NATIONAL AND KAPODISTRIAN UNIVERSITY OF ATHENS
SCHOOL OF SCIENCE
FACULTY OF GEOLOGY AND GEOENVIRONMENT
DEPARTMENT OF GEOPHYSICS & GEOTHERMICS

PERFORMANCE EVALUATION OF THE MAGOULA – NAFPAKTOS ARRAY (WEST GULF OF CORINTH)

Kravvariti Phaedra - Despina

Postgraduate Thesis

<u>Three-member Examination Committee:</u>

Dr. Voulgaris Nicholas (Advisor)

Dr. Papadimitriou Panayiotis

Dr. Kassaras Iannis

ATHENS, 2018

The assignment of this thesis with title ‘Performance evaluation of the Magoula-Nafpaktos Array (West Gulf of Corinth) was made by the department of Geophysics and Geothermics, Faculty of Geology and Geoenvironmnet in order to investigate the efficiency of processing seismic data derived from the Magoula-Nafpaktos array, using azimuth and slowness. Before presenting the results of this study, I would like to pay my regards to those who helped me in any way complete this assignment.

I would like to express my sincere regards to Dr. Nicholas Voulgaris (Professor), for his guidance throughout the procedure as well as for his initial suggestion to investigate this specific issue. His assistance both in theoretical and technological matters were of great importance for the conduction of the study.

I would also like to pay my respects to Dr. Panayioti Papadimitriou (Professor) and Dr. Iannis Kassaras (Assistant Professor), who are the other two members of the examination committee for their targeted comments during the correction of the study.

I would also like to express my deep gratitude to my best friend Konstantinos Georgiou, for his assistance concerning issues of theoretical and practical computer science as well as my husband Konstantinos Fokas for his great support throughout this procedure.

Last but not least I would like to thank Dr. Andreas Karakostantis and Aggelos Mouzakiotis for their valuable assistance concerning some of the algorithms that were crucial for this study and the creation of some maps.

SUMMARY

The purpose of the current Master thesis is to evaluate the performance of a seismic array that was deployed in the area of Nafpaktos (Magoula region) during the period of November-December 2014. The array is composed by the following stations (MG00, MG01, MG02, MG03, MG04, MG05, MG06 and MG07). In order to perform the current research two different techniques were applied: beamforming and F-K analysis. Applying those techniques, two parameters of the wave's propagation were studied in detail and these are Slowness (u) and Backazimuth (Φ).

Περιεχόμενα

1. Introduction

1.1 The tectonic setting of Greece

From a geological point of view, Greece is bounded by a stable continental plate (Eurasian) to the north, the Adriatic Sea to the west, the Anatolian plate to the east and finally the Mediterranean oceanic plate to the south, which is the upper limit of the African plate. In general, Greece is located on the active convergent boundary between the African and the Eurasian plates (Figure 1) (Pearce et al., 2012).

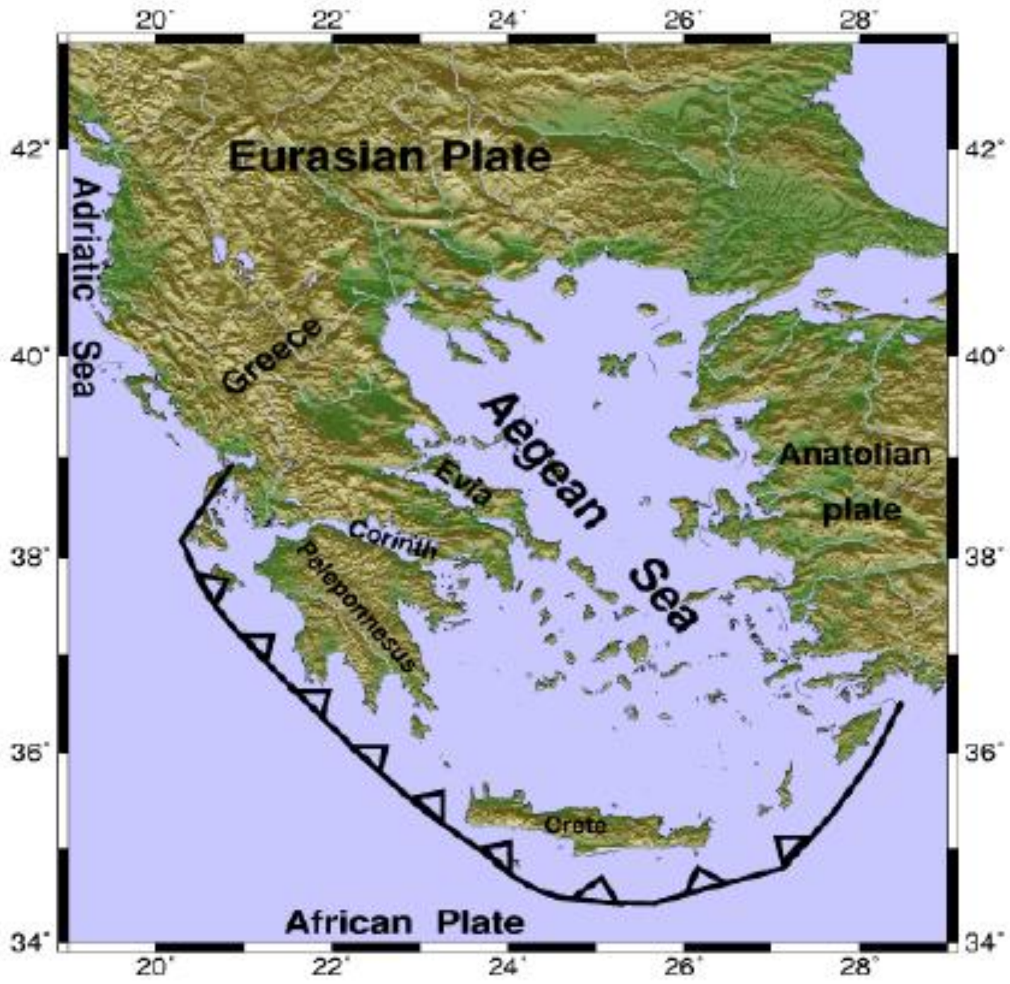

Figure 1. Greece. The convergent boundary between the Eurasian and the African plate along with the west and east geographical boundaries (Adriatic Sea and Anatolian plate respectively) (Pearce et al., 2012).

The main tectonic characteristics of the broader area of East Mediterranean are the aforementioned tectonic boundary and the Arabic plate, both of which have greatly influenced the morphology and the tectonics of Greece. More specifically, based on a wide variety of geological data, the Arabic plate seems to be moving with respect to the Eurasian plate by 18mm per year, having a N-NW direction for the last 3 million years. Based on similar geological data, the African plate is moving with respect to the Eurasian plate at a rate of 6mm per year towards north. These two discrete tectonic moves (that correlate with a 8-15mm per year time lag) have resulted in the formation of a great sinistral strike slip fault among the region of the Dead Sea which in turn shoves the Anatolian plate to the west. Based on that mechanism, one can say that the Anatolian plate is rotated anticlockwise relatively to the Eurasian plate (Pearce et al., 2012).

Another great tectonic feature of the area, created by those procedures, is the North Anatolian fault which is located in the northern part of the Anatolian plate (Figure 2). This dextral strike slip seems to have changed aspects of the convergent boundary while based on that tectonic feature, the Anatolian plate seems to rotate anticlockwise relatively to the Eurasian plate with a rate of 24mm/year (Pearce et al., 2012).

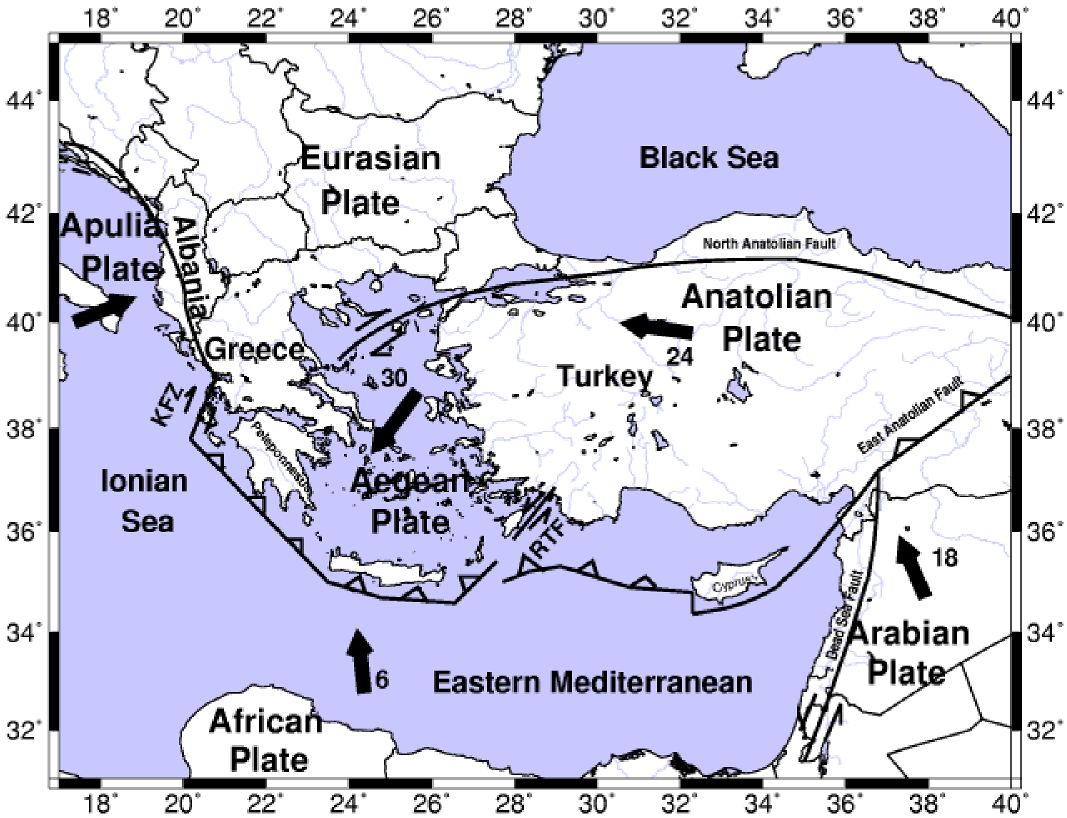

Figure 2. Schematic presentation of the relative tectonic motions that form the current tectonic model of Greece and especially of the Aegean Sea. The arrows indicate the plates' direction relatively to the, considered as stable, Eurasian plate. The number next to each arrow indicates the rate of motion of each plate in mm/year (Pearce et al., 20112).

The aforementioned conclusions about the relative motion of the Anatolian plate towards the east and its rate of motion, are also confirmed by GPS data (Figure 3) (Kreemer and Chamot-Rooke, 2004). Apart from this, GPS data can also confirm the anticlockwise motion of the African plate relatively to the Eurasian plate which occurs for the last 92 million years. The fact that the African plate also subducts beneath the Eurasian plate is also indicated both by the existence of the volcanic arc in the Aegean region and by the spatial distribution of the area's earthquakes. Detailed tomography that has taken place along this region also confirms the existence of this subduction zone (Pearce et al., 2012).

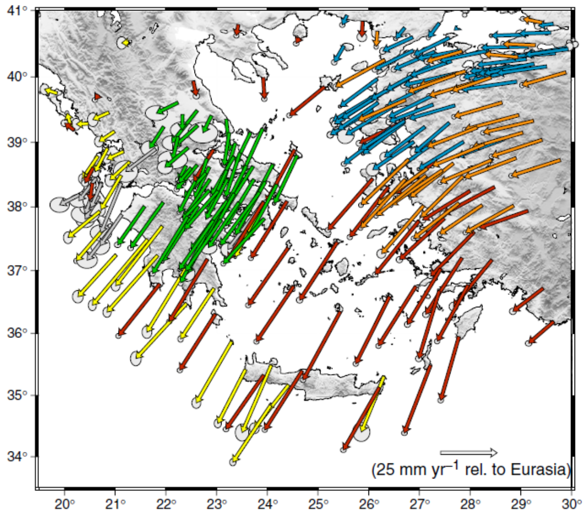

Figure 3. The vectors correspond to GPS data that indicate both the direction and the rate of movement. Those movements are representative both for the Anatolian plate and the Aegean microplate, when considering the Eurasian plate as stable. The different colours correspond to data derived from different papers (Kreemer and Chamot-Rooke, 2004).

Due to the subduction that takes place in Greece, the area with the most geological interest is the Aegean. The volcanic arc and the island arc in the Aegean are typical effects of that subduction. This subduction lies from the coast of North Greece-Albania, characterizes the south coast of Crete and ends at the big clockwise strike-slip fault of Rhodes (Figure 4) (Pearce et al., 2012). The subduction's rate is not the same along the zone. Contrary to the subduction under the Aegean, the subduction under the Hellenides is characterized by a smaller rate (2-4mmper year) and is separated by the area of the faster subduction with a clockwise strike slip in Kefalonia, which moves almost 14mm per year (Figure 5) (Vassilakis et al., 2011).

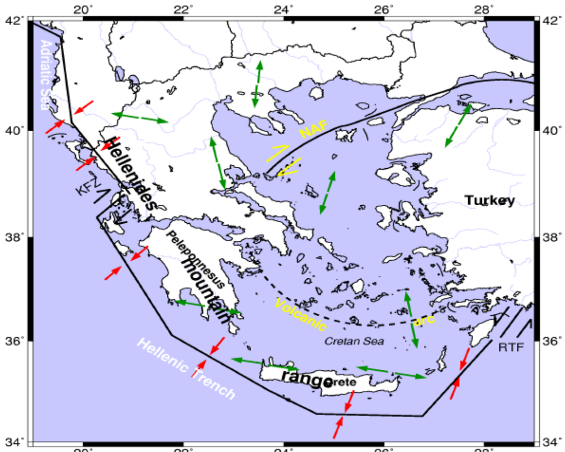

Figure 4.The Greek subduction arc and the major tectonic settings of Greece (Pearce et al., 2012).

Most of the Greek region is characterized by an extensive tectonic setting (Figure 4). This extension causes a reduction in the lithosphere's thickness which has a N-S direction and increases towards the East (Pearce et al., 2012). The Aegean microplate moves with a rate of 30-35mm per year towards SW, in relation to the stable Anatolian microplate (Vassilakis et al., 2011; Pearce et al., 2012).

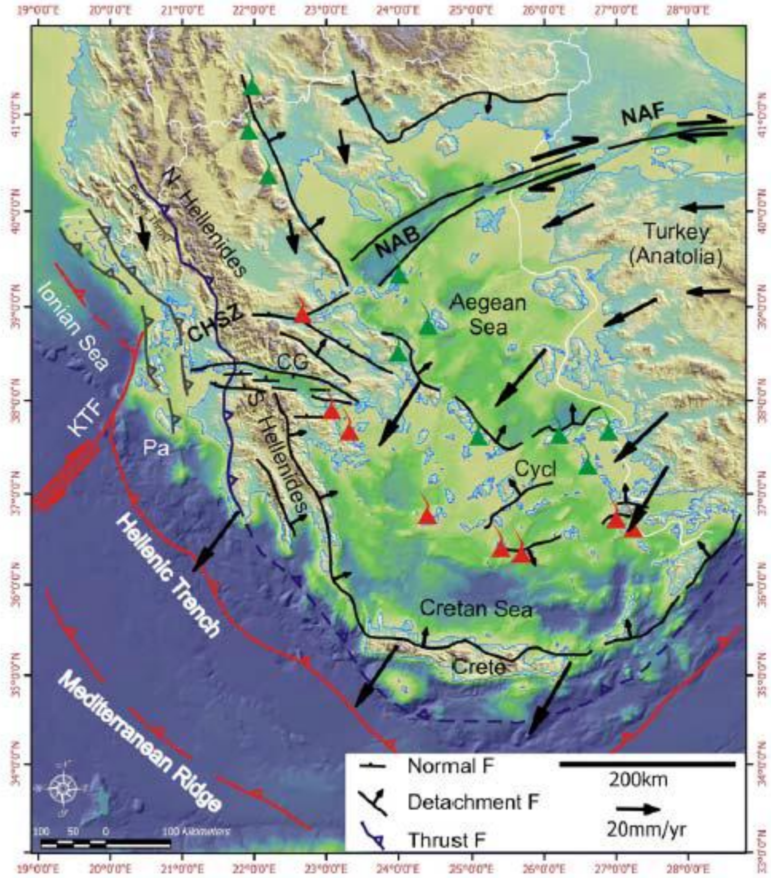

Figure 5.The major geological structures of Greece. The red and green arrows correspond to the position of the volcanic arc today and during the Miocene, respectively. The big black arrows show the velocity based on GPS data with the Eurasian plate considered as stable. (CG): Corinth Gulf, (NAF): North Anatolian Fault, (KTF):Detachment fault of Kefalonia, (PA): Paxoi Zone and (NAB): North Aegean Basin, (Vassilakis et al., 2011).

In general, the Aegean area appears to be an elevated plateau that lies between the Black Sea (minimum depth 1300m) and the Mediterranean (minimum depth 1500m), with a minimum depth of 350m. It is also characterized by a relatively thick crust (25-30m) which appears to be thicker that the typical oceanic crust, yet thinner that a continental crust. The heat flow of high temperatures is also evident in the area due to the extension that takes place and makes the crust thinner (Pearce et al., 2012). This is the reason why the Aegean area is not only one of the most seismically energetic areas worldwide (Vassilakis et al., 2011;Pearce et al., 2012)but also one of the fastest deforming area (Pearce et al., 2012). Based on seismic data, the Benioff zone under the Aegean area reaches up until

180km depth under the volcanic arc and based on tomography one can say that it might extend even northern. Moreover, based on isotopes, little amount of sediments have already embodied in the volcanic formations, which leads to the conclusion that the subducted plate has not been at depths that melting takes place, yet. What is more, based on seismological data, there is a low velocity layer on the upper mantle in the middle of the Aegean, which is caused by the dehydration of the subducted plate (Pearce et al., 2012).

As far as the mainland is concerned, its formation is highly related to the Tethys Sea. More specifically, during the last stages of Tethys' subduction, several continental terranes cleaved off the African Continent, moved towards the north, merged and formed a mass between Eurasia and Africa (Pearce et al., 2012). This is why the highest areas of the mainland are not characterized by thick crust but by overthrusts and folds (Vassilakis al., 2012). This mass is now known as Hellenides. Hellenides have a NW direction and are near the subduction zone that lies in the Ionian Sea (Ring et al., 2010; Pearce et al., 2012). Despite the fact that the subduction has been continuous since the Jurassic era, the thrusts happened progressively from the internal to the external Hellenides (based on the terranes' rate of movement). The geology of Hellenides is separated in units, each of which is characterized by specific petrology, tectonic history, deformation and preorogenic palaeogeography. The main units found in a cross-section along the Aegean (heading from the North to the South) are (Figure 6): (a) the Srednogorie Block and Rhodope-Sakarya Block, (b) the Vardar-Izmir Oceanic Unit, (c) the Pelagonian-Lycian Block, (d) the Pindos Oceanic Unit (including the Cycladic Blueschist Unit), (e) the Tripolitza Block, (f) the Ionian Block, and (g) the East Mediterranean Ocean (Ring et al., 2010).

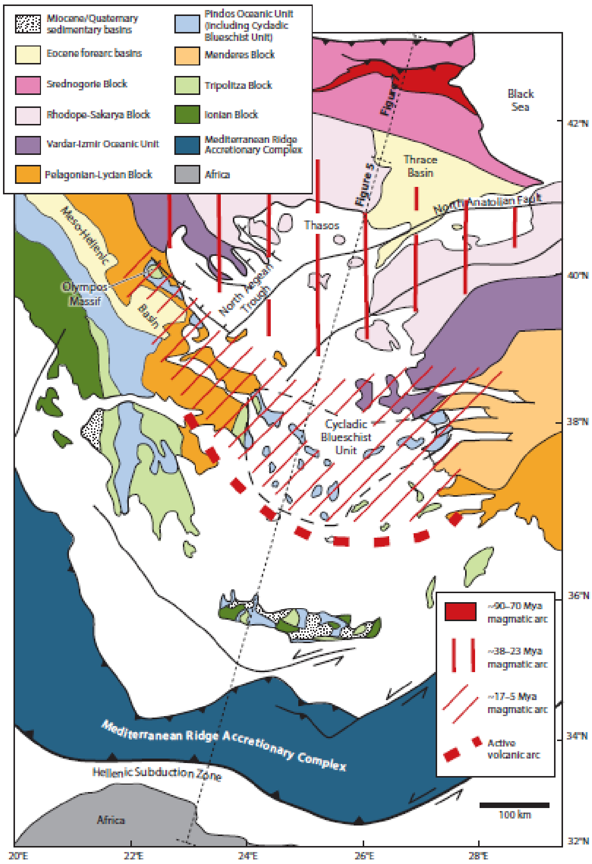

Figure 6.Geological cross-section along the Aegean and the units of Hellenides (Ring et al., 2010).

In general, the unit of Srednogorie and Rhodope were placed in that exact location about 100-185 million years ago. The Vardar-Izmir Ocean was placed under the Srednogorie-Rhodope unit during the Cretaceous (145-65 million years ago) and is mainly composed of ophioliths from the Jurassic Era (145-200 million years ago). After that, the Pelagonian block, which consists of metamorphic rocks, was placed under the Vardar Ocean. Those metamorphic rocks have undergone a blueschist metamorphic phase about 85-125 million years ago. Under the Pelagonian block lies the ocean of Pindos which is mainly composed by condinetal sediments. The Tripoly unit occurs structurally beneath the ocean of Pindos, it has Eocene – Oligocene and is a part of the Triassic-Eocene platform flysch. The unit of Tripoli is separated from the Ionian with a tectonic detachment. The Ionian block is characterized by Eocene-Miocene flysch that indicates the time that the tectonic changes occurred. Last but not least, the ocean of the East Mediterranean was placed in its position about 19 million years ago (Ring et al., 2010).

In other indicative cross-sections along the Peloponnese and the central part of Greece one can find the following: Mani, Arna, Tripolis, Pindos and the units of Parnassos and Vardousia over the coat of Pindos and the coat of the internal Hellenides respectively (Papanikolaou and Royden, 2007).

1.2 The main geomorphologic features of Greece

More specifically, some of the major geological features of Greece, which will be analyzed briefly later, are: the North Aegean Basin, the Corinth Gulf, the Greek volcanic arc and the Basin of Crete.

1.2.1 The North Aegean Basin

The North Aegean Basin is basically characterized by strike slips and an extensional tectonic setting with N-S direction (Figure 4). The basic morphological features of North Aegean are the Strymon Basin, the North Aegean Trough and the Skyros basin. The North Aegean Trough includes several smaller basins that are separated by faults. The largest basins of them are the Sporades basin (with NE-SW direction) and the Saros Basin (with ENE-WSW direction). Many geologists consider that the faults separating those basins are a natural extension of the North Anatolian Fault (Pearce et al., 2012).

1.2.2 Corinth Gulf

Corinth Gulf is a seismically active zone of 110km length that is characterized by an extensional tectonic field with N-S direction. The extensional rate in this area is about 15mm per year. Due to this tectonic setting, there are many normal faults (Tsodoulos et al., 2008) with E-W direction in the gulf, which make this area one of the most seismically active zone in Europe (Figure 7). These faults raise the south part of the gulf with a rate of 1mm every year. Many geologists consider the faults in the Corinth Gulf as the western part of the North Anatolian Fault (Moretti et al., 2003).

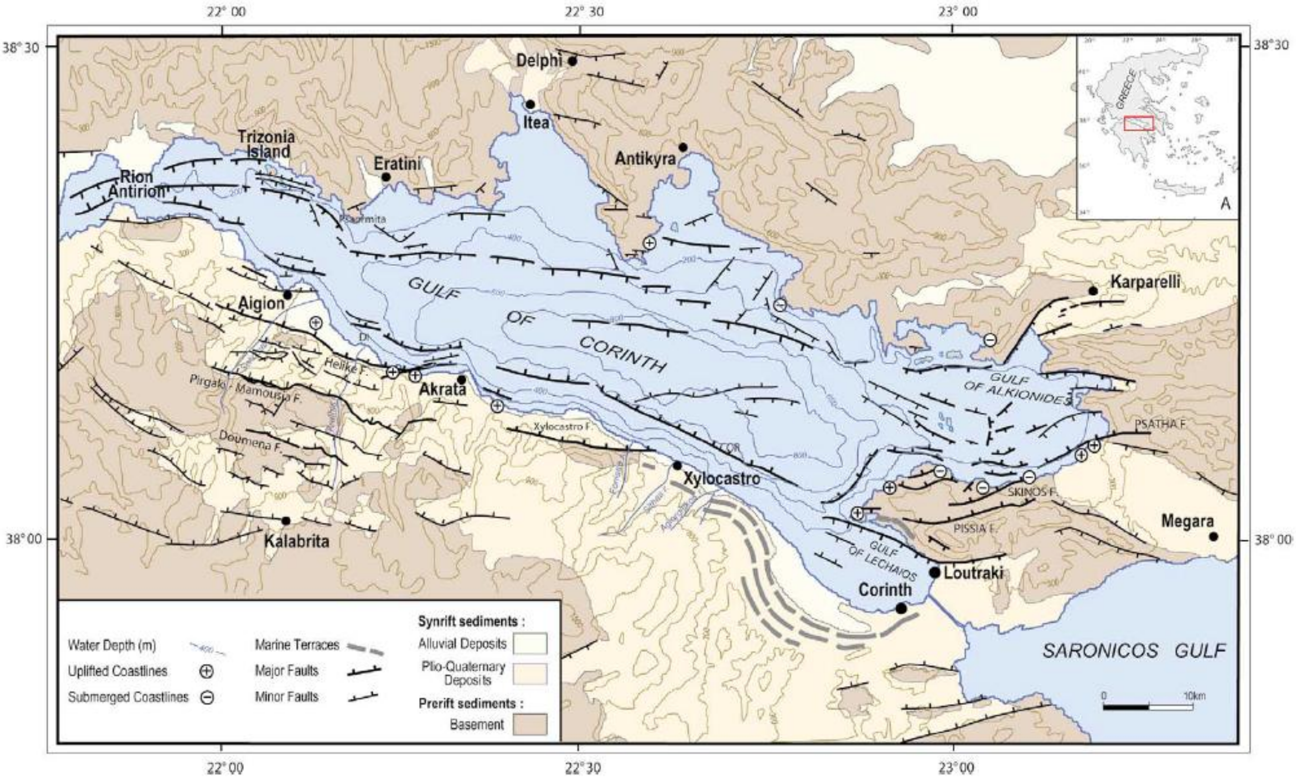

Figure 7.Tectonic map of the Corinth Gulf (Moretti et al., 2003).

The eastern part of the gulf is wider with layers of coherent sediments thicker than those found in the western part. On the other hand, the rate of the extension appears to be faster on the western part of the gulf, especially on the Aigio and Rio-Antirio areas where the gulf is narrower. From a geomorphological point of view, the maximum depth of the east part of the gulf reaches 860m, the maximum width is about 30km and the thickest layer of sediments is 2,4km. As far as the western part is concerned the maximum depth is 60m (Rio-Antirio area) and the 400m in the Aigio-Trizonia area where the gulf is 6km wide (Figure 8) (Moretti et al., 2003).

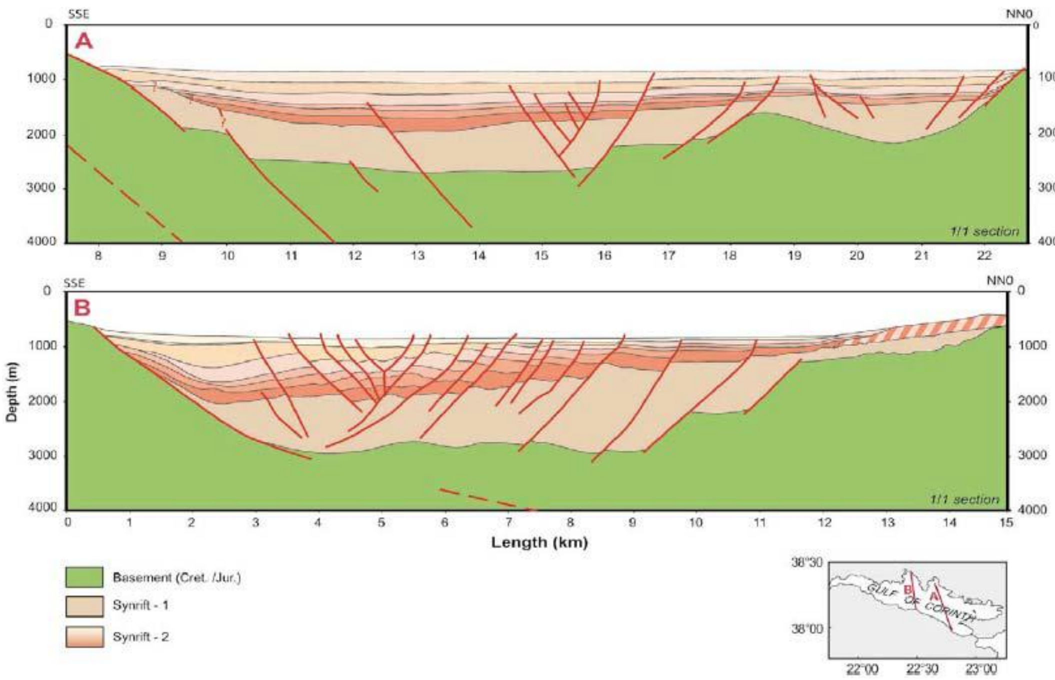

Figure 8.Cross sections of the Corinth Gulf (Moretti et al., 2003).

1.2.3 The Aegean's Volcanic Arc

The volcanic arc is located in the south Aegean and is created due to the subduction of the African plate beneath the Aegean's microplate (Pe-Piper and Piper, 2005) and is composed by the following volcanoes: Kromionia, Sousaki, Methana, Aigina, Poros, Milos, Kimolos, Santorini, Kos and Nisyros (Figure 9) (Morris, 2000; Drouza et al., 2007). It can be separated into two distinctive volcanic arcs that have differences in the magmatic type, the age, the spatial distribution of the faults and the petrogenesis (Pe-Piper and Piper, 2005).

Figure 9.The Volcanic Arc of the south Aegean (Drouza et al., 2007).

More specifically, the western part of the arc, which includes Aigina and Methana, produces andesitic-dacitic magma of Pliocenic age and is characterized by listric faults with E-W direction and small displacement. However, the central and eastern part of this volcanic arc (Milos, Santorini, Nisyros etc.) has tholeitic and calc-alkaline basalts, andesites, dacites and rhyoliths and many pyroclastic materials. Their age is middle-upper Quaternary. The younger magma that is produced in that part of the volcanic arc is a result of the melting of both the dehydrated mantle (calc-alkaline composition) and the asthenospheric mantle (tholeitic magma) which is affected by the extensional tectonic setting of the broader area (Pe-Piper and Piper, 2005).

Apart from these two types of magma, there is also a third one, appearing in a much smaller rate, which indicates the existence of Pliocenic felsic lava in the islands of Kromionia (area near the canal of Corinth) and Kos (Pe-Piper and Piper, 2005).

1.2.4 The Cretan Basin

The Cretan basin is located between the outer arc formed by the islands of Kythira, Antikythira, Crete, Karpathos, Rhodes and the active volcanic arc. The basin's tectonic setting is extensional (Figure 4) and the whole region moves towards the south. From a geomorhological point of view, the depth of the basin increases to the east while its northern part is controlled by a big fault. Finally, based on models focusing on the relation between the thickness of the basin's crust and the existing extensional tectonic field, the Cretan basin seems to have been detached from the Cyclades area (Pearce et al., 2012). This is attributed to the big detachment fault that lies in the basin and seems to be extended under the Cyclades area (based on the big relocations that took place in the Aegean before the early Miocene) (Ring and Reischmann, 2002).

In general, the tectonic field of Greece indicates extension with NW-SE direction in the area of north Peloponnese and western Crete and E-W among the central and eastern Crete. Peloponnese is characterized by two huge faults with NNW direction, Crete has faults with E-W, ESE-NWN and NA-SW direction and finally Rhodes is characterized by faults with NNE-SSW direction. Those faults are normal and are parallel to the Greek arc (Pearce et al., 2012).

2. The Seismological and Geological Setting of the west part of the Corinth Gulf

2.1 Seismology in the Corinth Gulf

The seismicity in Gulf of Corinth is monitored with detail by two separate and densely established seismological networks; the Corinth Rift Laboratory Network (CRLN) which is a rather local network aiming at monitoring the western part of the Gulf since 2000 (Kapetanidis et al., 2015; Kaviris et al., 2017) near Aigion and the Hellenic Unified Seismological Network (HUSN) (Kaviris et al., 2017).

The CRL network is a semi-permanent network located at the area of Aigion aiming at monitoring the microseismicity of the Corinth Gulf, recording events down to 1. In this way researchers can provide us with more details concerning the active structures in the broader area. More specifically the CRLN is comprised of 12 stations, 5 of which are located north of the Gulf and the other seven south of the Gulf. The velocimeters of the stations are in depths of 60-130m in boreholes so as to be able to monitor microseismicity and avoid any noise produced by human activities (Lyon-Caen et al., 2004). Throughout their operation, these stations provide us with real-time continuous waveforms and based on Kapetanidis and Papadimitriou (2011), from 2000 until 2011 they have recorded over 10000 events every year. More specifically, during rest periods the network might record 10-20 events daily with magnitude that does not exceed 2, while in case of an unrest that number might raise to 150 (Bourouis and Cornet, 2009).

The broader area has suffered from several earthquakes even during the historical times, which have destroyed whole cities located around the Gulf. Such an event was the earthquake in Heliki in 373BC (Kaviris et al., 2010, Kapetanidis et al., 2015, Kaviris et al., 2017).

The seismic catalogues are complete for events greater than 6 for the past 300 years (Kapetanidis et al., 2015). Great seismic activity is evident in the area since 1911, including events with magnitude greater than 6. The majority of those earthquakes are attributed to normal focal mechanisms with N-S oriented extension (Hatzfeld, 2000). Such events took place in Corinth in 1928 (Ms 6.3) (Kaviris et al., 2010), in Eratine of Phokida in 1965 (MW 6.3), in Antikyra in 1970 (Mw 6.2) (Kapetanidis et al., 2015), in Galaxidi in 1992 (Mw 5.8) (Kaviris et al., 2017) and in Aigion in 1995 (Ms 6.2) (Bernard et al., 1997; Kaviris et al., 2010; Kaviris et al., 2017). The latter two are attributed to shallow northdipping offshore faults (Kapetanidis et al., 2015). In the years after 1995, the most important earthquakes that were recorded were both located in the Efpalio earthquake in 2010 and they both had a magnitude of Mw 5.1 (Kaviris et al., 2017).

The seismicity of the western part of the gulf is mostly characterized by seismic swarms (Kaviris et al., 2017). Some of the most recent swarms took place in 2008 and in 2013. The first of those occurred four months before the great earthquake of Andravida in NW Peloponnesus and included two rather moderate events with magnitude M4.6 (Kaviris et al., 2010). The other one started on May 21, 2013 in the SE of Aigion and included several earthquakes of approximately 3.5 magnitude. That went on until 15th July when the western part of the swarm was suddenly activated. Until the end of the phenomenon on August 31st, more than 1500 earthquakes were recorded from 15 different seismological stations (Kapetanidis et al., 2015).

2.2 Geological Setting of the Corinth Gulf

The Gulf of Corinth lies between the northern continental Greece and Peloponnesus (Chery, 2001), in the fore-arc region of the Aegean Sea (Weiss, 2004). Its length is approximately 120km long with a N120°E trend and based on chronological data retrieved from sediments that were deposited during the rifting procedure, this rifting seems to have started 5Ma ago (Beckers et al., 2015). The basin is also characterized by a sequence of active faults that extend the gulf (Chery, 2001; Weiss, 2004) with a north-south direction (Weiss, 2004) and a rate of 10-15mm per year based on GPS data. This extension corresponds to 33% of the total displacement that takes place in the Aegean and reaches 30 ±1 mm per year. It is probably attributed to the African plate's 'rollback' and the southwest displacement of the Anatolian plate (Weiss, 2004; McNeil et al., 2005; Beckers et al., 2015). This extension seems to be amplified towards the western tip of the gulf (Weiss, 2004).

The basin's faults are either high angle or low angle normal ones (Figure 10) (Chery, 2001). Any other type of focal mechanism is attributed to smaller fracture zones that are located close to the major faulting zones extremities (Rigo et al., 1996). Supposing that the high angle faults (that are dominant in the southern part of the basin, like the Helike fault or the Aigion fault) reach a depth of 10-15km, based on morphological features, the basin's extension should have been 7mm yearly. Comparing the predicted rate of extension with the real one, one can conclude that the extensional field that characterizes the area is attributed to high angle faults by 50-75% (Chery, 2001). The remaining percentage has not been attributed to a specific king of faulting so far, even though focal mechanisms in the area have revealed the existence of a detachment fault which is characterised by a dip of 15° (±10°) towards the north. That fault was recorded at depths of 8-12km, north of the high angle faults, and plays a really important role in the overall extension (Rigo et al., 1996; Chery, 2001; Weiss, 2004; Beckers et al., 2015). Based on Chouliaras et al, 2015 the detachment's minimum depth offshore is 6km. A very important evidence for the existence of that detachment zone was an extended research that took place in the area after the Aigion earthquake in 1995. That study proved, through focal mechanism modeling the existence of that low- angle dipping fault near the brittle crust. More specifically, that specific event was attributed to a low-dip angle (33°) normal offshore fault 15km from the city of Aigion (Bernard et al., 1997). Apart from that, the extension seems to be currently controlled by several offshore faults with a dip of 0 or 180° (Beckers et al., 2015).

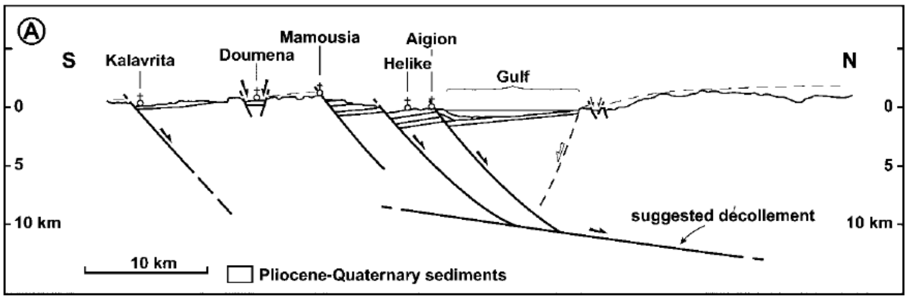

Figure 10. Cross section from south to north of the western part of the Gulf of Corinth. The cross section depicts the two high angle faults that are active (Helike and Aigion) as well as the suggested low angle detachment that is evident through the focal mechanisms from the area's microseismicity (Chery, 2001).

2.2.1 Onshore faults

As far as the western Corinth Gulf is concerned, the basin seems to be extended by 16mm every year. The main percentage of this extension is clearly attributed to offshore active faulting, yet there have also been identified some onshore faults (Beckers et al., 2015). More specifically, the northwestern coastline of Peloponnesus is characterized by the Eliki-Aigion-Kamarai-Psathopyrgos fault system (Figure 11). The slip rates of those faults, resulting from trench analysis, seismic data, drilling, uplifted coastlines and dislocation modeling are presented in table 1 (Beckers et al., 2015).

The Eliki fault system is located in the southern coats of the Corinth Gulf and it is a north-dipping structure (Weiss, 2004). It is segmented into two major parts, known as the Eastern and the Western Eliki north-dipping faults. The length of those faults reaches the 15-20km and they are divided by a wide transfer zone at the Kerynites River. The age of that fault has been calculated at 07-1.1Ma. It can be inferred by measurements that took place in the uplifted terraces in the Eastern segment of the Eliki fault that the uplift rates of the fault in the East are approximately 1 -1.5mm per year and they are reduced towards the eastern tip of the fault. Also, based on superficial measurements the dip angle of the fault seems to be 50° at least up until the depths of 1-2km (Mc Neill et al., 2005; Ford et al., 2012) where there are indications that it transforms into a low angle listric fault (Bernard et al., 2006) with a dip of 22°-15° (Ford et al., 2012). The fault has ruptured carbonate sediments that have been exposed locally on the coastline (Collier and Jones, 2004). This eastern tip of the Eliki fault was most recently activated in the 1861 earthquakewith Ms=6.6 (Mc Neill et al., 2005). The Western part of the Eliki fault seems to be deactivated due to the existence of the Kamarai fault zone close to it (Bernard et al., 2006).

The Aigion fault is 10±1km long and 10±2km wide (Bernard et al., 2006) and has a NW-SE direction (Palyvos et al., 2005). It is divided into two major faults and several smaller ones with less significance. Although the Aigion fault is mapped onshore, several authors have suggested that it continues further to the east, having an offshore segment (Palyvos et al., 2005; Mc Neill et al., 2007). The offshore segment is composed by two major faults that form a graben and several minor ones into the graben. Those offshore segments are traced up until a distance of 3km from the shore and have a dip angle of 50-60°. The average slip rate throughout the Holocene and the late Quaternary period is approximately 2.5-4.5mm/y (Mc Neill et al., 2007).

The Kamari fault zone is 9±2 km long and 7±1km wide and it lies between the Psathopyrgos and the Aigion fault systems, connecting them. Its geometry suggests a possibility of generating an earthquake with a magnitude up to 6.2 (Bernard et al., 2006).

The Psathopyrgos normal fault is the westernmost onshore fault of the western Gulf. It has an E-W direction and a dip of approximately 60° to the north (Bernard et al., 2008; Sokos et al., 2012). Its length is approximately 15±2 km and it is 9±2km wide (Bernard et al., 2006). The Psathopyrgos fault is separated from the offshore faults with the Selianitika fault while it is also linked to the Rion-Patras faults to the south (Sokos et al., 2012). Despite being an active fault it hasn't produced any significant earthquake for the last 300 years. Yet in November-December 2002 a large seismic swarm took place on that fault, recording earthquakes with magnitude up to 3.5 (Bernard et al., 2008).

Fault system	Slip rate (mm/year)
Eliki	1-1.5
Aigion	2.5-4.5
Kamari	1.9-2.7

Table 1. The onshore fault systems of the Corinth Gulf along with their slip rate.

Another onshore faulting system is the Marathias fault that lies in the southern part of the continental Greece (northern shoreline of Corinth Gulf) (Figure 11). Despite the fact that it is mapped in detail, its current activity has not been proven (Beckers et al., 2015). It is 12km long and it has a dip of 55° to the south (Sokos et al., 2012).

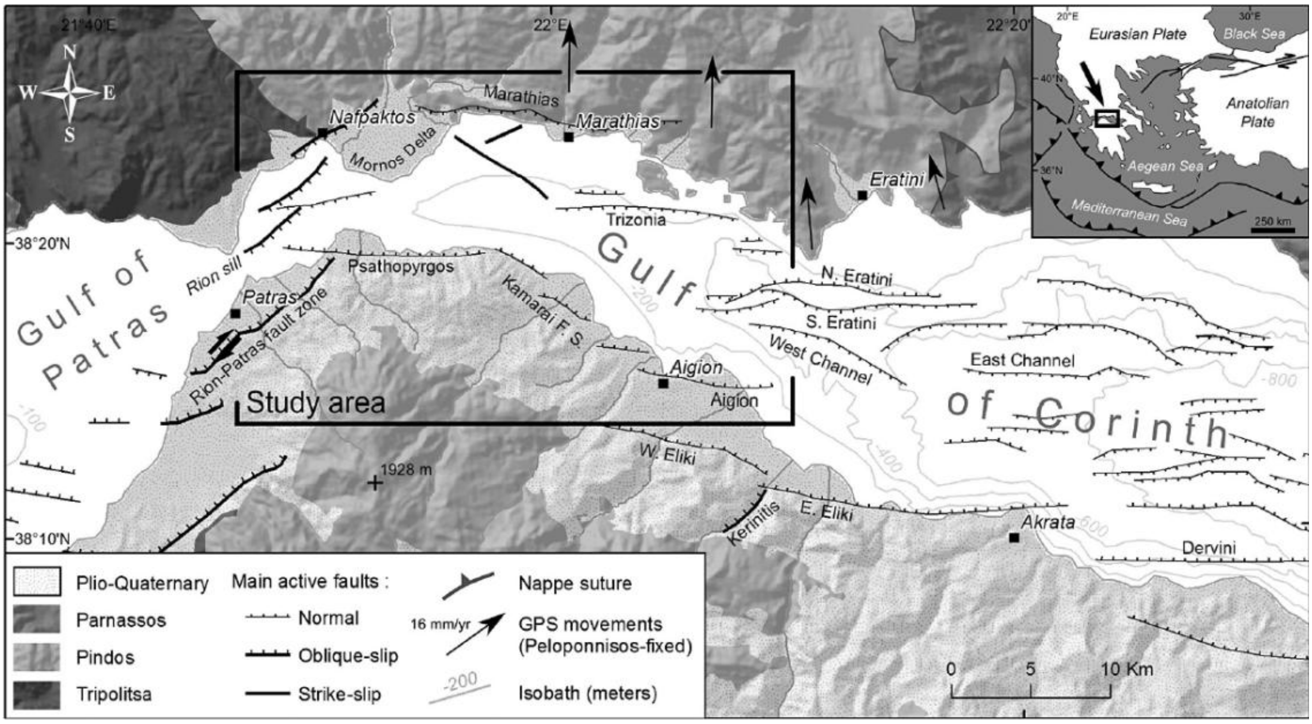

Figure 11. Map of the western and central segment of the Gulf of Corinth with several offshore and onshore faults (Beckers et al., 2015).

Based on the interpretation of the area's seismic activity, it is suggested, as already mentioned, that the onshore faults of the southern coast of the Gulf (Western Eliki fault, Aigion fault) seem to be connected in depth, creating a detachment formation (Figure 12) (Rigo et al., 1996; Bernard et al., 2006).

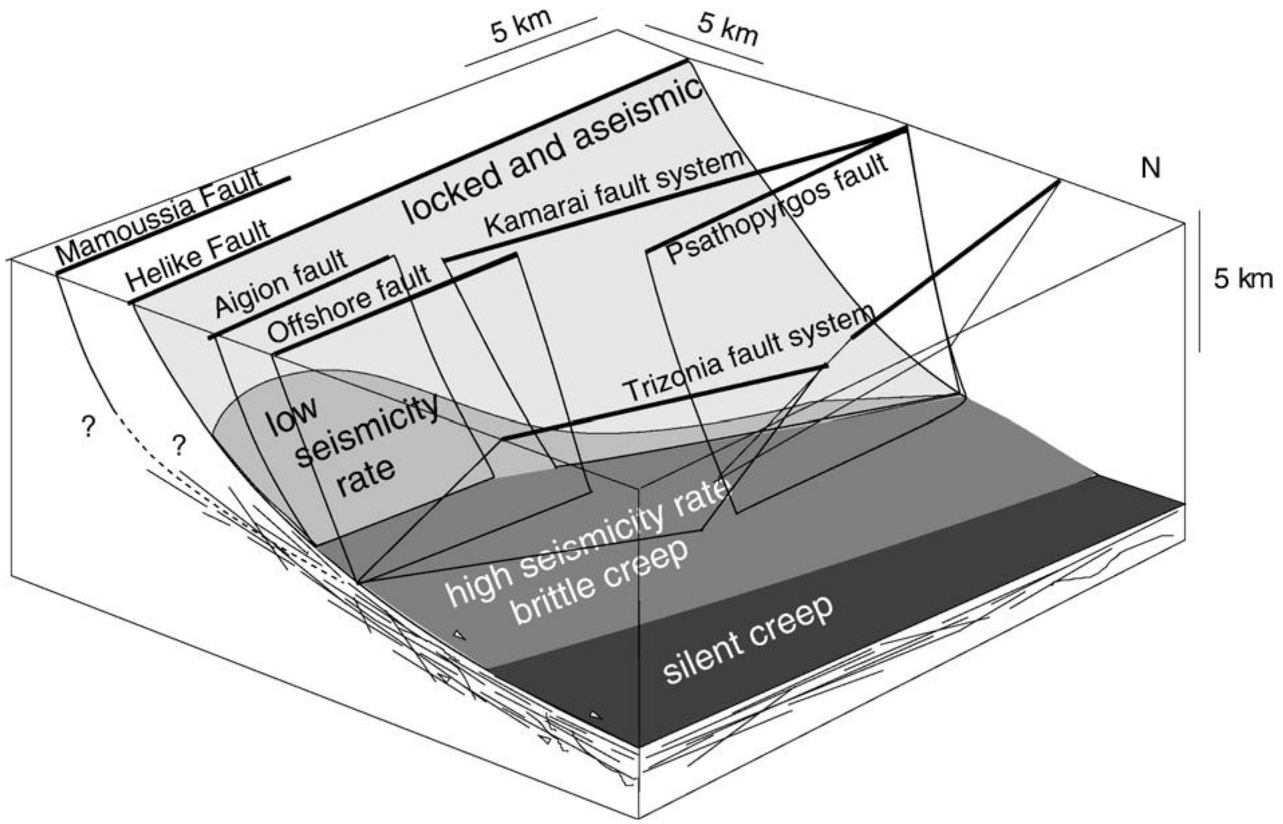

Figure 12. Proposed fault geometry based on the microseismicity that took place in the area during 2000-2001 (Bernard et al., 2006).

2.2.2 Offshore faults

In order to study and map the tectonic setting of the area, the Gulf of Corinth has been divided into 5 different sectors depending on the characteristics of each one. Starting from the west, there is the westernmost sector, the west sector, the central sector, the east sector and the easternmost sector. Each of those sectors is characterized by different fault systems (Figure 13). Yet, it can be said that along the south coast of the Corinth Gulf there is a dominance of north-dipping normal faults, whereas the north coast is mainly characterized by their antithetic south-dipping normal faults (Westaway, 2002; Chouliaras et al., 2015). Apart from these, several studies concerning focal mechanisms in the western part of the gulf based on microseismicity, suggest many mechanisms that happen to be antithetic when compared to the dominant ones in the north and south part respectively. Such events may provide us with reverse or even strike slip faults. Those can be attributed to small fracture zones or faults in the areas close to the larger faults, explaining the observed deviations (Rigo et al., 1996).

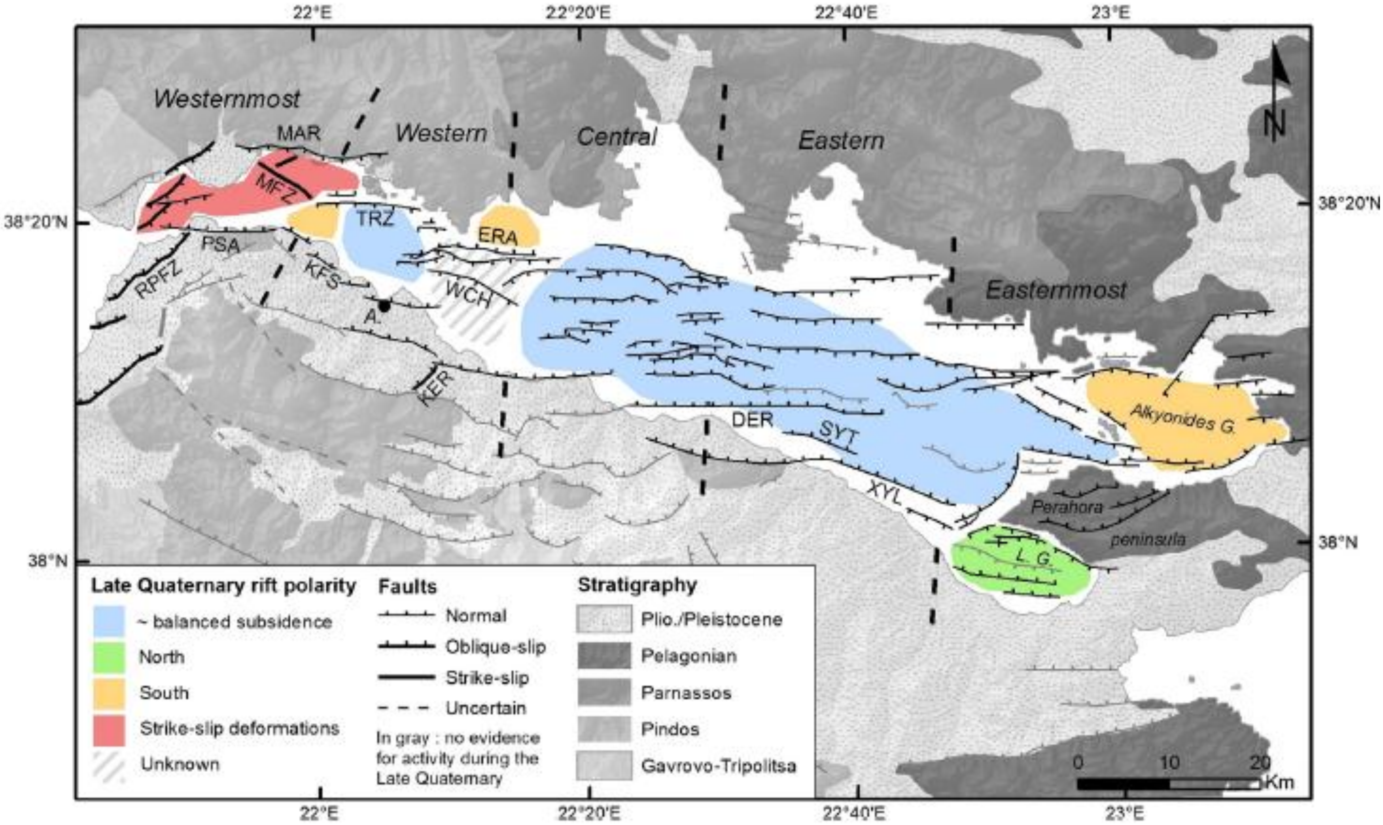

Figure 13. The Gulf of Corinth subdivided into 5 major sectors, i.e. Westernmost, western, central, eastern and easternmost (Beckers et al., 2015).

So far, scientists have mapped three major fault systems spread in the western part of the basin. More specifically, the Eratini-West Channel fault system is located in the East, the Nafpaktos fault system is situated in the west and the Trizonia fault system (TZFS) lies in the northern region of the basin. These three fault systems along with other submarine systems are depicted in Figure 11 (Beckers et al., 2015).

Analyzing the seismotectonic setting of the Gulf, starting from the westernmost boundary, there is no active fault today while the seismic data of the area are inadequate. Moving towards the NE, at the Nafpaktos basin, scientists have identified the Nafpaktos fault system with several dextral oblique-slip faults and some normal faults with SE dipping direction. Those faults can be subdivided into two major categories of faults that cross each other throughout the basin, forming a morphology that seems like a staircase (Figure 13) (Beckers et al., 2015).

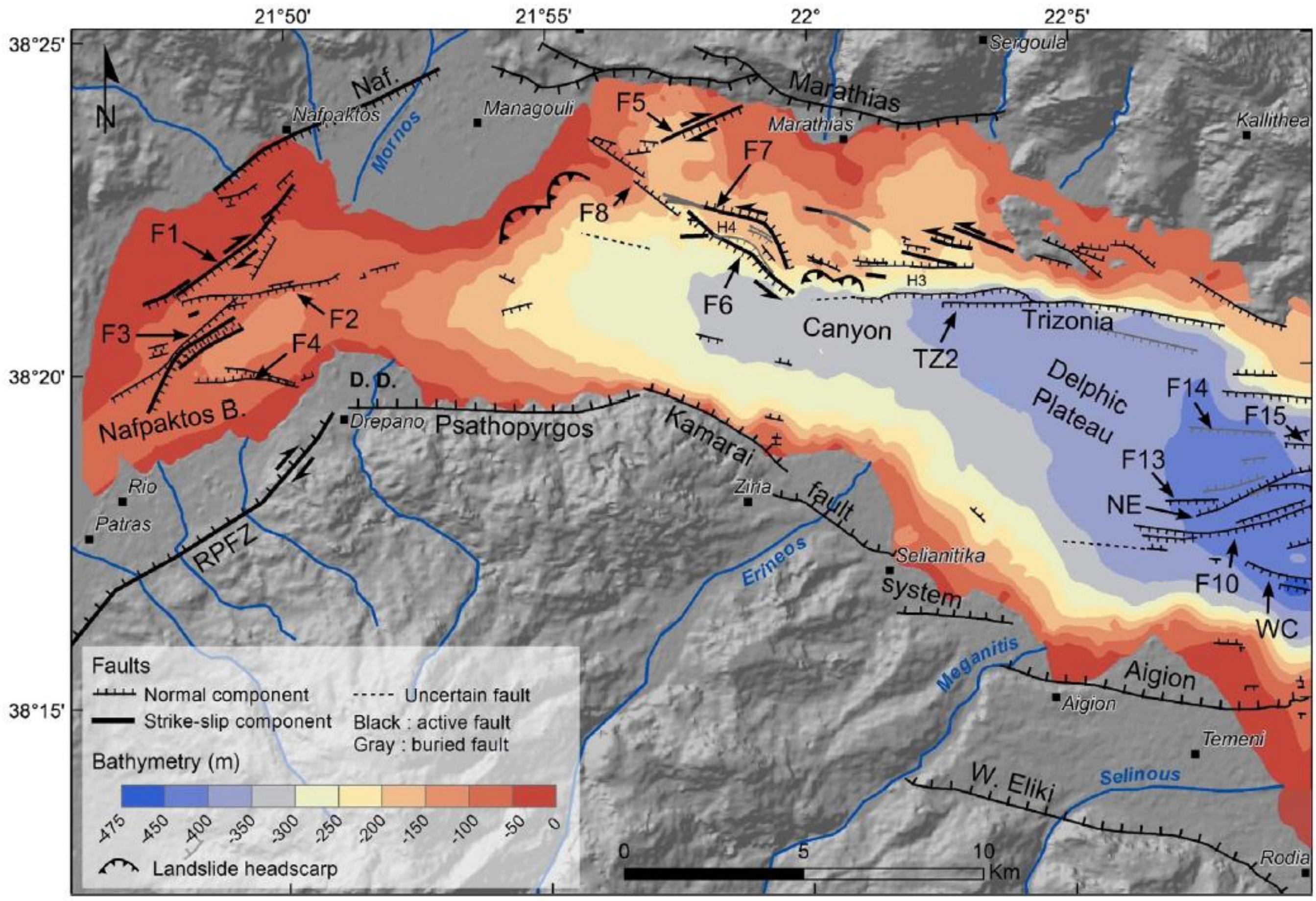

Figure 14. Map of the offshore and onshore faults identified in the area (Beckers et al., 2015).

As clearly shown in Figure 13, the first category of faults includes the F1 and F3 fault systems. Those faults, have a NE direction, almost parallel to the Rion-Patras fault zone. The F3 fault system seems to create a flower-type structure. The F1 fault system has a 5,5km length and its central part is characterized by 1.3-2.1mm vertical slip per year. It is mainly composed by strike-slip faults, as several of the F3 faults (Beckers et al., 2015).

The second category of faults, include the F2 and F4 normal fault systems. Both of these systems have an E-W direction, almost parallel to the onshore Psathopyrgos fault. In fact, the F4 fault zone seems to have been identified as the offshore part of the Psathopyrgos fault. The length of the F2 fault zone is approximately 6km and its average vertical slip is 1.8-2.9mm yearly (Beckers et al., 2015).

Moving to the east, the next major fault zone that is identified is the Trizonia fault zone (TZFS). The TZFS is located east of the Mornos Delta, spreading along the northern part of the gulf and is composed by the F6, F7 and F8 faults and several horsts bounded by those faults (H3 and H4). All of these formations are located west of the Trizonia Island. More specifically, the H3 horst is the biggest one with 4km length. Southern of that fault system, there are only some minor faults. The TZFS is 10-11.5km long and its eastern tip (in contrast to the western one) is well identified based on several data sets. The F6 normal fault zone has a NW-SE direction and it is south-dipping. On the other hand the F7 fault zone seems to be north-dipping. Yet, both of those normal faults have a strong strike slip component. The F8 fault zone, includes north-dipping normal faults and has a length of 3.4km. It is almost parallel to horst H4 and can be divided into two major segments. The F6, F7 and F8 fault zones form the Managouli fault zone, which has 7km length, lying with a NW-SE direction. The Managouli fault zone is located between the main Trizonia fault and the Mornos delta. Between the onshore Marathias fault and the offshore Managouli zone lies the F5 fault which has NE-SW direction and has a strong strike-slip component (despite its central part appears to be normal) (Beckers et al., 2015).

The third major fault zone that has been identified in the western part of the Corinth Gulf is the Eratini-West Channel fault zone which is mainly composed by normal faults with E-W direction (Beckers et al., 2015). The major characteristic of the Delphic Plateau (as the area is named) is the existence of three horsts that are subdivided into two categories: the bedrock horst (north) and the Eratini-West Channel horsts. Between those horsts, scientists have mapped 4 major fault formations. The first one is depicted in Figure 12 as F14. It has a really low dip angle and the deformation occurs towards the south. Based on the used data-set, this fault seems to be inactive for the last 130ka. At the eastern tip of the F14 fault starts the F15 active fault. Another south-dipping normal fault is the F10 fault which lies south of the F14 inactive fault and is 5km long. Depending on the location, the slip rate of that fault seems to be shifting from the west to the east since in the west it ranges between 0.5-0.8mm annually while in the center it ranges between 0.9 and 1.4mm per year. Moving southern, towards the Selinous prodelta area, scientists have also identified one more fault dipping to the south with a non-defined extension. Last but not least, the Eratini-West Channel horsts are controlled by the Eratini-West Channel fault which is situated close to the south coast of the Gulf (Beckers et al., 2015).

Moving to the east, the central Gulf of Corinth is basically characterized by the submarine eastern tip of the Eliki onshore fault, the Derveni fault system and the Galaxidi fault (Figure 14). The Eliki fault, as already mentioned, is divided into the onshore and the offshore segment. The offshore segment lies north of Akrata region and has a dip of 15° - 35°. Both the Eliki and the Derveni faults are north-dipping ones. The Derveni fault (DER) is located at the east of the Eliki fault, in the south part of the central Gulf. Near the surface its dip is approximately 35°, yet while moving deeper (up until 4km depth) it becomes a listric fault with an angle of 17-20°. The northern sector of the central part of the basin is characterized by another major formation, which is known as the Galaxidi fault. The Galaxidi fault is south-dipping but it does not reach the seafloor (Taylor et al., 2011).

Yet, apart from the tectonic setting of the Central Gulf of Corinth, there is also a great difference in the geological and sediment setting between the western and the central sector. Moving towards the east, the crust seems to be thinning and there are several discontinuities in the basement. These changes along with the different rifting procedures of the area is partially attributed to the fact that the western part of the Gulf is characterized by the Pindos nappe, while the central part's basement has sediments from the Gavrovo-Tripolitsa unit and a coat to the north from the Parnassos carbonate platform (Taylor et al., 2011).

The major faults mapped in the eastern sector of the Gulf are the eastern tip of the Derveni fault, the Sithas fault and the Xylocastro fault, all of which have an important overlap and are located at the southern margin of the Gulf (Figure 14). Based on several studies and unlike their superficial mapping, those faults seem to be emerging in depth (Taylor et al., 2011).

The Sithas fault, or Likoporia fault as it is referred by many, lies south of the Antikyra Gulf, between the Derveni and the Xylocastro faults. It is named after the local Sithas River which is located east of the Xylocastro area, and it is a N-dipping fault that extends up to the basement. Contrary to several of the central and eastern faults that have both an offshore and an onshore segment, the Sithas fault has only an offshore component. Close to the seafloor it can be referred as a high angle fault (45-48°) but as extending towards the basement it transforms into a listric fault with an angle of 28° (Taylor et al., 2011).

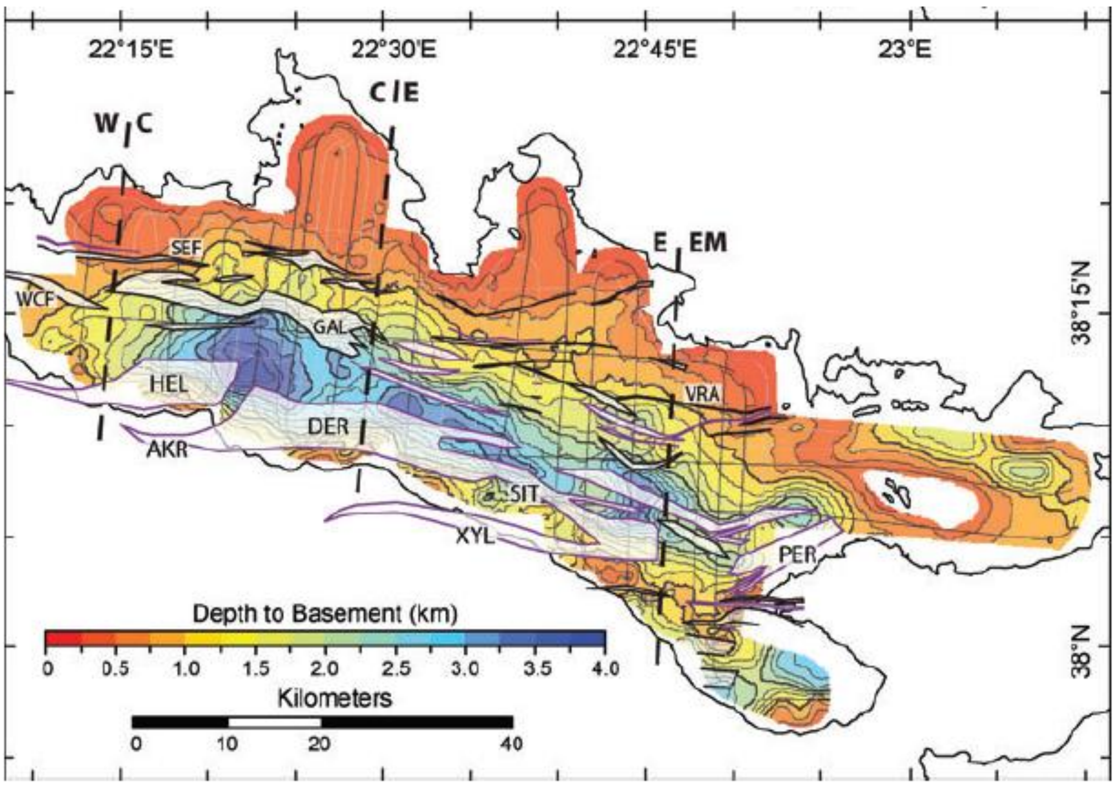

Figure 15. Fault zones of the western, central, eastern and easternmost sectors of the Gulf along with the depth to the basement for each position (Taylor et al., 2011).

The Xylocastro fault is mainly a submarine fault southern from the Sithas fault which extends to the west for about 20km onshore (Taylor et al., 2011) (Figure 15), while its total length is over 30km (Weiss, 2004). Just like the Sithas fault, it is considered to be a high-angle fault near the seafloor with a dip of approximately 45°, yet its angle seems to be decreasing close to the base, reaching the 20° (Taylor et al., 2011).

Last but not least, at the easternmost section of the eastern sector of the Gulf lies the Kiato fault, named after the closest town. The Kiato fault is a normal south-dipping fault with a really high-angle that reaches 75°. It is proposed that this fault is the submarine continuation of an onshore fault that constitutes the southern margin of the Xylocastro horst (Taylor et al., 2011).

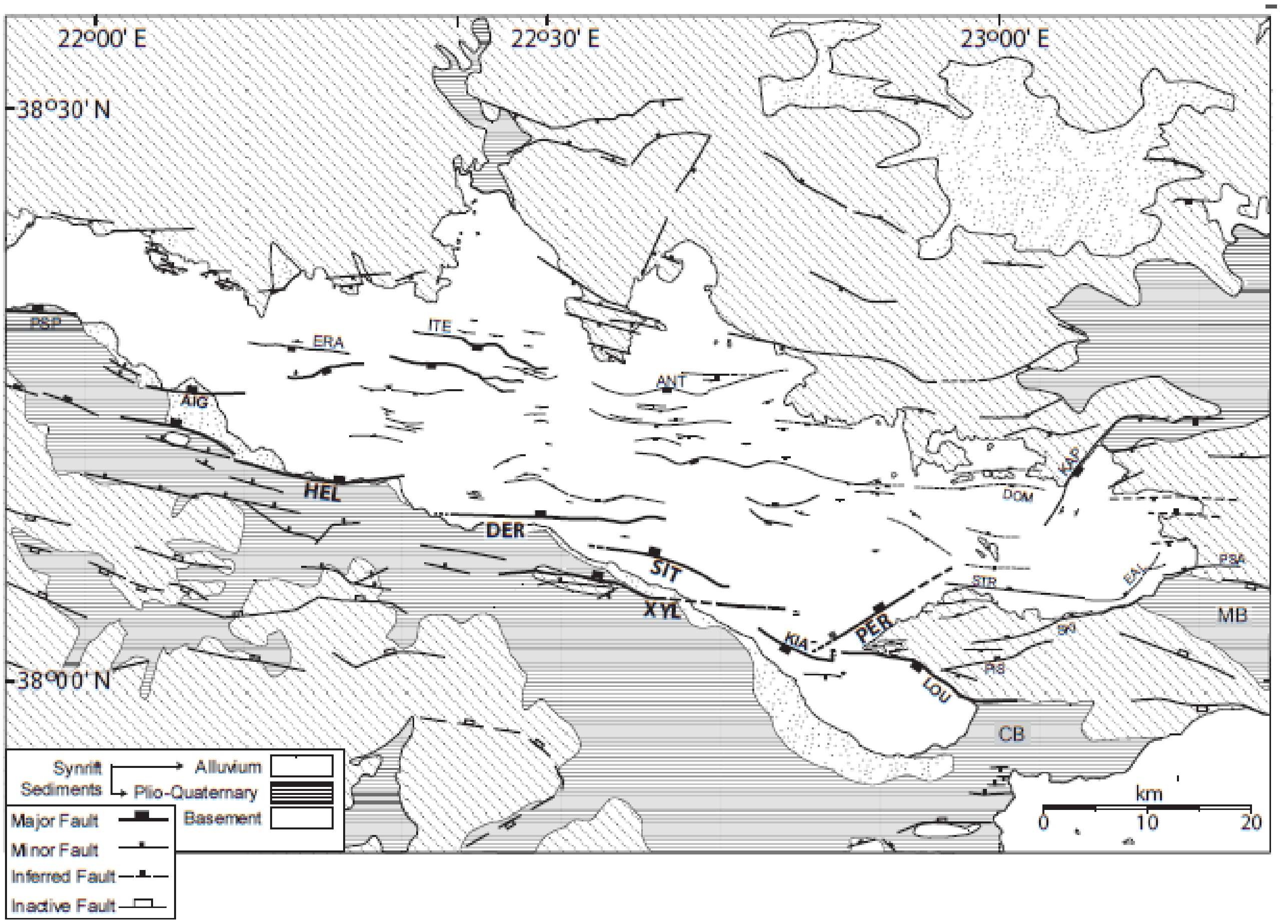

Figure 16. Fault map of the Gulf of Corinth, depicting most of the onshore and offshore major and minor faults (Weiss, 2004).

The easternmost part of the Gulf of Corinth displays a really complex fault system since it is comprised by three main subsystems; the one on the Perahora Peninsula, the one in the Alkyonides basin and the one in the Lechaio basin. Apart from the rifting complexity of the area, there is also a great change in the geological setting due to the transition that takes place from the Parnassos unit to the Pelagonian coat (Taylor et al., 2011).

Starting from the north and moving southwards, the Alkyonides gulf is a 12-km-wide subbasin, with 24km length that is locates in the NE part of the Gulf of Corinth. This subbasin is composed of three major offshore faults that coincide with the southern margin of the basin (Figure 16). The first fault, located in the SW of the Alkyonides basin is called the Strava fault and is subdivided into the northern and the southern Strava segment bounding the Strava graben to the north and to the south respectively. The high-angle South Strava fault has a length of 8km, with a 100°N-110°E direction and a dip angle of 40-45°. The sediments that dominate the area are Triassic-

Lower Cretaceous limestone and flysch deposits. The North Strava fault is a south dipping 6-km-long fault with similar characteristics to its South component) (Sakellariou et al., 2007).

Moving eastwards in the Alkyonides Gulf (Figure 17), there is the north-dipping West Alkyonides Fault with a length of 7km. This fault is a low angle one with a dip angle of 25-30°. The difference in the dip angle between the West Alkyonides fault and the Strava fault is mainly attributed to the different mechanical properties of the lithology (Sakellariou et al., 2007).

The south margin of the Alkyonides Gulf is lastly characterized by the NE-dipping high angle East Alkyonides Fault that has a length of 8km (Figure 17). The East Alkyonides fault lies in a N50-60° direction and has a dip angle of 45°. Eastern of the East Alkyonides fault lies the north-dipping normal Psatha fault and a little northern there is the North and South Mytikas faults that bound the Pateras Mountain to the north and to the south respectively (Sakellariou et al., 2007).

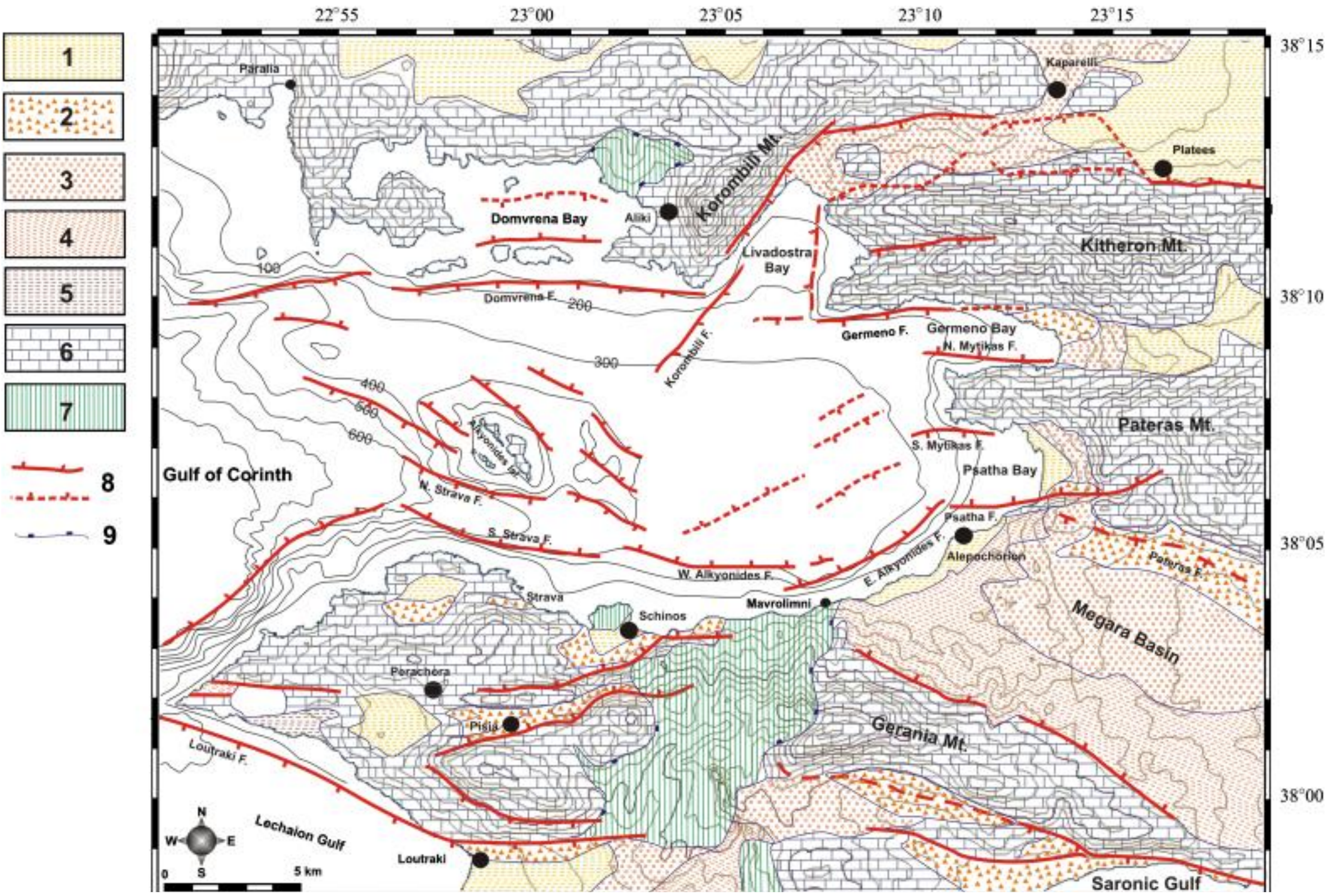

Figure 17. Geological map of the Gulf of Alkyonides (Eastern Corintiakos Gulf Sector) (Sakellariou et al., 2007).

The northern part of the Alkyonides basin is basically composed by the Livastrova and the Germeno bays (Figure 17). These two bays are connected with the south-dipping Germeno fault which has a dip angle of 40-45°. At the western tip of the Germeno fault, southern of the Livadostra basin, there is a tectonic horst on the base of which lies a faulted basement ridge (Sakellariou et al., 2007).

West of the Livastrova basin lies the offshore extension of the Korombili fault which has a N30° direction and a SE trending dip. Yet the major fault that controls the northern margin of the Alkyonides basin is the Domvrena Fault. The Domvrena fault has a 12km length and it is a south-dipping high angle (40-45°) fault. On the footwall of the Domvrena fault lies the Domvrena bay (a 200m deep basin) which is limited by a north-dipping high angle fault and its opposite south-dipping one (Figure 17). On the other hand, the hanging wall of the same fault is controlled by several NW-SE trending faults (Sakellariou et al., 2007).

Apart from those major faults there are also several minor faults that characterize the Alkyonides basin with SW-NE direction and a total displacement that never exceeds a few tens of meters (Sakellariou et al., 2007).

South-West of the Alkyonides basin lies the Perahora Peninsula. The Perahora Penisnula is bounded by the Loutraki and the Perahora fault (Figures 16 and 17). The Perahora fault has a NE direction and near the seafloor exhibits a high-angle of 54° that decreases greatly while moving to the basement, reaching the 33°. The Perahora fault continues further into the Lechaion basin. The Loutraki fault is a southdipping high-angle fault with a dip angle of 45-50°. Except from those two major faults, there are also several minor normal faults both north and south-dipping that are spread in the Perahora Peninsula. Many of those superficial faults are thought to have been activated during the 1981 earthquakes. Last but not least the Lechaion basin is composed of several south-dipping faults and thick north-dipping sediments. The Loutraki fault seems to be the geological boundary between the Perahora Peninsula and the Lechaion Basin (Taylor et al., 2011).

3. Introduction to seismic arrays

3.1. Definition and Details

A seismic array is defined as a set of seismometers placed at specific points in order to create the proper formation (Rost and Thomas, 2002; Havskov and Alguacil, 2004). In general, a seismic array should consist of at least three sensors deployed in a way so that their minimum distance always exceeds 1 km yet is always less than 200km and the minimum aperture between two successive seismometers is 2km. In this way, the ratio signal to noise is increased, producing coherent signal for analysis (Rost and Garnero, 2004). Of course, such array parameters are determined upon the budget and the purpose of the study (Schweitzer et al., 2002). All of the sensors should also be characterized by the same specifications in order to record in the same way and have a common time reference point so as to be synchronized (Rost and Garnero, 2004; Havskov and Alguacil, 2004).

Based on the proposals made by Asten and Henstridge in 1984, an array's configurations is considered to be effective only when the number of the sensors that are included in the array is higher than the number of the distinctive waveforms (both signal and noise) that can be recorded at the same time, while the sensors' distance is smaller than the half of the shortest wavelength and the total diameter of the array is equal in length to the largest recorded wavelength (Havskov and Alguacil, 2004).

As far as the shape of the configuration is concerned, it is greatly depending on the purpose of the study. For instance, if data are derived from a wide range of azimuths then the array's shape should be like one circle or more than one in concentric shape. If the data are derived from a limited area, then the array may have a semicircular shape (Havskov and Alguacil, 2004).

In practice, after carefully considering the above characteristics, one can say that the main difference between the results extracted by a seismic array and those extracted by a local network is attributed to the use of different analysis techniques. That is to say that the data derived from a seismic array can be analyzed with techniques used for local networks while every local network can, under certain circumstances, be used as a seismic array (Schweitzer et al., 2002).

A seismic array is mostly used nowadays in order to detect a seismic epicenter using data without obvious P and S onsets (Rost and Thomas, 2002; Schweitzer et al., 2002; Havskov and Alguacil, 2004) since it can greatly increase the signal coherency of the waveform. It can also provide information about seismic parameters such as the azimuth of approach and apparent velocity (Havskov and Alguacil, 2004). Such deployments have also been widely used in order to determine the source of volcanic tremor as well as several seismic wave-field properties in regions with volcanic activity (Schweitzer et al., 2002; Havskov and Alguacil, 2004). In this way, these well positioned stations can provide useful information for studying small structures of the Earth's crust, mantle, inner core and core-mantle boundary (Rost and Thomas, 2002; Rost and Garnero, 2004) as well as tomographic Figures of high resolution for regional analysis (Rost and Thomas, 2002). Apart from these, such deployments are also used in order to study the propagation of seismic waves near, far from the seismic source and in the sensor's area (Havskov and Alguacil, 2004).

Despite the aforementioned applications and uses of such deployments, seismic arrays were originally introduced in 1958 in order to locate and track down nuclear explosions worldwide (Rost and Thomas, 2002; Schweitzer et al., 2002; Havskov and Alguacil, 2004). However it wasn't until 1990 that many of these deployments became known. Some of these arrays worldwide are KURK (Kurchatov, Kazakhstan), ILAR (Eielson, Alaska), ESDC (Sonseca, Spain), CMAR (Chiang Mai, Thailand), BRTR (Keskin, Turkey), ASAR (Alice Springs, Australia) and AKASG (Malin, Ukraine). The aperture's geometry differs among those arrays while their installation depends on the signal's period (Schweitzer et al., 2002).

3.2 Advantages and disadvantages of seismic arrays

The first and primary advantage of a seismic array is that it enables the increase of the signal to noise ratio (SNR), as already mentioned, due to stacking and forming a final beam (Rost and Thomas, 2002). The theoretic background behind this feature is based on the fact that stations situated in nearby regions tend to provide us with similar seismograms. The seismic waves that are recorded from stations that are close have travelled almost the same path, have met almost the same structures and thus the observed final time delay is slight. As a result, the difference among the seismograms can only be attributed in delay (which is relatively small) and background noise (Havskov and Alguacil, 2004).

In order to increase the SNR, the time delay was firstly removed and when all of the signals are in-phase the final beam was formed by stacking the waveforms. Having removed the time delay before stacking them enhances only the different seismic phases, since noise shows incoherency among the stations and is decreased (Rost and Garnero, 2004). This technique can also be effective even when local noise is present since its apparent velocity and azimuth will be different from the signals (Havskov and Alguacil, 2004).

The enhanced SNR also gives us the chance to detect phases that wouldn't be seen otherwise and several of their parameters such as period and travel time (Rost and Thomas, 2002; Rost and Garnero, 2004). The fact that the time delay is removed before creating the beam also enables us to study phases that are recorded at the same time (such as core phases like PKP) (Rost and Garnero, 2004).

What is more, by using a seismic array, the directivity of the waveform and as a result the location of the epicenter can be identified more easily (Rost and Thomas, 2002; Rost and Garnero, 2004). This is possible when the array is larger than the horizontal wavelength of the oscillation since then and only then the slowness is equal to the vertical incidence angle and the back azimuth is given by the horizontal angle (Rost and Garnero, 2004). Moreover, in large scale, a seismic array can provide us with high resolution tomography as already mentioned (Rost and Thomas, 2002).

Despite all the aforementioned advantages such a deployment is also characterized by great disadvantage. The main drawbacks upon many are that its maintenance as well as its installation is really costly (Rost and Thomas, 2002).

4. Methodology

4.1. Parameters studied

Applying the techniques that are usually used for seismic arrays, the two parameters of the wave's propagation that are studied in detail are:

a) Slowness (u) and

b) Backazimuth (Φ).

Slowness is stable regarding a specific ray (Schweitzer et al., 2002) and is derived from the equation u=1/Vapp=sin i/Vo, where Vapp is the apparent velocity and Vo is the medium velocity under the array (Rost and Thomas, 2002; Havskov and Alguacil, 2004). Since slowness is the inverse of the apparent velocity, it is most correctly called apparent or horizontal slowness. Both of these interdependent parameters (apparent velocity, apparent slowness) should not be confused with velocity or slowness (Havskov and Alguacil, 2004). Apparent slowness is measured in s/km when studying regional events or in s/˚ for teleseismic applications (Schweitzer et al., 2002). As one can easily notice, by knowing the slowness of the wave and the medium velocity beneath the array, one can extract information about the angle of incidence in the vertical plane (i) and vice versa (Rost and Thomas, 2002). Vertical incidence angle (i) is defined as the angle between the vertical plane and the direction towards the source and it cannot exceed the 90˚ (Schweitzer et al., 2002).

Backazimuth is defined as the angle of the arriving wavefront and it can be found by measuring clockwise the angle between the North and the epicenter's direction. Backazimuth is calculated in degrees (˚)(Rost and Thomas, 2002; Schweitzer et al., 2002).

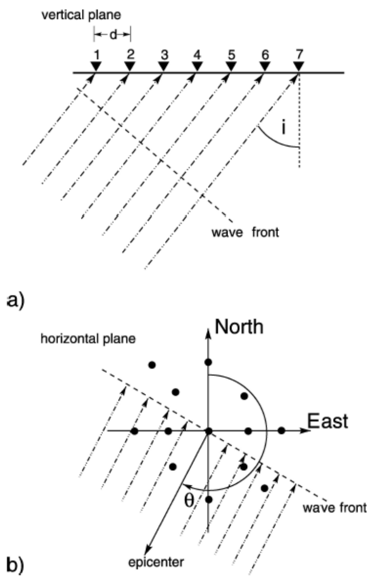

Figure 18. (a) The wavefront's angle of incidence in vertical plane and (b) The arriving wavefront in horizontal plane along with the backazimuth (Schweitzer et al., 2002).

4.2 Detection Processing

Both of the aforementioned parameters are derived from the analysis of the waveforms that are recorded from the seismic array. Yet, since the recording from the seismic array is continuous, there is a procedure followed in order to detect the seismic signals in daily recordings. This procedure is based on the fact that data are composed of recorded noise and signal stacked with noise. The signal of a recorded earthquake is different compared to the background random noise since it usually has greater amplitude, different for each phase but beforehand known frequencies, different shape and greater coherency. As a result, assuming that the recorded data are independent measurements of a zero-mean Gaussian random variable, signal plus noise is distinguished from random noise by calculating the power within a specific time period. The signal is located in those time windows where the calculated power exceeds the predefined threshold (which is neither stable through time nor always accurate) (Schweitzer et al., 2002).

Based on the above, the most common technique for seismic arrays is to calculate the power within two different time windows characterized by different time intervals. The one's interval should be long (LTA) and the other's short (STA). The parameter compared to the predefined threshold is the ratio STA/LTA that coincides with the signal-to-noise ratio (SNR). When this ration exceeds the threshold, there is signal (Schweitzer et al., 2002).

The parameter STA is given by the following equation:

$$\mathrm{STA(t)} = \frac{1}{\mathrm{L}} \cdot \sum_{\mathrm{j}=0}^{\mathrm{L}-1} |\mathrm{w(t-j)}| \text{ [1]}$$

where L=sampling rate·STA window length, while the parameter LTA is equal to:

$$\mathrm{LTA(t)} = 2^{-\varsigma} \cdot \mathrm{STA}(\mathrm{t}-\varepsilon) + (1-2^{-\varsigma}) \cdot \mathrm{LTA}(\mathrm{t}-1) \text{ [2]}$$

where ε is the symbol for time delay (few seconds) and ς is a steering parameter for the LTA update rate (Schweitzer et al., 2002).

4.3 The methodology of beam forming

Beamforming is mostly used in order to increase the SNR and distinguish signal from random noise in the recorded waveforms. Since the signals derived from different stations are different in P onset and maybe in the recorded noise, one should remove the time delays from all the signals of a specific backazimuth and slowness before constructing the beam in order for it to be effective (Rost and Thomas, 2002; Schweitzer et al., 2002). The best way to remove the time delay is to set the P onset on every station and then move the traces of all the stations with respect to the P-onset pick of the station which is located in the centre of the array (Schweitzer et al., 2002) (Figures 19 and 20).

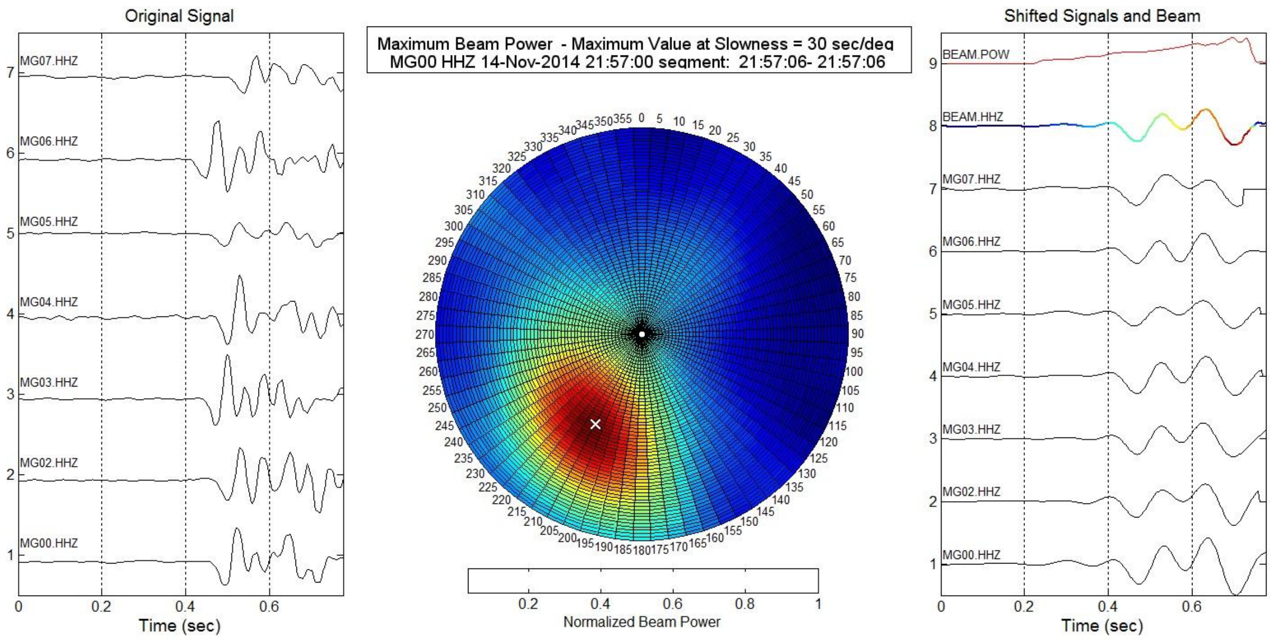

Figure 19. Left: The original signals from all the stations of the seismic array for an event that took place on the 14th of November 2014, 21:57. Right: The sifted signals, without time delay, along with the beam and the power beam, filtered with a bandpass filter (2-10Hz).

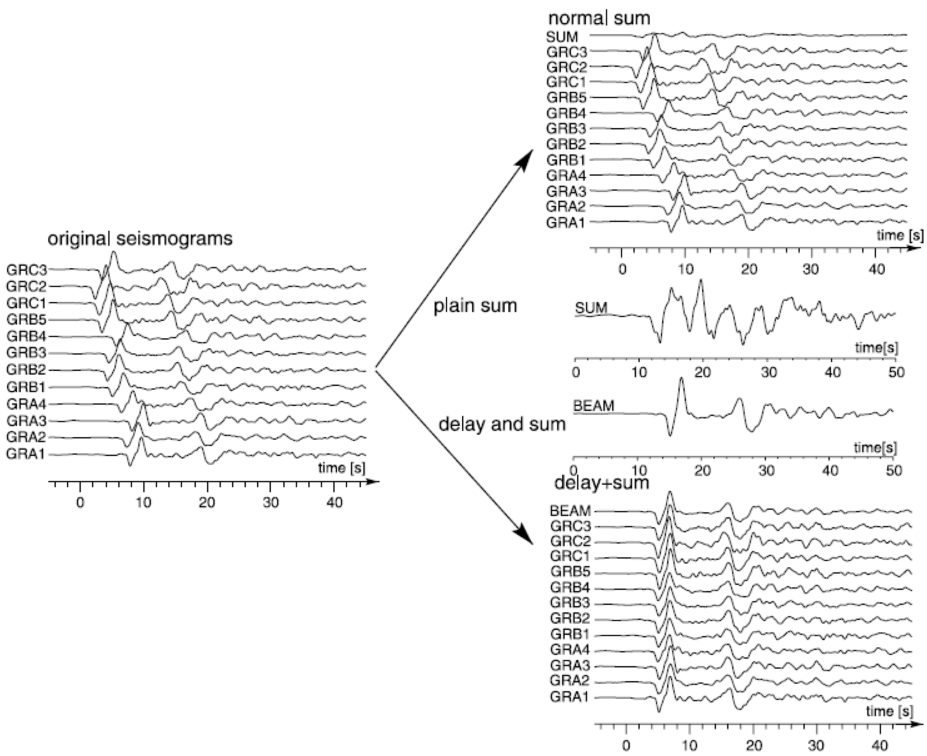

Figure 20. Left: The original signals from all the stations of the Grafenberg array for an event that took place on the 2nd of October 2000, 21:57. Right (top): plain sum and Right (bottom): shifted signals and sum. The most representative beam is derived after shifting the signals (Rost and Thomas, 2002).

In case there is a lot of noise and the picking of the P-onset is a difficult task, or when there is workload and limited time, one can form a set of predefined beams. Each of these predefined beams is characterized by different amplitude and slowness. The best beam is the one whose combination of slowness and backazimuth gives the highest power on the beam (Schweitzer et al., 2002).

When installing a seismic array, there should always be a reference point in the centre of the array which can either be an instrument or just the geometrical centre. Based on that, the location of all the array's sensors can be described by a parameter rj whole absolute value gives the exact three dimensional distance between the centre of the array and the specific sensor. Provided that there is a sensor in the centre of the array, then the recorded by that sensor waveform would be described by the following equation:

$$\mathrm{Xcenter(t)} = \mathrm{f(t)} + \mathrm{ni(t)}, [3]$$

where f(t) is the time series for signal and ni(t) is the time series for noise (Rost and Thomas, 2002).

Since each seismic station has different location, the same wave front will arrive in different times, resulting in the noticeable time delays. These time delays are associated with travel time differences whole value depend on the distance between the sensor and the epicenter and the phases' slowness (Rost and Thomas, 2002). Based on that fact, the recorded waveform by a station I would be described by the following equation:

$$\mathrm{x_i(t)} = \mathrm{f(t - r_i . \cdot u_{hor})} + \mathrm{n_i(t)}, [4]$$

Where u_{hor} is the apparent slowness of the propagating wave front and r_i is the location of that sensor (Rost and Thomas, 2002).

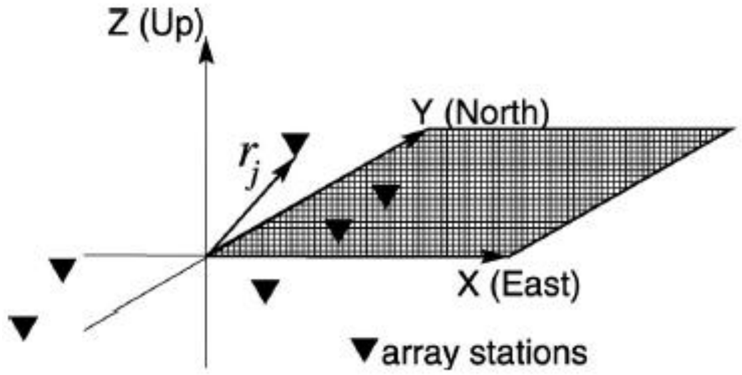

Figure 21. The location of several sensors that are part of a seismic array. The center of the coordinate system coincides with the reference point of the array (Rost and Thomas, 2002).

As already stated in order to apply beam forming, one should firstly remove the time delay from all the stations for a specific backazimuth and slowness. Then the time series would alter taking the following form (Rost and Thomas, 2002):

$$\overline{x_i}(t) = x_i(t - r_i . \cdot u_{hor}) = f(t) + n_i(t - r_i . \cdot u_{hor}), [5]$$

The stacked waveforms after removing the time delay, form the beam trace for an M- component array which is described as:

$$b(t) = \frac{1}{M}\sum_{i=1}^{M} \bar{x}\,(t) = f(t) + \frac{1}{M}\sum_{i=1}^{M} n_i\,(t - r_i\,.\cdot u_{hor})\ [6]$$

Following that procedure, the coherent signal is emphasized while the random noise is suppressed, correlating the method of beamforming as the application of a frequency filter in the waveform. The effectiveness of the method is greatly depending on the number of the array's components, while the increase of the SNR in an array S with several stations compared to the one of a single-station array (s), is approximately calculated by:

$$S \approx \sqrt{M}\, s\ [7]$$

This equation is based on the hypothesis that the signal has the perfect cohesion and that the noise is completely random (Rost and Thomas, 2002).

4.4 Beam forming restrictions

The main requirement for the correct formation of the beam is the use of the correct combination of backazimuth and slowness. Both of these parameters are depending on various factors such as variations of the propagation's velocity for local geological reasons that can alter their value significantly comparing to the theoretical one (Rost and Thomas, 2002). Not taking into account these variations might result in signal distortion or decrease of the signal's amplitude (Rost and Thomas, 2002; Schweitzer et al., 2002). In order to avoid this amplitude decrease, one could weight the traces or normalize the amplitudes before applying the technique (Schweitzer et al., 2002. Apart from that, another serious condition is the similarity and coherency of the signals from all the stations. That is why arrays with very big size or sensors that are not uniformly installed fail to produce scientifically acceptable results using the technique of beam forming (Rost and Thomas, 2002).

4.5 F-K Analysis

The major difference of the frequency-wave number analysis is that it can calculate both the horizontal slowness (u) and the backazimuth (θ) simultaneously, by measuring the power that corresponds to different sets of slowness and direction. This takes place in the frequency domain so as to save time from extra calculations. The correct set of horizontal slowness and backazimuth is the one that produces the highest amplitudes of the recorded summed signal (Rost and Thomas, 2002).

As already discussed above, the signal that is recorded in a seismometer with location vector r_i is described by the following equation (without taking noise into account):

$$x_i(t) = f(t - r_i . \cdot u_{hor}), [8]$$

with u_{hor} given by the following equation:

$$u_{hor} = \frac{1}{v_{hor}} (\cos\theta, \sin\theta), [9]$$

In order to calculate the maximum amplitude of the summed signal, all the distinct signal have to be in phase. In other words, the factor of time delay that is recorded in each station and is given by $r_i . \cdot u_{hor}$ should disappear. Based on that, the summed signal is described as:

$$y(t) = \frac{1}{N} \sum_{n=1}^{N} x_i(t + r_i . \cdot u_{hor}), [10]$$

A signal with a different slowness vector is computed by:

$$y(t) = \frac{1}{N} \sum_{n=1}^{N} x_i(t + [(u_{hor} - u)] r_i .], [11]$$

As a result, the total energy of the summed signal can be derived, using the integration of the squared summed amplitudes over time and Parseval's theorem:

$$E(k - k_0) = \int_{-\infty}^{\infty} y^2(t)dt = \frac{1}{2\pi} \int_{-\infty}^{\infty} |S(\omega)|^2 \left| \frac{1}{N} \sum_{n=1}^{N} e^{2\pi i * (k - k_0) * r_i} \right|^2 d\omega, [12]$$

with S(ω) being the Fourier transform of s(t) and k is the wave number vector given by the following equation:

$$k = (k_x, k_y) = \omega * u = \frac{\omega}{v_0} (cos\theta, sin\theta) [13]$$

The vector k_0 corresponds to u_0. The wave number is of great importance since its direction is determined by the backazimuth and its magnitude is a result of the slowness.

The equation [12] can also be written as:

$$E(k - k_0) = \frac{1}{2\pi} \int_{-\infty}^{\infty} |S(\omega)|^2 |A\ (k - k_0)|^2 d\omega, [14]$$

Where $|A\ (k - k_0)|^2 = \left| \frac{1}{N} \sum_{n=1}^{N} e^{2\pi i * (k - k_0) * r_i} \right|^2$ is the array response function (ARF). The ARF is determined by the geometry of the array (interstation spacing, configuration and aperture). So, based on the above, the slowness is given by the wave number vector $k=(k_x,k_y)$:

$$|k| = (k_x^2 + k_y^2)^{1/2} = \frac{2\pi}{u_s} = \frac{\omega}{v_s} [15]$$

Where v_s is the apparent horizontal slowness. The backazimuth is given by:

$$\theta = \tan^{-1}\left(\frac{k_x}{k_y}\right). [16]$$

The different sets of slowness and backazimuth form the fk diagram, which has polar coordinate system. In this diagram the azimuthal axis corresponds to the backazimuth while the radial axis corresponds to the slowness (Figures 22 and 23) (Rost and Thomas, 2002).

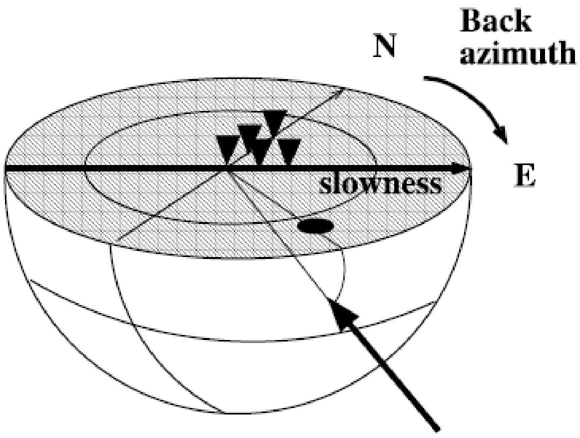

Figure 22. Fk diagram. An incident wave travels through an imaginary half sphere beneath the array at point (X). The fk diagram corresponds to the projection of that half sphere. Slowness is given by the distance of the maximum energy from the origin while the angle from north is the backazimuth (Rost and Thomas, 2002).

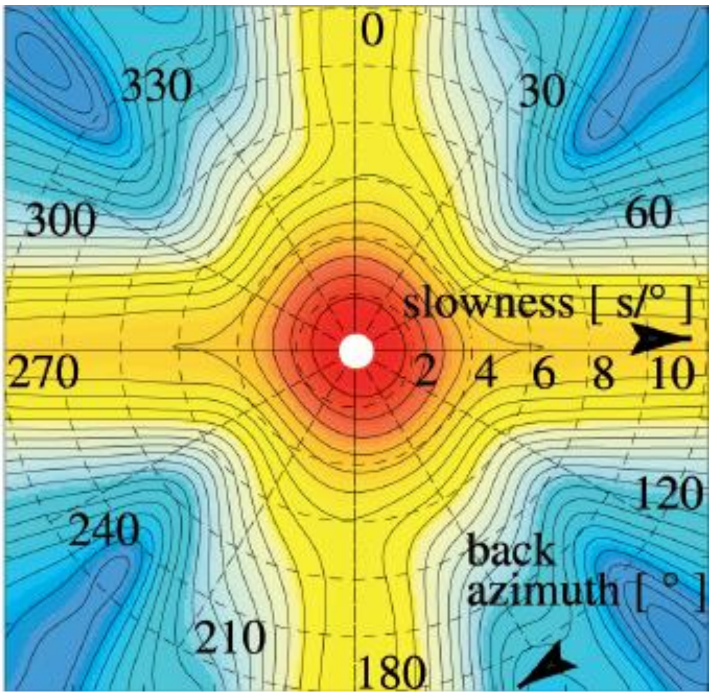

Figure 23. An fk diagram (Rost and Thomas, 2002).

4.6 F-K Analysis Restrictions

The application of this method should be conducted in relatively short time-windows in order to reassure that the calculated slowness in unique and corresponds to one specific phase. Having a long-time window arises the danger of making the identification of a specific phase impossible. In other words, the fk technique is best used in arrays whose recorded signal shows a really small time delay. This problem can be overcome by carefully selecting the time window for the application of the method. Last but not least another restriction of the method is that it is based on the assumption that there are no heterogeneities beneath the recorders which is almost inevitable and can change the results given (Rost and Thomas, 2002).

4.7 Epicenter Location

4.7.1 The Lomax Method

Having acquired the two parameters of each event (slowness and azimuth), the epicenter can be derived from a two-stage procedure. The first part is the calculation of the S-P time using the S and P arrivals from the last procedure. After that a non-linear probabilistic earthquake location methodology and algorithms are used for the determination of the epicenter (Lomax et al., 2000) (APPENDIX I). More specifically the algorithm reads the velocity model which is used as a grid with multiple cells each of which has a specific velocity value. Using that it calculates travel times for every different cell and the station and it forms new grids with many different travel times (one for every cell). The algorithm stores one grid for every station. The time calculation is based on a wave equation using the method of Podvin and Lecomte (1991). In order to calculate the exact arrival time of the wavefront it is assumed that it only depends on the arrival times of the neighboring cells. Thus, if the arrival times in all the neighboring cells in a 3-D model are known, we can assume the arrival time in the central one without knowing the epicenter (Podvin & Lecomte, 1991). Based on the Huygens theorem, every neighboring cell sends a pulse the time that the wavefront arrives. The first of all those pulses that will reach the central cell is the one that corresponds to the first time arrival. In this way a grid with all the first-time arrivals for every cell is formed (Alomax.free.fr, 2017).

Using that grid and the probability density function (PDF) the epicenter can be calculated. The algorithm receives with a non-linear way a sum of places that form space around the hypocenter with the best fit. The probability density function is calculated by an algorithm in two different ways (Alomax.free.fr, 2017).

The first one uses the least square method (Tarantola &Valette, 1982) and it is described by the following equation:

$$pdf(x,t_0) \propto kexp\left(-\frac{1}{2}\sum_{obs_i}\frac{[Tobs_i(x)-Tcalc_i(x)]^2}{\sigma_i^2}\right) [17]$$

where $Tobs_i$ is the observed arrival time at the station (i) and the $Tcalc_i$ is the theoretically calculated time, σ is the standard deviation and k is a normalization factor.

The second one uses the equal differential Time (EDT) method (Zhou, 1994) which is based on the hyperbola method (Milne, 1886) and it is described by equation 18:.

$$pdf(x) \propto k \left[\sum_{obs_a obs_b} \frac{1}{\sqrt{\sigma_a^2+\sigma_b^2}} \exp\left(- \frac{\{[Tobs_a(x) - Tobs_b(x)] - [TTcalc_a(x) - TTcalc_b(x)]\}^2}{\sigma_a^2+\sigma_b^2} \right) \right]^N \quad [18]$$

where ***T***obs is the observed arrival time at the stations (a and b) and the ***TT***calc is the theoretically calculated time. The epicenter is probably where the exponent takes the value 1, i.e. when the difference between the observed and the calculated time is zero. This methodology is applied in every different pair of stations and the effect of those who seem to have systematic errors, in the final solution is minimized. The best hypocenter is given by the non-linear method Oct-Tree. In this method, the PDF is calculated for every different cell of the grid. The cell with the biggest value is subdivided into 8 new cells and then it calculates the new probability factors for every one of these new cells. This procedure is repeated until a fair solution is given or after a specific number of repetitions which is predetermined (Figure 24) (Alomax.free.fr, 2017).

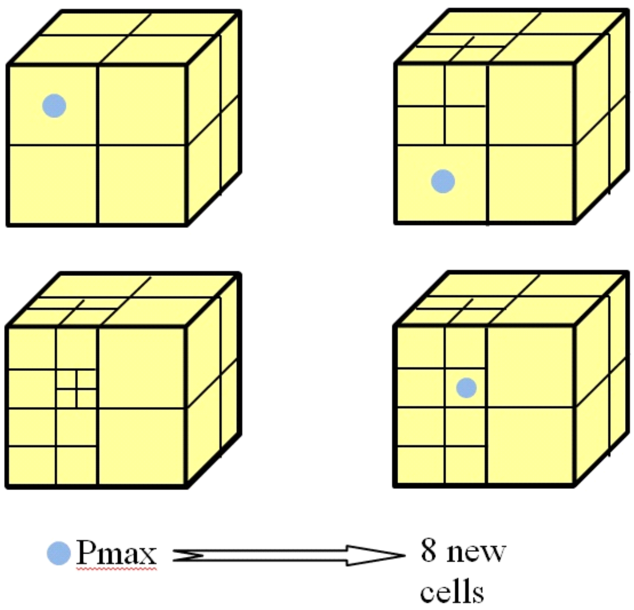

Figure 24. The Oct-Tree methodology (schematics) (Alomax.free.fr, 2017).

4.7.2. Array – depending calculation method

The second method which can be used to calculate the epicenter is only depending on the parameters acquired from the seismic array. Knowing the slowness from the aforementioned techniques, firstly we calculate the incidence angle based on the P and S propagation velocity beneath the surface. After that, based on that angle of incidence and the pre-calculated backazimuth, we calculate the path of the wavefront based on the given velocity model. This path is acquired by the use of the Snell law for every consecutive layer. After that the P and S travel times are calculated, assuming that the travelled on that specific path. The ratio Vp/Vs should be stable throughout this procedure, in order for both waves to travel on the same path. The best hypocenter is the one that results in P-S times closer to the ones that were derived from the synthetic seismograms so as to have increased accuracy due to the high ratio of SNR.

The main advantage of such a method is that it only depends on the parameters of the seismic array, yet its major disadvantage is that it is very sensitive when it comes for the velocity model. Every slight change of the method can lead to huge errors.

4.7.3. The hybrid method

In this study a combination of those two techniques was used in order to extract the hypocenter. In other words, after running both procedures simultaneously we obtain some possible hypocenters from the first methodology and the travel times of the ray path as they were calculated by the second procedure. The ray path of the wavefront should be in the same area where the possible hypocenters from the 1st method have been calculated. The point on the ray path that is characterized by the maximum possibility is considered to be the optimum hypocenter.

Yet the outcome of the program is the distance between the epicenter and the central station of the array and not the actual coordinates. Thus, the distance is transformed into degrees and then they are added to the coordinates of the central station (APPENDIX II). The maps are created using the GMT program (Alomax.free.fr, 2017).

4.7.4 HYPOSAT

In order to minimize the errors caused in the procedure of locating the event using the parameters of azimuth and slowness, another method is also utilized and the acquired results were compared to the epicenters as they were calculated by the Seismology lab of the Kapodistrian University, Athens. More specifically, I used the HYPOSAT program (version 4.4b, 2003).

The initial parameters used in this program are the arrival times of the first onsets along with backazimuths and slownesses (or apparent velocities). Apart from these, travel-time differences between phases observed in the same station are also used, mostly in case of the existence of surface reflections (pP or sP) in order to locate the exact depth. They can also be used in case there is only one station and the only input parameters are the P and S onsets as well as the azimuth. By taking into account this extra parameter the uncertainties of the model which is used are also minimized (Schweitzer, 1997).

As mentioned above, in order for the program to proceed in the inversions, a local velocity model, the coordinates of the stations as well as the observed arrival times of all phases and the observed azimuth and slowness are of great importance and comprise the data input. A file containing the data for the calculation of the ellipticity corrections is also needed (Schweitzer, 1997).

Firstly, HYPOSAT calculates an initial epicenter. This is acquired just by using all the available azimuth data with which it calculates a mean solution of all crossing azimuth lines. Alternatively, it uses a single S-P travel time difference along with the azimuth observed at the same station. Last but not least, if all the aforementioned methods to calculate an initial solution fail, then a starting epicenter is guessed taking into account either the coordinates of the closest station or the central point of the station net (Schweitzer, 1997).

In order to derive the location of the event, the equation system used in HYPOSAT is solved with the Generalized – Matrix – Inversion (GMI) technique which uses the Single – Value – Decomposition algorithm (SVD) as published in Press et al. (1992). All the partial derivatives that are derived from the program are recalculated several times until the difference between two consecutive solutions is below a predefined limit. It is really crucial that the input parameters are weighted before used, so as to maintain almost intact the well defined ones during the iterations (Schweitzer, 1997).The system of equations to be solved has the following form:

$$\begin{bmatrix} 1 & \frac{\partial t_1}{\partial lat} & \frac{\partial t_1}{\partial lon} & \frac{\partial t_1}{\partial z_o}\cdots \\ 1 & \frac{\partial t_i}{\partial lat} & \frac{\partial t_i}{\partial lon} & \frac{\partial t_i}{\partial z_o} \\ 0 & \frac{\partial dt_1}{\partial lat} & \frac{\partial dt_1}{\partial lon} & \frac{\partial dt_1}{\partial z_o}\cdots \\ 0 & \frac{\partial dt_j}{\partial lat} & \frac{\partial dt_j}{\partial lon} & \frac{\partial dt_j}{\partial z_o} \\ 0 & \frac{\partial p_1}{\partial lat} & \frac{\partial p_1}{\partial lon} & \frac{\partial p_1}{\partial z_o}\cdots \\ 0 & \frac{\partial p_k}{\partial lat} & \frac{\partial p_k}{\partial lon} & \frac{\partial p_k}{\partial z_o} \\ 0 & \frac{\partial azi_1}{\partial lat} & \frac{\partial azi_1}{\partial lon} & 0\cdots \\ 0 & \frac{\partial azi_l}{\partial lat} & \frac{\partial azi_l}{\partial lon} & 0 \end{bmatrix} \cdot \begin{bmatrix} \delta t_o \\ \delta lat \\ \delta lon \\ \delta z_o \end{bmatrix} = \begin{bmatrix} \Delta t_1\cdots \\ \Delta t_i \\ \Delta dt_1\cdots \\ \Delta dt_j \\ \Delta p_1\cdots \\ \Delta p_k \\ \Delta azi_1\cdots \\ \Delta azi_l \end{bmatrix}$$

where

$t_{1,i}$ - i travel times and their residuals $\Delta t_{1,i}$

$dt_{1,j}$ - j travel-time differences between two phases observed at the same station and their residuals $\Delta dt_{1,j}$

$p_{1,k}$ - k observed ray parameters (or apparent velocities) observations and their residuals $\Delta p_{1,k}$

$azi_{1,l}$ - l observed azimuth (from station to epicenter) observations and their residuals $\Delta azi_{1,l}$

δt_o - the calculated change in the source time for one iteration

δlat - the calculated change in the latitude for one iteration

δlon - the calculated change in the longitude for one iteration

δz_o - the calculated change in the source depth for one iteration (if not fixed)

4.8 Maps

All the epicenters acquired by the aforementioned methodologies are depicted in maps using the GMT program, so as to be compared and draw our final conclusions concerning the validity of the results and the effectiveness of this specific seismic array.

5. Data

In order to investigate the accuracy in the determination of an earthquake's epicenter using the aforementioned methodologies, we detected all the earthquakes that took place in the time period from 2nd November 2014 to 4th December 2014. This time period corresponds to an earthquake swarm that took place in the area of NW Gulf of Corinth. The data for investigation were narrowed down to this multiplet cluster so as to use events that are characterized by the same focal mechanism and produce similar waveforms. In this way the factor of different local geological structures would be eliminated and in the end this research could provide us with trustworthy results on a specific geological background. This method of utilizing and choosing of data set has long been used and proposed when trying to relocate events by several researchers (Fremont and Malone, 1987; Papadimitriou et al., 1993; Waldhauser, 2009).

During that period almost 400 earthquakes were recorded in the area of interest. During the first stage of our analysis, which was the beamforming and the f-k analysis, 210 earthquakes were excluded from the investigation due to the recorded noise and the difficulty to identify the P and S onsets, issues that would jeopardize the validity of our investigation. Thus, the final catalogue which was used throughout this first stage was comprised by 190 earthquakes. The epicenters of those events were calculated with the Lomax algorithm. From those earthquakes 59 more were excluded after the calculation of their epicenter due to their significantly small size and the fact that they could not be traced in the relative catalogue of the National and Kapodistrian University of Athens. Including those 59 events in the final maps would make the comparison of this study's results with the university's catalogues inevitable, so, the Lomax algorithm was applied to 190 earthquakes (Figures 37-41) but only 141 of them were compared with the HUSN results in Figures 42-45.

As far as the second location technique is concerned (HYPOSAT), that was applied on 139 earthquakes from the initial list. Those earthquakes were the ones that were also found in the University catalogues so as to be able to compare the results afterwards. The two excluded events were turned down due to their huge error in the calculation of the epicenter.

6. Velocity model

The velocity model is one of the most important parameters for the accuracy of the results. The initial velocity model that was used throughout this study was the one that Sweeney and Walter had proposed in 1998 (region 17). This model was a general one and could be applied to all Greek regions (Sweeney and Walter, 1998).

Depth	Velocity for P (km/sec)	Velocity for S (km/sec)
0	2.5	1.1
1	4	2.1
3.5	6	3.4
13.5	6	3.7
24.5	7.2	4
34	7.2	4
34	7.9	4.46
100	8	4.46

Table 2. Initial velocity model used for the study.

Yet the initial results were not that promising (as expected with such a general model) so changes were performed. In order to adjust the velocity model we took into account local velocity models about the Corinth Gulf as they were used in studies in the broader area of the Gulf of Corinth (Gautier et al., 2006) and specifically in its western part (Rigo et al., 1996). These models are listed in detail in APPENDIX IV. Yet a combination of those along with some changes proved to be the optimum velocity model for this study. The velocity model that was used is cited below.

Depth	Velocity for P (km/sec)	Velocity for S (km/sec)
0	3.8	2.8
4	5.2	3
7.2	5.8	3.4
8.2	6.1	3.5
10.4	6.3	3.6
15	6.5	3.8
30	7	4
100	7	4

Table 3. Velocity model used for the study.

7. The Magoula seismic array

The array that was used for this study is comprised by 8 stations named MG00, MG01, MG02, MG03, MG04, MG05, MG06 and MG07. Their exact coordinates and elevation is listed in the table below. All of the stations have a TRILLIUM 40 seismometer and a CMG-DM24S6-EAMU digitizer.

Name	Latitude (°)	Longitude (°)	Elevation (m)
MG00	38.4144	21.9467	143
MG01	38.4142	21.9468	143
MG02	38.4149	21.9470	143
MG03	38.4140	21.9460	143
MG04	38.4141	21.9480	143
MG05	38.4155	21.9457	143
MG06	38.4128	21.9462	143
MG07	38.4154	221.948	143

Table 4. The coordinates of the Magoula array.

8. Array Signal Processing

The first step of the process is to calculate the required parameters. In other words, determine the slowness and azimuth for every earthquake. This is accomplished by applying the beamforming technique and the f-k analysis. In order to apply those, I used the algorithm included in APPENDIX III, which runs in MATLAB environment. This algorithm provides the beamforming and f-k results simultaneously.

Before running the procedure some parameters should be defined such as the frequency filters that should be applied on the waveforms, as well as the component that is studied and the maximum and minimum probable borders of the slowness factor considering the f-k analysis. This last parameter is used in order to set a limit for slowness during the repetitive inversions and reduce the errors.

In this specific investigation, the frequency filters that were basically used were bandpass filters of 2-10HZ for the ‘Z-component’ and 0.5-7Hz for the ‘H-Component’. Those limits were based on a signal analysis that was applied on the recordings of an array established at Tripoli (Pirli et al., 2004). Of course, depending on the waveform these filters were appropriately shifted. As far as the beamforming method is concerned, I used the Max Power technique. Before I drew this conclusion, I also tried both of the other techniques, yet the Max Power technique was the one with the most promising results and minimum errors in case of reflections in the waveform.

Following, there is an example of an earthquake that was used during our analysis. That earthquake took place on the 3rd of December 2014 at 08:26:40.950 and was recorded by the Magoula array. The initial waveform of the Z component is shown in Figure 25.

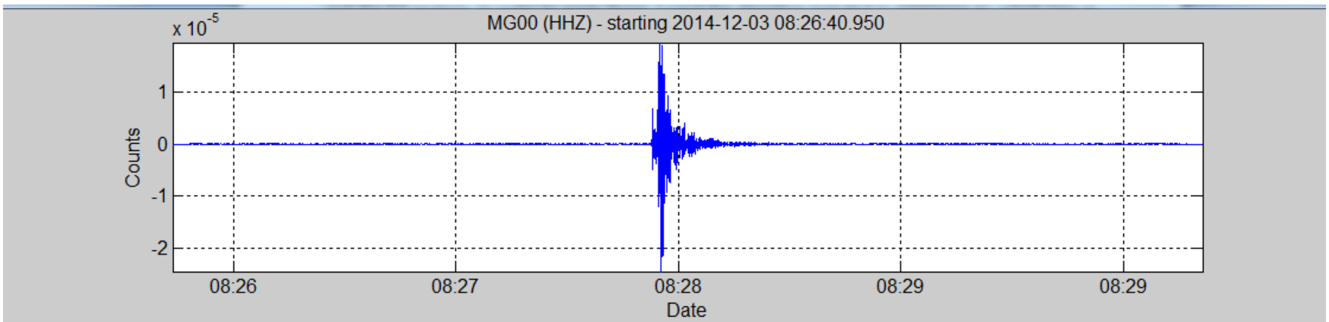

Figure 25. Waveform (Z-component) of the 3-12-2014 earthquake that was recorded by the Magoula array.

The only parameter that should be set now, is the selection of a segment where the P-onset lies. The program selects the point in the waveform that has the biggest aptitude, since that corresponds to the point in the waveform which has the biggest amplitude and it is closest to the P-onset. In case of reflections, when detected, they should be best excluded from the segment since they might cause errors. Reflections are more common in epicentral distances of more than 10° but they might be found in less than that. They are recognized due to the non coherent frequency and amplitude comparing to the rest of the recording and the requested initial phase. The problem of distinguishing reflections from the first arrivals worsens when the earthquakes depth is big. This is because the signal is recorded with attenuation (Tselentis, A., 1997). More specifically, in Figure 26, reflection was not excluded from the segment and the highest amplitude was the one of the reflection. The requested parameters that resulted from the beamforming were slowness 14sec/deg and the azimuth was 152,5 (Figure 27). The corresponding results from the f-k analysis were 13.89 sec/deg and 149,74 (Figure 28).

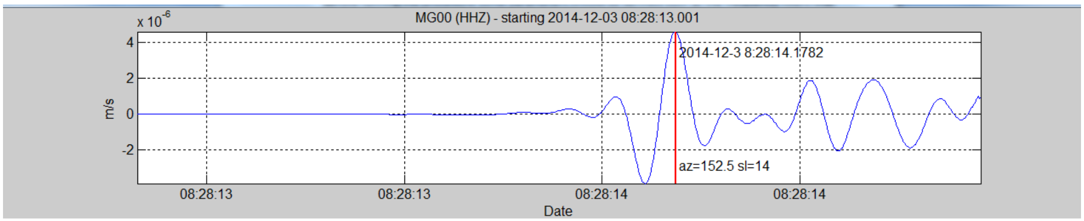

Figure 26. Point in the waveform with the highest power (including reflection).

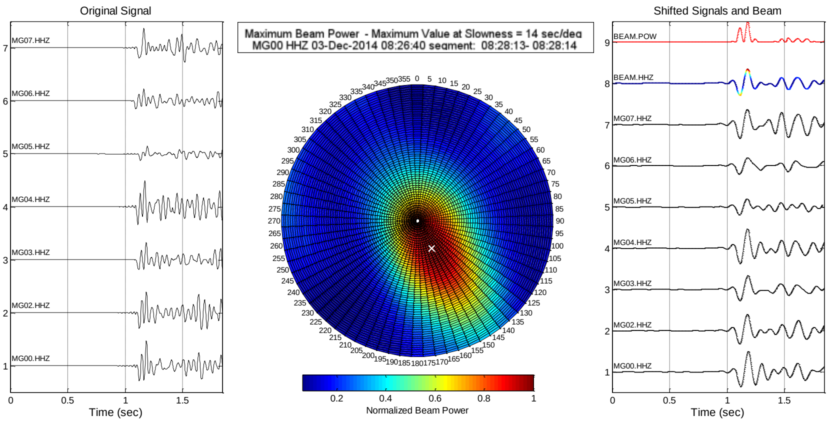

Figure 27. Beamforming results for the 3-12-2014 earthquake (including reflection).

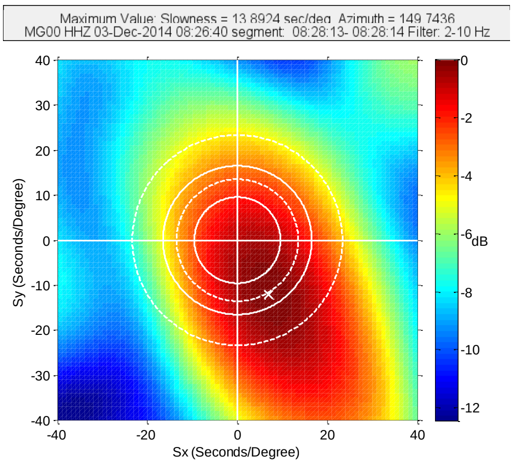

Figure 28. F-k analysis results for the 3-12-2014 earthquake (including reflection).

The same procedure was followed after excluding the segment of the reflection (Figure 29).

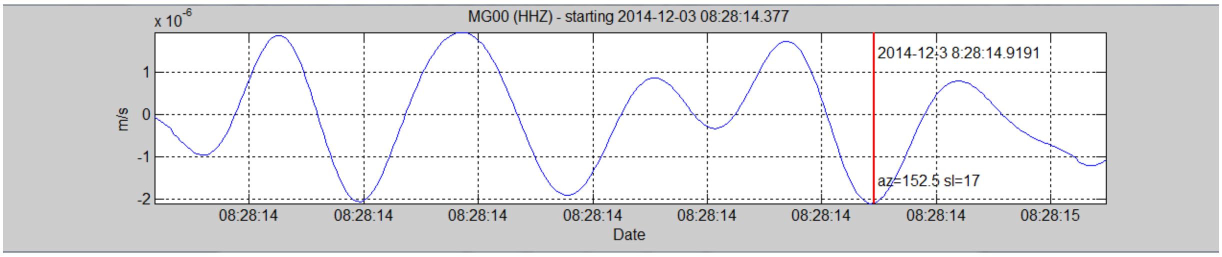

Figure 29. Point in the waveform with the highest power (without reflection).

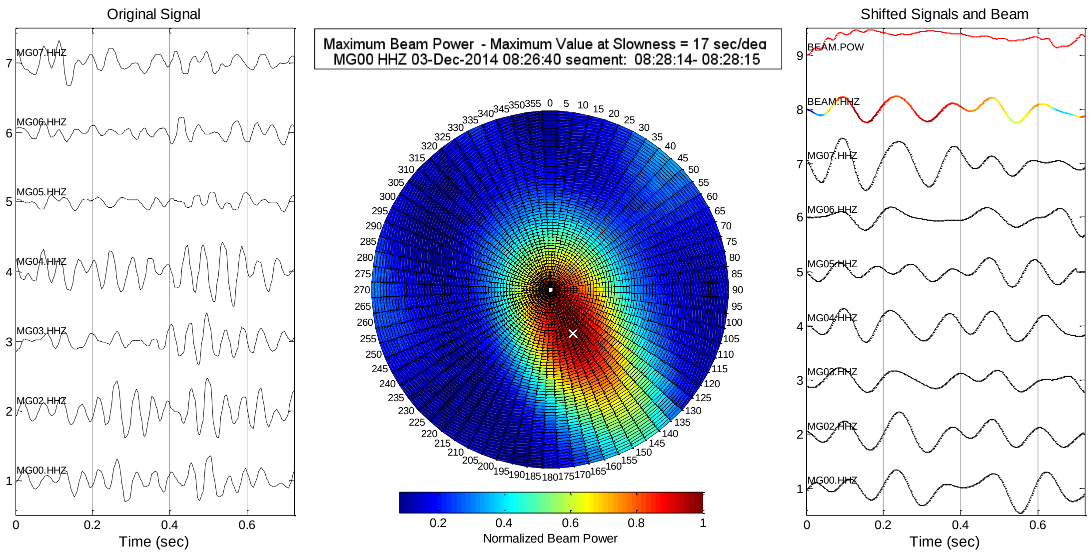

Figure 30. Beamforming results for the 3-12-2014 earthquake (without reflection).

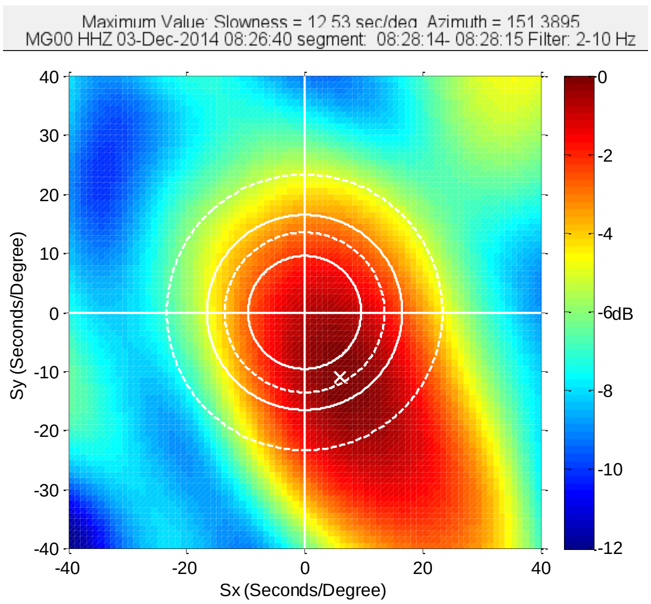

Figure 31. F-k analysis results for the 3-12-2014 earthquake (including reflection).

The requested parameters this time that resulted from the beamforming were slowness 17sec/deg and the azimuth was 152,5 (Figure 27). The corresponding results from the f-k analysis were 12.53 sec/deg and 151,38 (Figure 28). Comparing these two procedures, the azimuth deviation between those two techniques is minimized, while the slowness difference is increased.

The same procedure is followed with the H-component. It is important that the selected segment is the least possible so as to avoid including any phases from surface waves. This is due to the fact that surface waves tend to have bigger amplitudes and as a result higher power. This time there is a different result for the radial component and a different one for the transverse component (Figures 32-36).

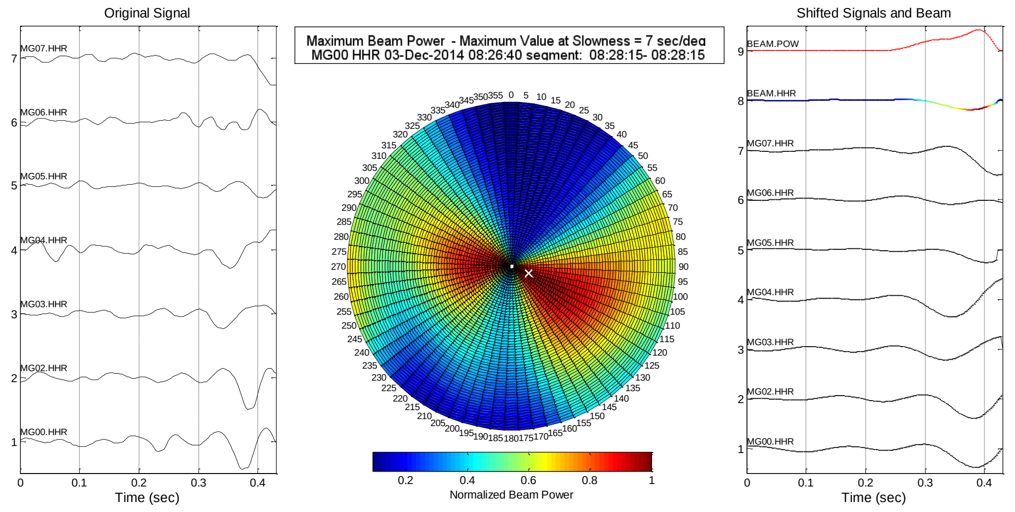

Figure 32. Beamforming results for the 3-12-2014 earthquake (radial component).

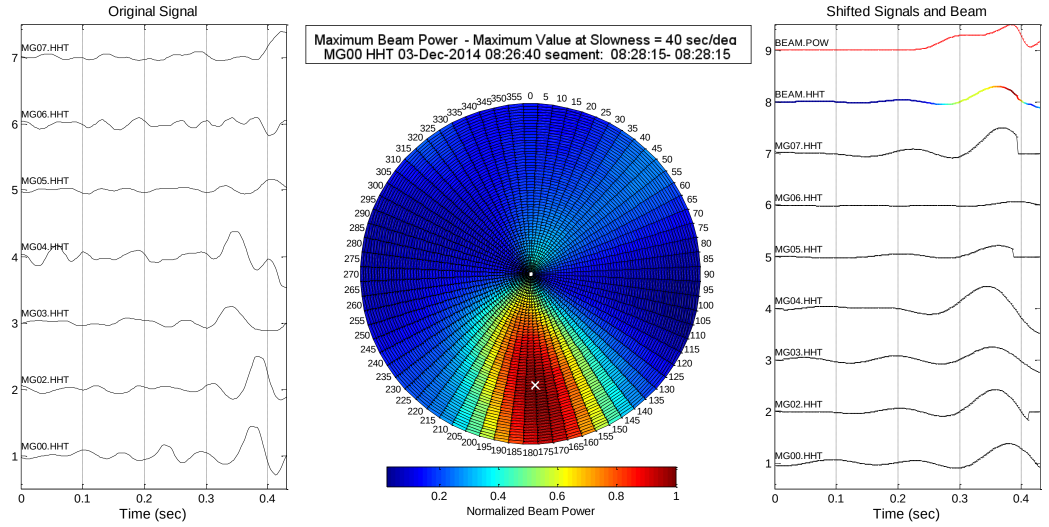

Figure 33. Beamforming results for the 3-12-2014 earthquake (transverse component).

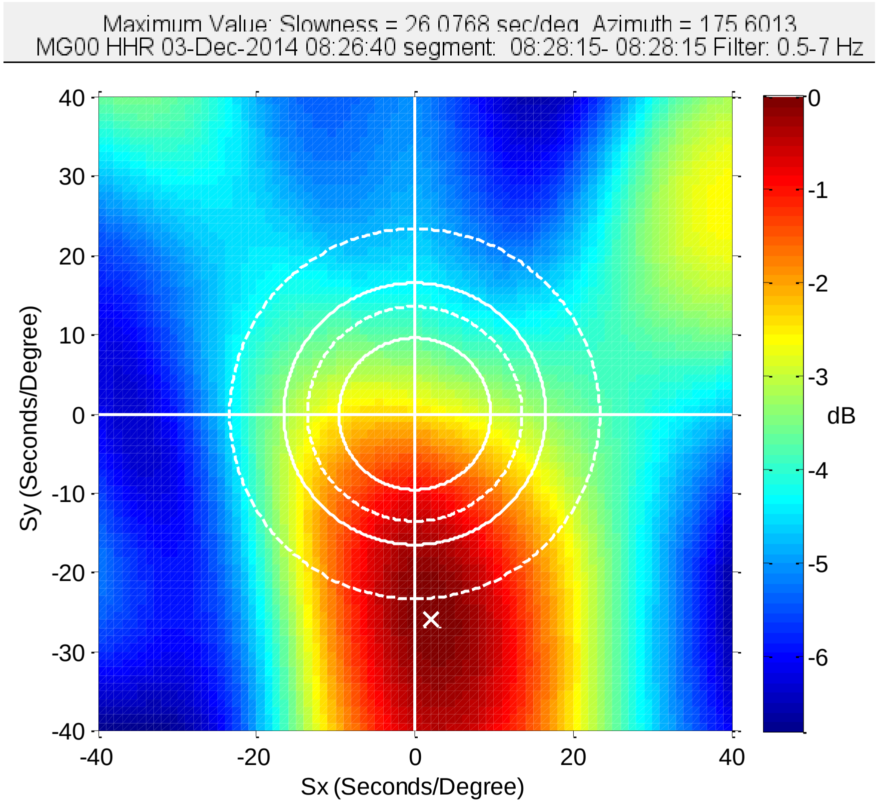

Figure 34. F-k analysis results for the 3-12-2014 earthquake (radial component).

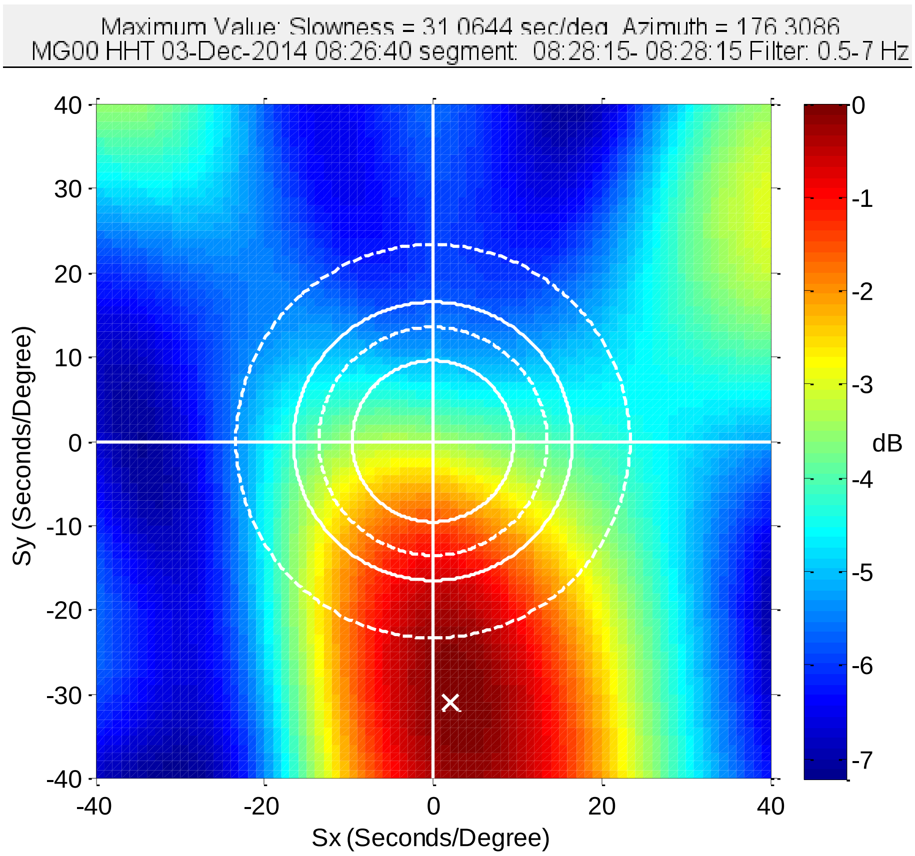

Figure 35. F-k analysis results for the 3-12-2014 earthquake (transverse component).

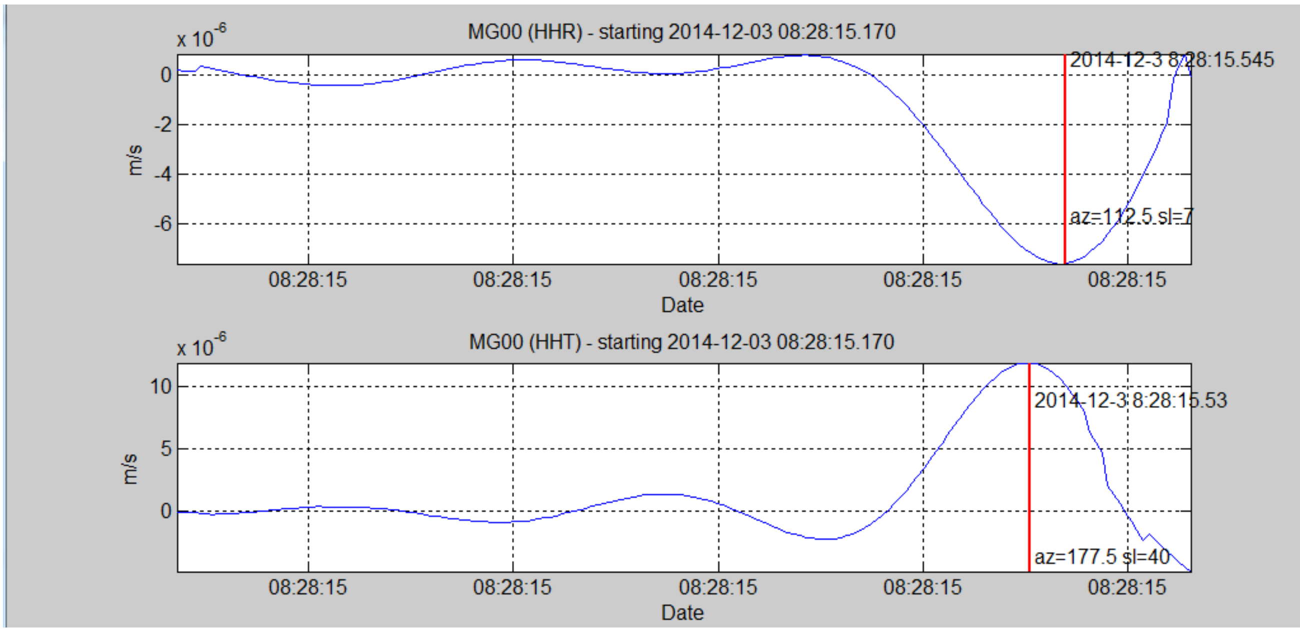

Figure 36. Point in the waveform with the highest power (radial and transverse component).

The requested parameters that resulted from the beamforming were slowness 7sec/deg and the azimuth was 112,5 for the radial component (Figure 32 & 36) and slowness 40sec/deg and the azimuth was 177,5 for the transverse component (Figure 33 & 36). The corresponding results from the f-k analysis were 26.07 sec/deg and 175,6 for the radial component (Figure 34) and 31,06 sec/deg and 176,3 for the transverse component (Figure 35).

7.1 Locating with the hybrid method

Those results are exported from the program in a *.dat file. This file is loaded afterwards in matlab and with the use of an algorithm the epicenter is located. More specifically, the events that were on the list, but were not in the corresponding event list of the National Kapodistrian University of Athens were excluded and afterwards we correlated each event to a number so as to make the procedure easier and simpler. After having applied the algorithm which is cited in APPENDIXES II &III, a file with four possible epicenters for each event is derived. To be more specific each different solution for the location corresponds to a different way of calculation. So, for the first possible solution, I used the parameters (azimuth and slowness) that resulted from the beamforming technique combining the Z- component and the radial H-component. For the second possible solution I used the parameters that resulted from the beamforming technique combining the Z- component and the transverse H-component. Correspondingly, for the third and fourth locations of the same event, I used the parameters that resulted from the f-k analysis combining either the Z- component and the radial H-component or the Z- component and the transverse H-component. All of those epicenters are depicted in the following maps (Figures 37-40).

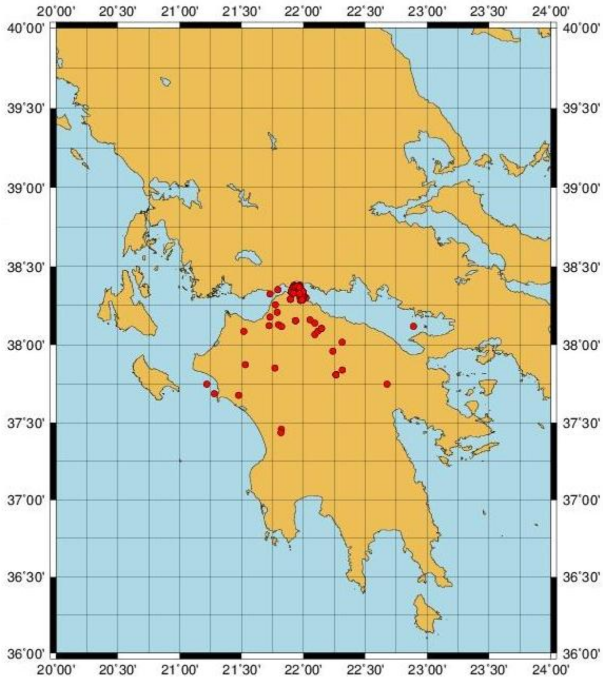

Figure 37. Epicenters based on azimuth and slowness that were derived from the application of the beamforming technique (Z-component and radial H-component).

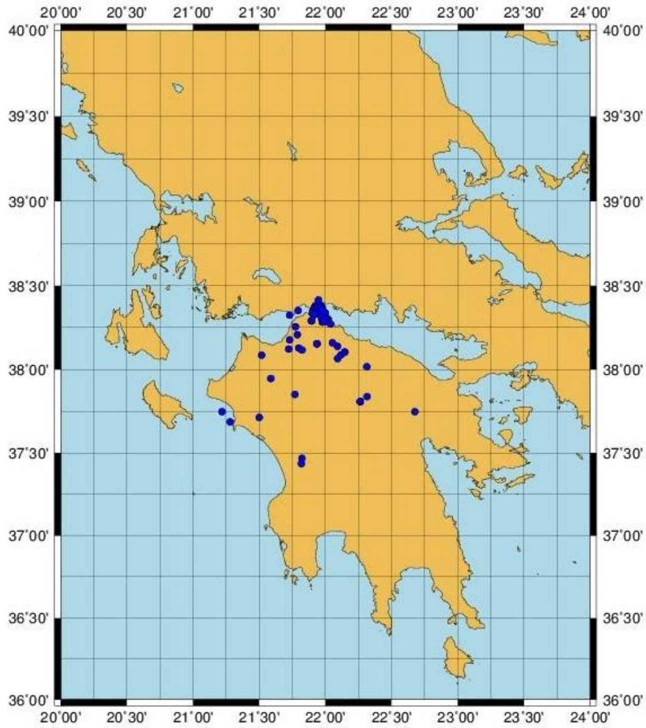

Figure 38. Epicenters based on azimuth and slowness that were derived from the application of the beamforming technique (Z-component and transverse H-component).

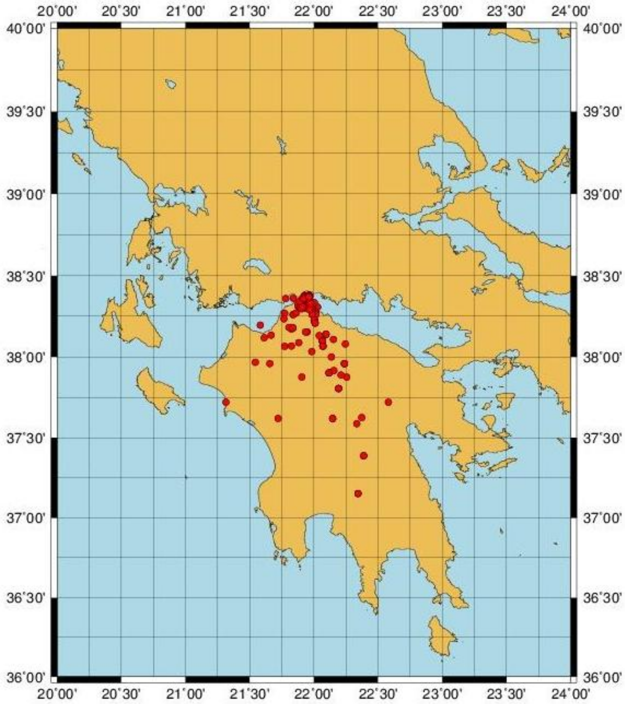

Figure 39. Epicenters based on azimuth and slowness that were derived from the application of the f-k analysis (Z-component and radial H-component).

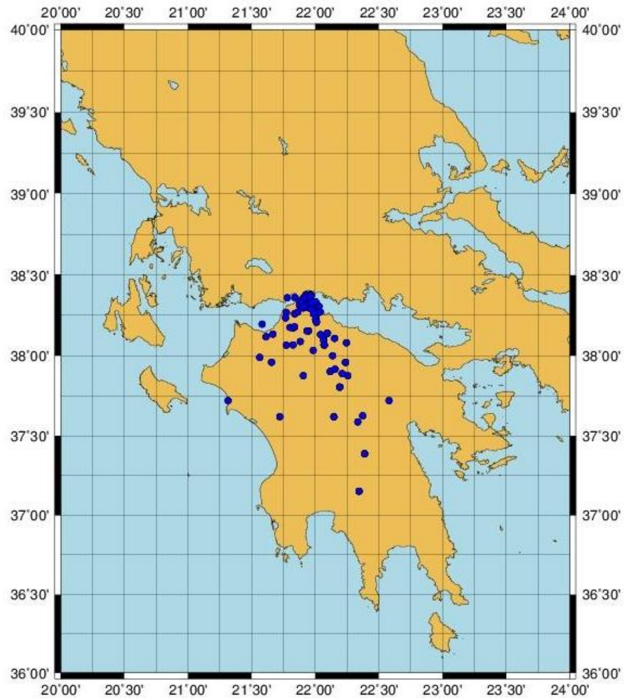

Figure 40. Epicenters based on azimuth and slowness that were derived from the application of the f-k analysis (Z-component and transverse H-component).

The following map is a synthetic one, including all four solutions for every earthquake (Figure 41).

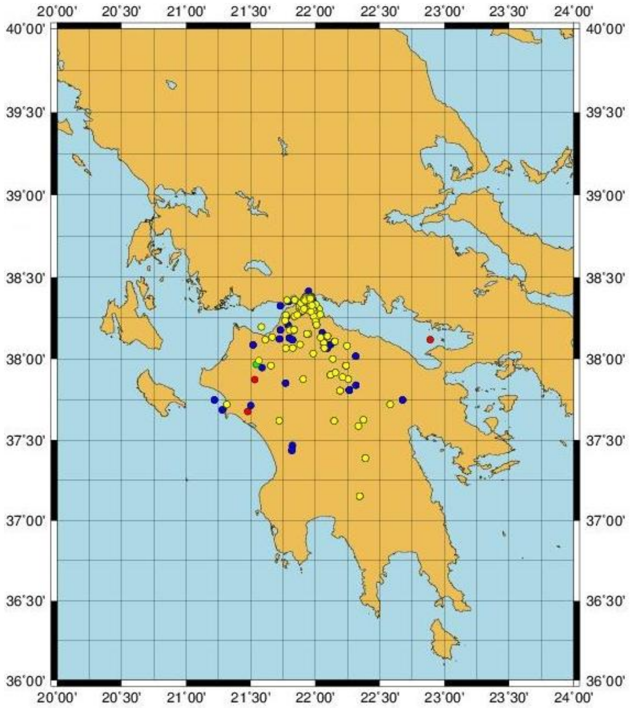

Figure 41. Epicenters based on azimuth and slowness that were derived from all the above mentioned techniques. Red: Beamforming technique using Z-component and radial H-component, Blue: Beamforming using Z-component and transverse H-component, Green: F-k analysis technique using Z-component and radial H-component and Yellow: F-k analysis using Z-component and transverse H-component.

Based on those results it can be easily concluded that there are no significant differences depending on which horizontal component will be used. Both of the results that correspond to each technique show several similarities in the locations. Yet, there are great differences between the epicenters that result from beamforming and those that result from f-k analysis.

The following maps are synthetic ones depicting all of the above results as well as the corresponding epicenters as they were calculated by the seismology lab of the National and Kapodistrian University of Athens so as to conclude on the differences between the already calculated epicenters and those calculated with the aforementioned methodology.

Based on those maps it can be easily seen that the epicenters calculated with the beamforming technique are more scattered compared to those of the HUSN. That scatter is even greater when the results are calculated with the f-k analysis. Most of those scattered earthquakes are located south of the Corinth Gulf, while some events that, based on HUSN, are located north of the Gulf have a different epicenter with the technique described above.

There are also many significant differences concerning the epicenters in the Gulf itself as the epicenters calculated with the beamforming and the f-k analysis seem to be more concentrated in the central part of the Gulf. Yet the same events based on HUSN are more scattered at the eastern and western part of the Gulf. This difference is equally existent both for the calculations with the radial and the transverse component for each technique.

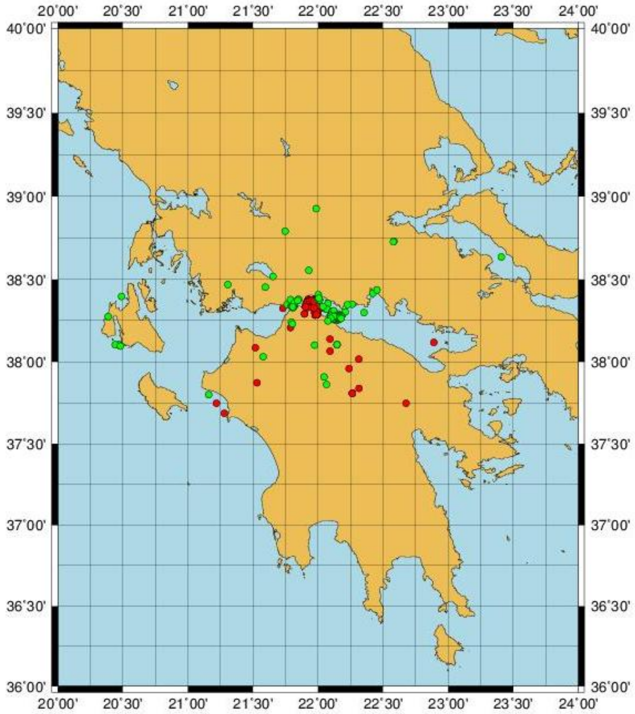

Figure 42. Epicenters based on azimuth and slowness that were derived from the application of the beamforming technique (Z-component and radial H-component) (red) and the corresponding epicenters from HUSN (green).

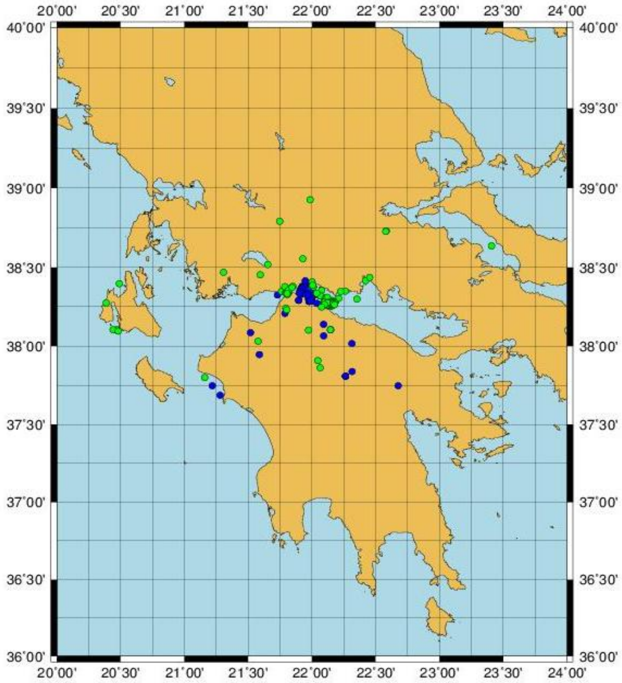

Figure 43. Epicenters based on azimuth and slowness that were derived from the application of the beamforming technique (Z-component and transverse H-component) (blue) and the corresponding epicenters from HUSN (green).

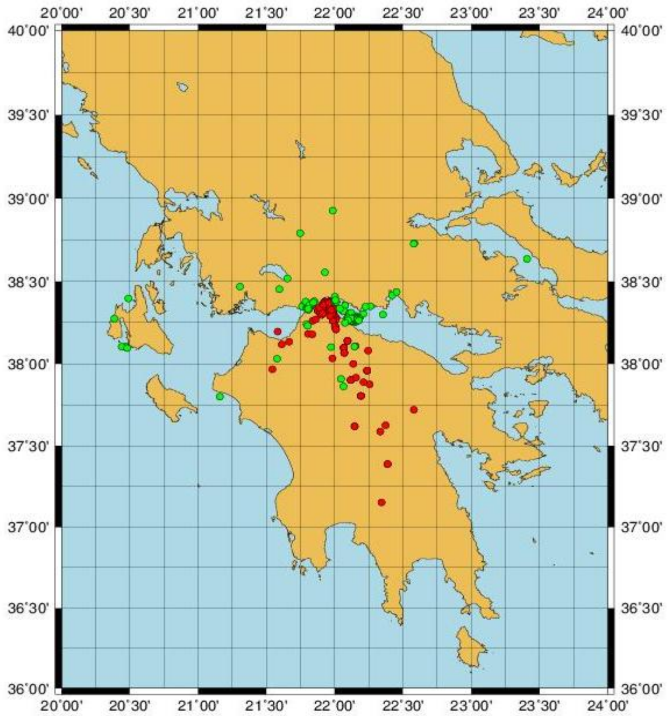

Figure 44. Epicenters based on azimuth and slowness that were derived from the application of the f-k analysis (Z-component and radial H-component) (red) and the corresponding epicenters from HUSN (green).

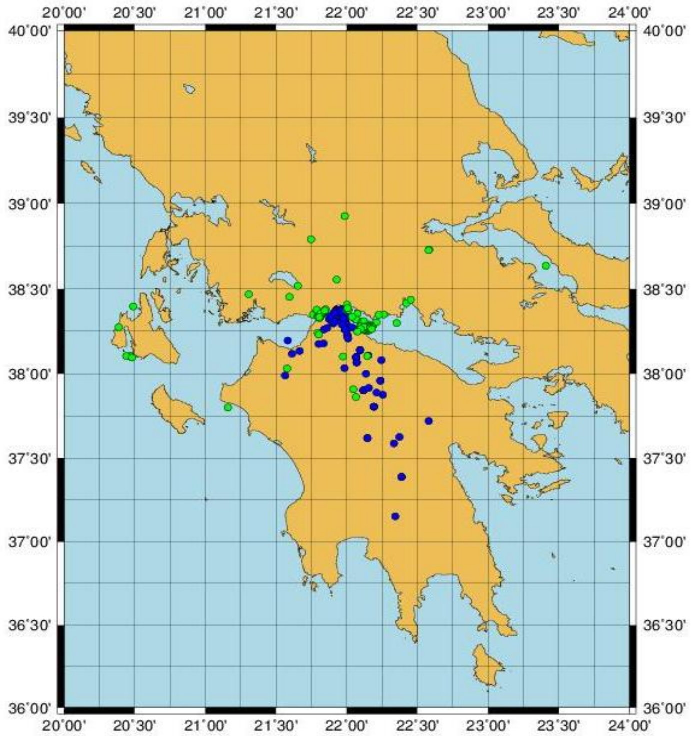

Figure 45. Epicenters based on azimuth and slowness that were derived from the application of the f-k analysis (Z-component and transverse H-component) (blue) and the corresponding epicenters from HUSN (green).

The differences that are clearly depicted on the above maps, as far as the beamforming technique is concerned, are mainly the result of the velocity model that was used throughout his study. A slight difference in the velocity of the geological structures that the propagation takes place is really important for the slowness factor that is used and can shift the location of the epicenter critically.

Another reason for the existence of those differences is the quality of the recorded signal as well as its coherency and similarity among all stations of the array. Last but not least, we should also take into account the distortion of the signal that was the result of the filters application so as to acquire the first onsets and calculate the parameters used.

As far as the f-k analysis is concerned, the main reason why there are such differences compared to the HUSN results is that the whole procedure is based on the assumption that there are no heterogeneities beneath the recorders. Most of the times, as in this situation as well, this is almost inevitable and changes the solutions of the events. This issue along with the fact that filters were applied on the signal can explain the reason why such deviations exist.

7.2 Locating with HYPOSAT

In order to increase the accuracy of the results, I also used another technique to locate the same events. In Hyposat the epicenters are not only based on the parameters of azimuth and slowness that are derived from the stations of the array, but they also depend on data from the HUSN network. More specifically for every event, I used the slowness and azimuth both from beamforming and f-k analysis (separately) as well as the first P arrival and azimuth for the three closest to the theoretical epicenter stations of the HUSN network. Each of the used for the calculations parameters (P-onset, azimuth and slowness) comes with an error factor (weight) based on its confidentiality.

After calculating those four different solutions for 25% of the total amount of earthquakes, it was rather obvious that statistically the errors of the final solution were significantly greater for the solutions that were based on the beamforming technique for both components. So the procedure was continued only for the solutions from the f-k analysis, where the errors were very low, within the tolerance limit, more accurate and more similar to the manual locations of the Kapodistrian University.

The following maps depict the epicenters as they were calculated from this procedure for 139 earthquakes. Each different solution for the location corresponds to a different way of calculation. The locations resulted from the f-k analysis combining either the Z-component and the radial H-component or the Z-component and the transverse H-component.

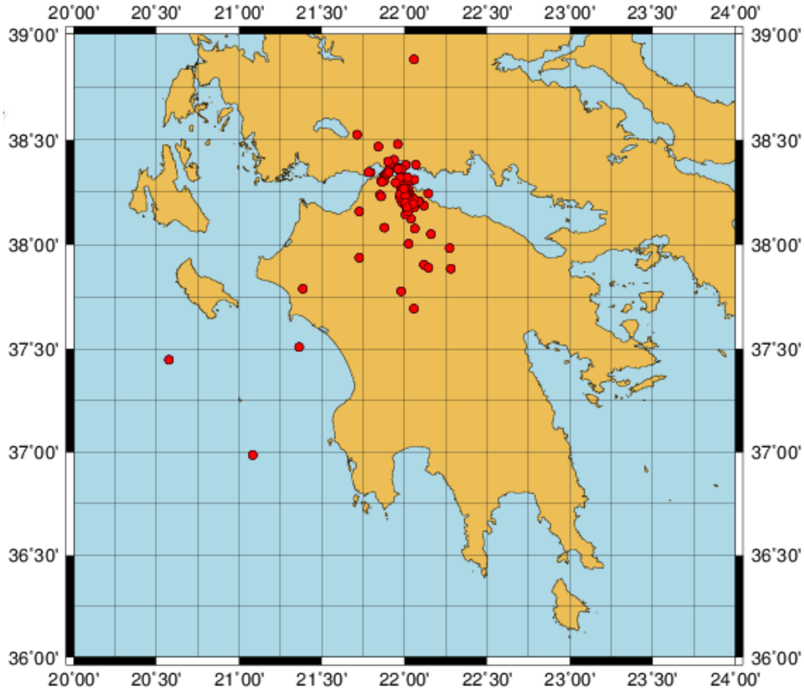

Figure 46. Epicenters calculated with HYPOSAT using the Z-component and radial H-component from the f-k analysis.

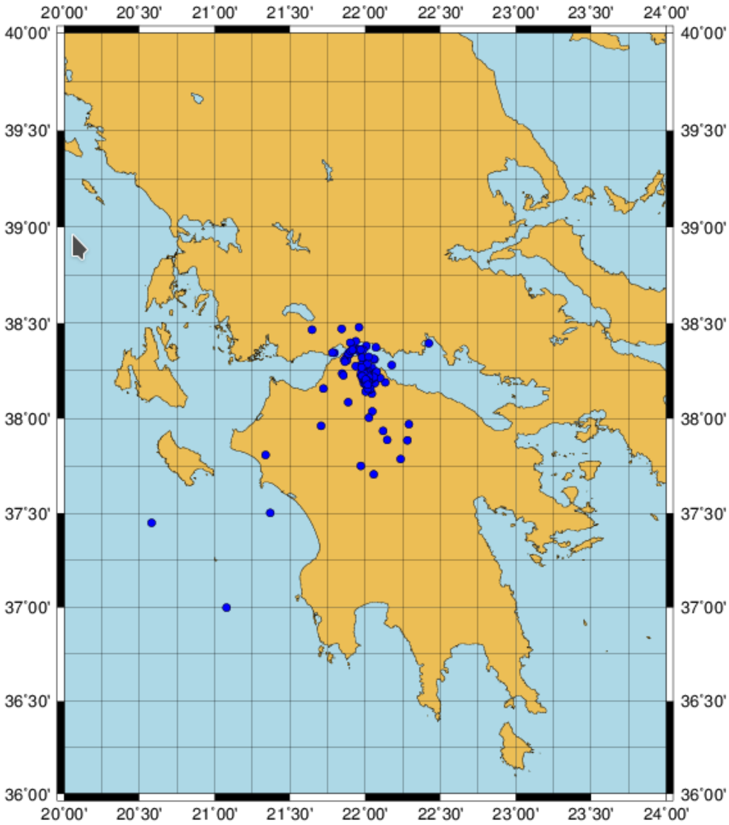

Figure 47. Epicenters calculated with HYPOSAT using the Z-component and transverse H-component from the f-k analysis.

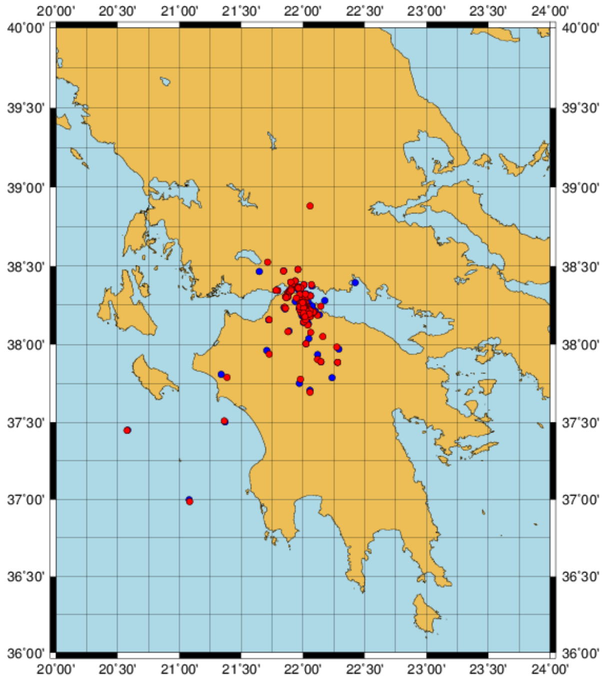

Figure 48. Epicenters calculated with HYPOSAT using the Z-component and transverse H-component from the f-k analysis (blue) and the radial H-component (red).

There are no great differences in the solutions either we use the radial or the transverse H-component based on Figure 48. Yet, we should also examine the deviations of those events when compared to the results of HUSN as they were calculated manual by the Seismology lab of the Kapodistrian University of Athens. The manual results are those preferred in this study so as to minimize the errors from the automatic locations.

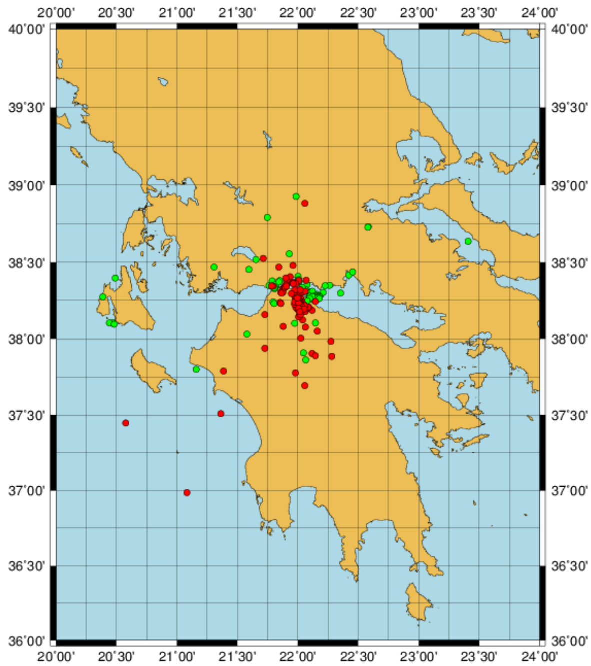

Figure 49. Epicenters calculated with HYPOSAT using the Z-component and radial H-component (red) and the corresponding epicenters from HUSN (green).

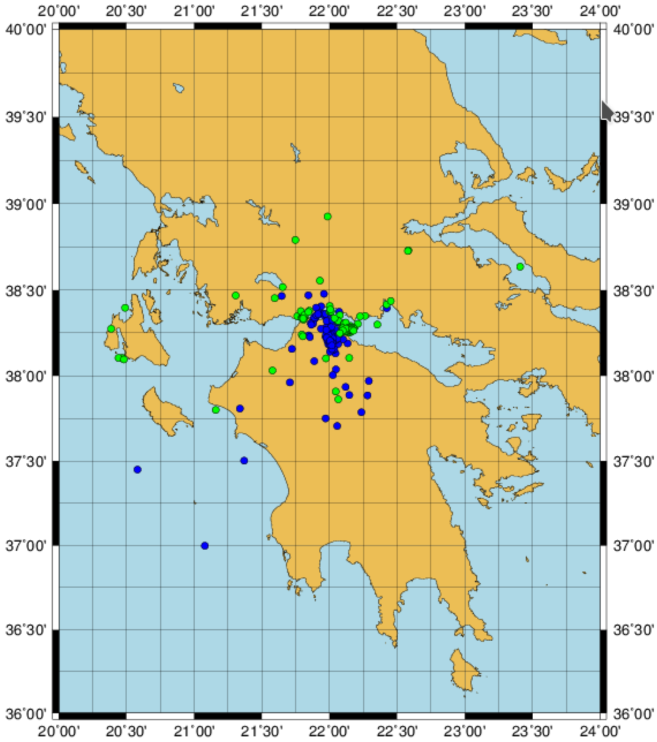

Figure 50. Epicenters calculated with HYPOSAT using the Z-component and transverse H-component (blue) and the corresponding epicenters from HUSN (green).

As with the hybrid method, hyposat also provides solutions that seem to be more scattered related to those that are calculated by the seismology lab of the National and Kapodistrian University of Athens. The difference lies on the issue that when using the radial H-component with HYPOSAT, we are able to locate some of the events at the north of the Corinth Gulf more accurately than before. The use of the radial H-component also simulates the events in the Corinth Gulf in a better way than with the use of the transverse H-component. The scattered events at the south of the Gulf are approximately the same with both components and equally different to those calculated by the National and Kapodistrian University of Athens.

The differences are also evident in those solutions and they are mostly attributed to restrictions and deviations that resulted from the application of the beamforming and f-k analysis techniques. Yet, the locations are better using the HYPOSAT compared to those of just applying the hybrid method due to the fact that HYPOSAT takes also into account phases from the HUSN network, eliminating the errors and the deviations comparing to the actual locations.

9. Conclusions

Having tried three different ways of analysis in order to acquire the location of those earthquakes it can be concluded that the technique with the most accurate and similar events to those that were calculated by the National and Kapodistrian University of Athens is the f-k analysis, using the radial H-component along with phases from the three closest to the epicenter stations of HUSN, applying the HYPOSAT algorithm.

That technique provides good locations for events in the westernmost region of the gulf as well as for a couple of events north of the Gulf. Events towards the central part of the Gulf as well as those that lie south of the gulf and in the Ionian Sea seem to have less accurate locations when using parameters from the array.

From a geological point of view, since the determination of focal mechanisms for those events exceeds the initial target of the study we cannot draw safe conclusion on the geological settings that are responsible for the events. Based only on suppositions from thoroughly examining the tectonic maps, one could say that events produced by the Psathopyrgos onshore normal fault, the Nafpaktos offshore fault system and the Trizonia fault zone can be located using the current local seismic array of Magoula – Nafpaktos. When it comes to eastern fault zones (comparing to the aforementioned) like the Eratini-West Channel, events whose hypocenters are located there seems to be attributed to the Trizonia fault zone when using the array.

The parameters extracted from the beamforming technique seem to provide the most evident deviations compared to the actual results mostly due to the restrictions that are mentioned above. Those deviations also exist with the f-k analysis results without the use of the other HUSN stations in the HYPOSAT algorithm.

One of the reasons why this technique seems to fail in providing us more accurate locations is the geology of the area of the seismic array. Even though its geometry was thoroughly studied before its application and there were no altitude differences in the deployment position of the stations the results were not promising due to the heterogenities and structural anomalies that govern the broader area.

Another reason why the array failed to meet its initial deployment goal was the velocity model which was used. The model that was used was a local one which was concluded after several trials. The main idea was that since the data used were extracted from the same cluster the same velocity model could be applied in all of the events. Apparently that hypothesis did not prove right based on the results due to the sensitivity of this method concerning velocities.

Except for these the quality of the signals and the distortion which were rather obvious due to the evidently great human activity that characterizes the area, is of great importance during those procedures since they can alter the solution significantly.

The overall conclusion on the issue is that despite the fact that such arrays provide us with very well located epicenters in other Greek areas, this specific area is not appropriate for such a study. This technique can only be used supplementary in cases when the location cannot be found precisely by the HUSN stations and a more local array with local velocity models needs to be used.

10. Issues for further analysis

In order to manage a better and more complete conclusion on the application of those techniques, more earthquakes should be analyzed. This would minimize the low-quality signals, giving the chance to use more accurate phases and minimize this way the errors connected to the azimuth's and slowness' calculation.

What is more, it would also be very beneficial for the study, if we established arrays like that in different locations so as to eliminate or at least examine the impact of the geological heterogeneities under the array to the final solution. The selection of the most realistic velocity model is one of the main restrictions for the application of all those techniques and needs to be further examined.

11. Appendixes

APPENDIX I

```
function epicenter = arr_locate_simple(sp,slow,baz,plt)
%   arr_locate location function. Algorithm reads all scattr samples from a
%   scater binary file, then reads a velocity model, shoots a ray for the
%   selected slowness and backazimuth and calculates S-P travel time
%   difference. The point at witch the difference between the observed and
%   calculated sp is minimized is selected as the hypocenter.
%
%
%   sp = S - P arrival time difference
%
%   slow = slowness in s/km
%
%   baz = backazimuth in degrees.
%
%   plt = 1 plots ray and optimal hypocenter. 0 supresses plot
%
%   output is a 3 element vector with: x,y,z of point with minimized sp

%%%%%%%%%%%%%%%%%%%%%%%%%%%%%%%%%%%%%%%%%%%
% Check arguments.
%
if nargin < 1
  error ( 'No input arguments given' );
  return;
elseif nargin < 4 || nargin > 4
  error ( 'Incorrect number of input arguments. (sp, slowness, backazimuth, plotflag)' );
  return;
elseif plt<0 || plt>1
  error ( 'plot argument must be 0 or 1' );
  return;
end

%%%%%%%%%%%%%%%%%%%%%%%%%%%%%%%%%%%%%%%%%%%
% Load the velocity model
%
modfile='model.dat';
fid=fopen(modfile);
if fid<0
    error ( 'Could not open model file' );
    return;
end
clear values
values=textscan(fid,'%f','Delimiter',' ','MultipleDelimsAsOne',1);  % velocity model is loaded into a single 1d vector
fclose all;

k=1;
for i =1:2:length(values{1,1})-1    % Loop to create depth and velocity vectors
    d(k)=values{1,1}(i);
    Vp(k)=values{1,1}(i+1);
    k=k+1;
end

clear k values fid modfile i

% Same for S
modfile='models.dat';
fid=fopen(modfile);
if fid<0
    error ( 'Could not open model file' );
    return;
end
clear values
values=textscan(fid,'%f','Delimiter',' ','MultipleDelimsAsOne',1);  % velocity model is loaded into a single 1d vector
fclose all;
```

```
k=1;
for i =1:2:length(values{1,1})-1     % Loop to create depth and velocity vectors
    Vs(k)=values{1,1}(i+1);
    k=k+1;
end

if abs(length(Vp)-length(Vs))>0
    error ( 'Vp and Vs layer number bot equal' );
    return;
end
%%%%%%%%%%%%%%%%%%%%%%%%%%%%%%%%%%%%%%%%%%%
% Ray tracing part
clear velp an1 d2 d3 xn ttimep p_ray  Vp_orig z df J slowp Vp3 dep k values fid modfile i
velp=1/slow;                    % Convert apparent slowness to apparent velocity
an1=asind(Vp(1)/velp);          % P Take-off angle at the surface
k=1;

for z=0.005:0.005:50
    d2=d;                       % Create a new vector with the initial layer depths
    d2(end+1)=z;                % Add the z depth
    d3=sort(d2);                % Sort the new depth with the addition of z
    [~,J]=find(d3==z);          % Find index (J) of z depth in the new vector
    J=J-1;
    Vp3(k)=Vp(J(end));          % Construct new velocity vector. Vp for each depth z
    Vs3(k)=Vs(J(end));          % Same for S
    dep(k)=z;                   % depth(k) for V(k)
    k=k+1;
end

% p_ray=zeros(length(dep),4);                        % Preallocate ray vector
ttimep=0;
ttimes=0;
xn=0;
for i=2:length(dep)                                  % Loop through all depths and calculate raypoints and traveltimes
    an1=asind((Vp3(i)/Vp3(i-1))*sind(an1));          % Calculate new angle at depth z(i)
    if isreal(an1)==1                                % Stop algorithm when total reflection occurs
        df=dep(i)-dep(i-1);                          % Get layer width (or layer-to-z depth width)
        dx=df*tand(an1);                             % Calculate horizontal distance inbetween depths z(i-) to z(i)
        xn=xn+dx;                                    % Calculate total horizontal distance
        ttimep=ttimep+sqrt(dx^2+df^2)/Vp3(i);        % Get P traveltime for new xn
        ttimes=ttimes+sqrt(dx^2+df^2)/Vs3(i);        % Get S traveltime for new xn
    else
        disp(['Total reflection ad depth = ' num2str(dep(i))])
        break
    end
    p_ray(i,:)=[sind(baz)*xn, cosd(baz)*xn, dep(i), ttimes-ttimep];   % Populate the ray point vector

end

%%%%%%%%%%%%%%%%%%%%%%%%%%%%%%%%%%%%%%%%%%%
% Find ray point where the observed and calculated sp difference is
% minimized
minsp=99999999;
for i=1:length(p_ray(:,1))
    if abs(p_ray(i,4)-sp)<minsp
        minsp=abs(p_ray(i,4)-sp);
        epicenter=[p_ray(i,1) p_ray(i,2) p_ray(i,3)];
    end
end
```

```
%%%%%%%%%%%%%%%%%%%%%%%%%%%%%%%%%%%%%%%%%%%%
% Plot here
if plt==0
    return
end
figure
subplot(2,2,1)
hold on
plot(p_ray(:,1),p_ray(:,2),'linewidth',2);
plot(epicenter(1), epicenter(2),'or','markersize',10,'linewidth',2);
plot(0,0,'^g','markersize',10,'linewidth',2);
xlabel('X (km)','Fontsize',15,'fontweight','bold')
ylabel('Y (km)','Fontsize',15,'fontweight','bold')
axis equal
subplot(2,2,2)
plot(p_ray(:,1),-p_ray(:,3),'linewidth',2);
hold on
plot(epicenter(1), -epicenter(3),'or','markersize',10,'linewidth',2);
xlabel('X (km)','Fontsize',15,'fontweight','bold')
ylabel('Z (km)','Fontsize',15,'fontweight','bold')
axis equal
subplot(2,2,3)
plot(p_ray(:,2),-p_ray(:,3),'linewidth',2);
hold on
plot(epicenter(2), -epicenter(3),'or','markersize',10,'linewidth',2);
xlabel('X (km)','Fontsize',15,'fontweight','bold')
ylabel('Z (km)','Fontsize',15,'fontweight','bold')
axis equal
legend([{'ray'};{'minsp'}])
```

APPENDIX II

```
k=0;
for i=1:6:1622;
    k=k+1;
    sp_tmp = PICK(i+2,1)-PICK(i,1);
    sp_dv = datevec(sp_tmp);
    sp(k,1) = sp_dv(6);
    sp(k,9) = PICK(i+2,1)-PICK(i,1);
    sp_tmp = PICK(i+4,1)-PICK(i,1);
    sp_dv = datevec(sp_tmp);
    sp(k,2) = sp_dv(6);
    sp(k,10) = PICK(i+4,1)-PICK(i,1);
    sp_tmp = PICK(i+3,1)-PICK(i+1,1);
    sp_dv = datevec(sp_tmp);
    sp(k,3) = sp_dv(6);
    sp(k,11) = PICK(i+3,1)-PICK(i+1,1);
    sp_tmp = PICK(i+5,1)-PICK(i+1,1);
    sp_dv = datevec(sp_tmp);
    sp(k,4) = sp_dv(6);
    sp(k,12) = PICK(i+5,1)-PICK(i+1,1);
    sp(k,5) = AZIM(i,1);
    sp(k,6) = AZIM(i+1,1);
    sp(k,7) = SLOW(i,1);
    sp(k,8) = SLOW(i+1,1);
end
for k=1:271;
    loc(k,1:3)=arr_locate_simple(sp(k,1),sp(k,7)/110.1,sp(k,5),0);
    loc(k,4:6)=arr_locate_simple(sp(k,2),sp(k,7)/110.1,sp(k,5),0);
    loc(k,7:9)=arr_locate_simple(sp(k,3),sp(k,8)/110.1,sp(k,6),0);
    loc(k,10:12)=arr_locate_simple(sp(k,4),sp(k,8)/110.1,sp(k,6),0);
end
for k=1:190;
    deg (k,1)= km2deg(loc(k,1));
    deg (k,2)= km2deg(loc(k,2));
    deg (k,3)=loc(k,3);
    deg (k,4)= km2deg(loc(k,4));
    deg (k,5)= km2deg(loc(k,5));
    deg (k,6)=loc(k,6);

    deg (k,7)= km2deg(loc(k,7));
    deg (k,8)= km2deg(loc(k,8));
    deg (k,9)=loc(k,9);
    deg (k,10)= km2deg(loc(k,10));
    deg (k,11)= km2deg(loc(k,11));
    deg (k,12)=loc(k,12);
end

k=0;
for i=1:6:1622;
    k=k+1;
    info(k,1)=YEAR(i,1);
    info(k,2)=MONTH(i,1);
    info(k,3)=DAY(i,1);
    info(k,4)=HOUR(i,1);
    info(k,5)=MIN(i,1);
    info(k,6)=SEC(i,1);
end
```

```
for k=1:190;
    lon=21.947;
    lat=38.415;
    epic (k,1)= info(k,1);
    epic (k,2)= info(k,2);
    epic (k,3)= info(k,3);
    epic (k,4)= info(k,4);
    epic (k,5)= info(k,5);
    epic (k,6)= info(k,6);
    epic (k,7)= deg (k,1)+lon;
    epic (k,10)= deg (k,4)+lon;
    epic (k,13)= deg (k,7)+lon;
    epic (k,16)= deg (k,10)+lon;
    epic (k,8)= deg (k,2)+lat;
    epic (k,11)= deg (k,5)+lat;
    epic (k,14)= deg (k,8)+lat;
    epic (k,17)= deg (k,11)+lat;
    epic (k,9)= deg (k,3);
    epic (k,12)= deg (k,6);
    epic (k,15)= deg (k,9);
    epic (k,18)= deg (k,12);
    end
filename = 'epic.xlsx';
xlswrite(filename,epic)
```

APPENDIX III

```matlab
clear all
close all
global det_type
global pick
global plot_beam
global flton
global shape
global saveseg
global evmethod
global azstep
global slstep
global ph_fid
global fk_comp
global fkslmin
global fkslmax
global fkbandmin
global fkbandmax


% Initial parameters

% Main startup switch parameters

det_type = 0; % Detection type 0 for P waves and Z component 1 for S waves
              % and rotation of H components
pick = 1; % should be set to 1 for segment selection
plot_beam = 1; % Set this switch to 1 to plot the final beam or beams on a
               % separate plot. Set to 0 to disable.
flton = 1; % set to 1 to filter signals beforebeam forming
shape = [0.5 18.]; % Filter cut off frequencies to be used if needed
saveseg = 0; % should be 1 to save the selected segment
orig_plot = 1; % should be set to 1 to plot the original selected segment
evmethod = 2; % Defines method to be used in order to evaluate maximum beam
              % value and select the solution.
              % 0 = Maximum beam value normalized by the mean of the maximum
              %     values
              % 1 = Maximum beam value not normalized

              % 2 = Maximum beam envelope (power) value is used
              % Within the script all 3 methods are calculated and the
              % selected one is used for plotting
azstep = 5; % Azimuth step
slstep = 1; % Slowness step
fk_comp = 1; % Perform also FK computations
fkslmin = -40; % Minimum slowness value for FK computations
fkslmax = 40; % Maximum slowness value for FK computations
fkbandmin = 0.0; % Minimum frequency value for FK computations (% srate)
fkbandmax = 0.3; % Maximum frequency value for FK computations (% srate)

% ---------------------------------------------------------------------------
% Open file for beam generated phases

ph_fid=fopen('beamphases.dat','a+');


% ---------------------------------------------------------------------------
```

```
% Create GUI figure

guif = figure(...
        'Name', 'Beam Power and FK analysis',...
        'Visible', 'off', ...
        'Position', [400 200 480 280], ...
        'NumberTitle', 'off',...
        'Resize', 'off',...
        'ToolBar', 'none', ...
        'MenuBar', 'none' ...
        );
% -------------------------------------------------------------------------

% Construct radiobuttons for the components

butgrp = uibuttongroup('Position', [0.03 0.02 0.3 0.25], 'Visible', 'on');

zcomp = uicontrol('Style', 'radiobutton', 'String', 'Z-Component', ...
    'Position', [20 30 110 30], 'Parent', butgrp,'FontSize',12, ...
    'HandleVisibility', 'off');
hcomp = uicontrol('Style', 'radiobutton', 'String', 'H-Component', ...
    'Position', [20 5 110 30], 'Parent', butgrp, 'FontSize',12, ...
    'HandleVisibility', 'off');
set(butgrp,'SelectionChangeFcn',@butgrp_selcbk);
set(butgrp,'SelectedObject',zcomp);
set(butgrp, 'Visible', 'on');


% -------------------------------------------------------------------------

% Construct pushbutton to initiate calculations

proces = uicontrol('Style', 'pushbutton', 'String', 'Process', ...
            'Position', [210 4 70 30], ...
            'Callback', @beamform_init);

% -------------------------------------------------------------------------
% Construct general options panel

gopanel = uipanel('Title','General Options','FontSize',12,...
            'TitlePosition', 'centertop', ...
            'BackgroundColor',[0.95 0.95 0.95],'Position',[0.03 .29 .3 .70]);

% -------------------------------------------------------------------------

% Construct FK Analysis checkbox

fktxt = uicontrol('Parent',gopanel,'Style', 'text', 'FontSize',12,...
            'String', 'FK Calculations', 'HorizontalAlignment', 'Right', ...
            'BackgroundColor', [0.95 0.95 0.95], 'Position', [0 155 90 15]);
fkcal = uicontrol('Parent',gopanel,'Style', 'checkbox', 'Value', 1, ...
            'Position', [105 155 20 20], ...
            'BackgroundColor', [0.95 0.95 0.95], ...
            'Callback','fk_comp = get(fkcal,''Value'');');
align([fktxt, fkcal], 'None', 'Middle');

% -------------------------------------------------------------------------
```

```matlab
% Construct select segment checkbox

picktxt = uicontrol('Parent',gopanel,'Style', 'text', 'FontSize',12,...
            'String', 'Select segment', 'HorizontalAlignment', 'Right', ...
            'BackgroundColor', [0.95 0.95 0.95], 'Position', [0 130 90 15]);
pickseg = uicontrol('Parent',gopanel,'Style', 'checkbox', 'Value', 1, ...
            'Position', [105 130 20 20], ...
            'BackgroundColor', [0.95 0.95 0.95], ...
            'Callback','pick = get(pickseg,''Value'');');
align([picktxt, pickseg], 'None', 'Middle');

% ---------------------------------------------------------------------------

% Construct save segment checkbox

savestxt = uicontrol('Parent',gopanel,'Style', 'text', 'FontSize',12,...
            'String', 'Save segment', 'HorizontalAlignment', 'Right', ...
            'BackgroundColor', [0.95 0.95 0.95], 'Position', [0 105 90 15]);
savsg = uicontrol('Parent',gopanel,'Style', 'checkbox', 'Value', 0, ...
            'Position', [105 105 20 20], ...
            'BackgroundColor', [0.95 0.95 0.95], ...
            'Callback','saveseg = get(savsg,''Value'');');
align([savestxt, savsg], 'None', 'Middle');

% ---------------------------------------------------------------------------

% Construct plot beam checkbox

pltbmtxt = uicontrol('Parent',gopanel,'Style', 'text','FontSize',12,...
            'String', 'Plot beam', 'HorizontalAlignment', 'Right', ...
            'BackgroundColor', [0.95 0.95 0.95], 'Position', [0 80 90 15]);
pltbm = uicontrol('Parent',gopanel,'Style', 'checkbox', 'Value', 1, ...
            'Position', [105 80 20 20], ...
            'BackgroundColor', [0.95 0.95 0.95], ...
            'Callback','plot_beam = get(pltbm,''Value''); display(plot_beam);');

align([pltbmtxt, pltbm], 'None', 'Middle');

% ---------------------------------------------------------------------------

% Construct filter data checkbox

flttxt = uicontrol('Parent',gopanel,'Style', 'text', 'FontSize',12,...
            'String', 'Filter data', 'HorizontalAlignment', 'Right', ...
            'BackgroundColor', [0.95 0.95 0.95], 'Position', [0 55 90 15]);
filt = uicontrol('Parent',gopanel,'Style', 'checkbox', 'Value', 1, ...
            'Position', [105 55 20 20], ...
            'BackgroundColor', [0.95 0.95 0.95], ...
            'Callback','[flton] = getflt_status(filt);');
align([flttxt, filt], 'None', 'Middle');

% ---------------------------------------------------------------------------

% Construct low cut filter frequency textbox

lctxt = uicontrol('Parent',gopanel,'Style', 'text',  'FontSize',12,...
            'String', 'Low cut (Hz)', 'HorizontalAlignment', 'Right', ...
            'BackgroundColor', [0.95 0.95 0.95], 'Position', [0 30 90 15]);
lcflt = uicontrol('Parent',gopanel,'Style', 'edit',  'FontSize',12,...
            'String', num2str(shape(1,1)), ...
            'Position', [95 30 40 20], ...
            'BackgroundColor', [1 1 1], ...
            'Callback','shape(1,1) = str2num(get(lcflt,''String''));');
align([lctxt, lcflt], 'None', 'Middle');

% ---------------------------------------------------------------------------
```

```matlab
% Construct high cut filter frequency textbox

hctxt = uicontrol('Parent',gopanel,'Style', 'text',  'FontSize',12,...
            'String', 'High cut (Hz)', 'HorizontalAlignment', 'Right', ...
            'BackgroundColor', [0.95 0.95 0.95], 'Position', [0 5 90 15]);
hcflt = uicontrol('Parent',gopanel,'Style', 'edit',  'FontSize',12,...
            'String', num2str(shape(1,2)), ...
            'Position', [95 5 40 20], ...
            'BackgroundColor', [1 1 1], ...
            'Callback','shape(1,2) = str2num(get(hcflt,''String''));');
align([hctxt, hcflt,], 'None', 'Middle');


% ----------------------------------------------------------------------------

% Construct beamforming options panel

bfopanel = uipanel('Title','Beamforming Options','FontSize',12,...
             'TitlePosition', 'centertop', ...
             'BackgroundColor',[0.95 0.95 0.95],'Position',[0.35 .55 .3 .45]);


% ----------------------------------------------------------------------------

% Construct azimuth step textbox

aztxt = uicontrol('Parent',bfopanel,'Style', 'text', 'FontSize',12,...
            'String', 'Azimuth step', 'HorizontalAlignment', 'Right', ...
            'BackgroundColor', [0.95 0.95 0.95], 'Position', [0 85 90 15]);
azst = uicontrol('Parent',bfopanel,'Style', 'edit', 'FontSize',12,...
            'String', num2str(azstep), ...
            'Position', [95 85 40 20], ...
            'BackgroundColor', [1 1 1], ...
            'Callback','azstep = str2num(get(azst,''String''));');

align([aztxt, azst], 'None', 'Middle');

% ----------------------------------------------------------------------------

% Construct slowness step textbox

sltxt = uicontrol('Parent',bfopanel,'Style', 'text', 'FontSize',12,...
            'String', 'Slowness step', 'HorizontalAlignment', 'Right', ...
            'BackgroundColor', [0.95 0.95 0.95], 'Position', [0 60 90 15]);
slst = uicontrol('Parent',bfopanel,'Style', 'edit', 'FontSize',12,...
            'String', num2str(slstep), ...
            'Position', [95 60 40 20], ...
            'BackgroundColor', [1 1 1], ...
            'Callback','slstep = str2num(get(slst,''String''));');
align([sltxt, slst], 'None', 'Middle');

% ----------------------------------------------------------------------------

% Construct pulldown menue to select beam power calculation options

evmth = uicontrol('Parent',bfopanel,'Style', 'popupmenu','FontSize',12, ...
            'String', {'Max Power', 'Maximum', 'Max Norm'}, ...
            'Position', [10 3 120 30], ...
            'Callback','[evmethod] = evmethod_popup(evmth);');
evtxt = uicontrol('Parent',bfopanel,'Style', 'text', 'FontSize',12,...
            'String', 'Select method', ...
            'BackgroundColor', [0.95 0.95 0.95], 'Position', [0 40 140 15]);
align([evmth, evtxt], 'Center', 'None');

% ----------------------------------------------------------------------------
```

```
% Construct FK options panel

fkopanel = uipanel('Title','FK Options','FontSize',12,...
            'TitlePosition', 'centertop', ...
            'BackgroundColor',[0.95 0.95 0.95],'Position',[0.35 .12 .3 .42]);

% -------------------------------------------------------------------------

% Construct fk slowness min textbox

fkslmintxt = uicontrol('Parent',fkopanel,'Style', 'text', 'FontSize',12,...
            'String', 'FK slow min', 'HorizontalAlignment', 'Right', ...
            'BackgroundColor', [0.95 0.95 0.95], 'Position', [0 80 90 15]);
fksmin = uicontrol('Parent',fkopanel,'Style', 'edit', 'FontSize',12,...
            'String', num2str(fkslmin), ...
            'Position', [95 80 40 20], ...
            'BackgroundColor', [1 1 1], ...
            'Callback','fkslmin = str2num(get(fksmin,''String''));');
align([sltxt, slst], 'None', 'Middle');

% -------------------------------------------------------------------------

% Construct fk slowness max textbox

fkslmaxtxt = uicontrol('Parent',fkopanel,'Style', 'text', 'FontSize',12,...
            'String', 'FK slow max', 'HorizontalAlignment', 'Right', ...
            'BackgroundColor', [0.95 0.95 0.95], 'Position', [0 55 90 15]);
fksmax = uicontrol('Parent',fkopanel,'Style', 'edit', 'FontSize',12,...
            'String', num2str(fkslmax), ...
            'Position', [95 55 40 20], ...
            'BackgroundColor', [1 1 1], ...
            'Callback','fkslmax = str2num(get(fksmax,''String''));');
align([sltxt, slst], 'None', 'Middle');

% -------------------------------------------------------------------------

% Construct fk band min textbox

fkbmintxt = uicontrol('Parent',fkopanel,'Style', 'text', 'FontSize',12,...
            'String', 'FK band min', 'HorizontalAlignment', 'Right', ...
            'BackgroundColor', [0.95 0.95 0.95], 'Position', [0 30 90 15]);
fkbmin = uicontrol('Parent',fkopanel,'Style', 'edit', 'FontSize',12,...
            'String', num2str(fkbandmin), ...
            'Position', [95 30 40 20], ...
            'BackgroundColor', [1 1 1], ...
            'Callback','fkbandmin = str2num(get(fkbmin,''String''));');
align([sltxt, slst], 'None', 'Middle');

% -------------------------------------------------------------------------

% Construct fk band max textbox

fkbmaxtxt = uicontrol('Parent',fkopanel,'Style', 'text', 'FontSize',12,...
            'String', 'FK band max', 'HorizontalAlignment', 'Right', ...
            'BackgroundColor', [0.95 0.95 0.95], 'Position', [0 5 90 15]);
fkbmax = uicontrol('Parent',fkopanel,'Style', 'edit', 'FontSize',12,...
            'String', num2str(fkbandmax), ...
            'Position', [95 5 40 20], ...
            'BackgroundColor', [1 1 1], ...
            'Callback','fkbandmax = str2num(get(fkbmax,''String''));');
align([sltxt, slst], 'None', 'Middle');



% -------------------------------------------------------------------------
% Make GUI visible

set(guif, 'Visible', 'on');
```

APPENDIX IV

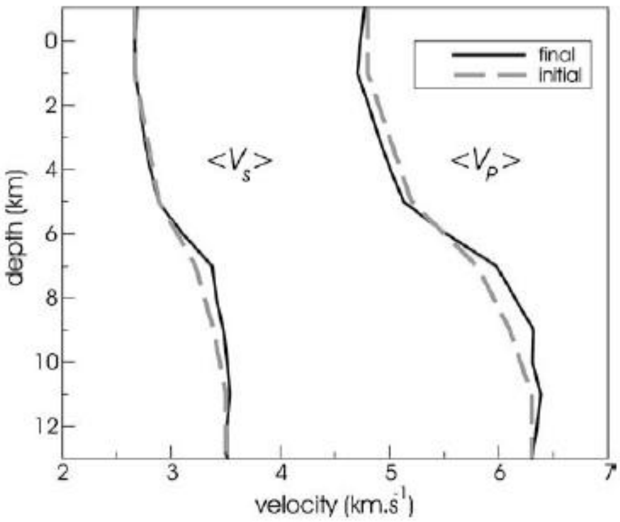

The figure above suggests a velocity model about the Corinth Gulf as it was calculated by Gautier et al., 2006. Those are mean velocity profiles for the S and P waves (left and right respectively). The initial model that was used in that study was the one that was proposed by Rigo et al., 1996. That was a rather local velocity model about the western part of the gulf which was also taken into account in this study in order to conclude after several trials on the used model. The Rigo et al., 1996 model is listed beneath in detail.

	Model 1	***Model 2***
Depth (km)	**Vp(km/s)**	**Vp(km/s)**
0.0-4.0	5.6	4.8
4.0-7.2		5.2
7.2-8.2		5.8
8.2-10.4		6.1
10.4-15.0		6.3
15.0-30.0	6.5	6.5
>30.0	7.0	7.0

10. Bibliography

Alomax.free.fr. (2017). The NonLinLoc Software Guide. [online] Available at: http://alomax.free.fr/nlloc/ [Accessed 9 Sep. 2017].

Beckers, A., Hubert-Ferrari, A., Beck, Ch., Bodeux, S., Tripsanas, E., Sakellariou, D. and De Batist, M., 2015. Active faulting at the western tip of the Gulf of Corinth, Greece, from high-resolution seismic data. *Marine Geology*. 360 January, pp.55-69.

Bernard, P., Briole, P., Meyer, B., Lyon-Caen, H., Gomez, M., Tiberi, C., Berge, C., Cattin, R., Hatzfeld, D., Lachet, C., Lebrun, B., Deschamps, A., Courboulex, F., Larroque, C., Rigo, A., Massonnet, D., Papadimitriou, P., Kassaras, J., Diagourtas, D., Makropoulos, K., Veis, G., Papazisi, E., Mitsakaki, C., Karakostas, V., Papadimitriou, E., Papanastasiou, D., Chouliaras, M. and Stavrakakis, G. 1997. The Ms=6.2, June 15, 1995 Aigion earthquake (Greece): evidence for low angle normal faulting in the Corinth rift. *Journal of Seismology* [online] 1 May pp. 131-150. Available from: <https://www.researchgate.net/> [Accessed March 24 2018].

Bernard, P., Lyon-Caen, H., Briole, P., Deschamps, A., Boudin, F., Makropoulos, K., Papadimitriou, P., Lemeille, F., Patau, G., Billiris, H., Paradissis, D., Papazissi, K., Castarede, H., Charade, O., Nercessia, A., Avallone, A., Pacchiani, F., Zahradnnik, J., Sacks, S. and Linde, A. 2006. Seismicity deformation and seismic hazard in the western rift of Corinth: New insights from the Corinth Rift Laboratory (CRL). *Tectonophysics* [online] 426 August pp. 7-30. Available from: <http://ardoise.ens.fr/> [Accessed April 3 2015].

Bernard, P., Boudin, F., Linde, A., Sacks, S., Serpetsidaki, A., Patau, G. and Diagourtas, D. 2008. Seismic and Aseismic Processes on the Psathpyrgos Normal Fault, Western Rift of Corinth, Greece. *American Geophysical Union, Fall Meeting 2008*. Available from: <http://adsabs.harvard.edu/> [Accessed April 3 2015].

Bourouis, S. and Cornet, F.H. 2009. Microseismic activity and fluid fault interactions: some results from the Corinth Rift Laboratory (CRL), Greece. *Geophysical Journal International* [online] 178 February pp. 561-580. Available from: <https://watermark.silverchair.com/> [Accessed March 24 2018].

Chevy, J. 2001. Core complex mechanics: From the Gulf of Corinth to the Snake Range. *Geology*[online] 29(5) May, pp.439-442. Available from: <http://geology.gsapubs.org/> [Accessed November 12, 2010].

Chouliaras, G., Kassaras I., Kapetanidis, V., Petrou, P. and Drakatos, G. 2015. Seismotectonic analysis of the 2013 seismic sequence at the westernCorinth Rift. *Journal of Geodynamics* [online] 90 July pp. 42-57. Available from: <http://www.elsevier.com> [Accessed March 24 2018].

Collier, R. & Jones, G., 2003. Rift sequences of the Southern Margin of the Gulf of Corinth (Greece) as exploration/production analogues, *in AAPG International Conference, Barcelona*, Search and Discovery Article #90017.

Drouza, S., Georgoulias, F.A. and Moustakas, N.K., 2007. Investigation of soils on volcanic materials in Nisyros Island, Greece. *Catena*, 70 November, pp. 340-349.

Fremont, M.-J. & Malone, S.D., 1987. High precision relative locations of earthquakes at Mount St. Helens, Washington, *Journal of Geophysical Research.*, [online] 92(B10) September pp. 10223–10236. Available from: < https://agupubs.onlinelibrary.wiley.com/> [Accessed March 24 2018].

Gautier, S., Latorre, D., Virieux, J., Deschamps, A., Skarpelos, C., Soritiou, A., Serpetsidaki, A. and Tselentis, A. A new passive tomography of the Aigion Area (Gulf of Corinth, Greece) from the 2002 data set. *Pure and Applied Geophysics*, 163, pp. 431-453.

Hatzfeld, D., Karakostas, V., Ziazia, M., Kassaras, I., Papadimitriou, E., Makropoulos, K., Voulgaris and Papaioannou, Ch. 2000. Microseismicity anf faulting geometry in the Gulf of Corinth (Greece). *Geophysical Journal International*, 141, May, pp. 438-456.

Havskov, J. and Alguacil, G. 2004. *Instrumentation in earthquake seismology.*1^{st} ed. [electronic book] Springer Netherlands. Available from: <http://link.springer.com>[Accessed August 6 2015].

Ford, M., Rohais, S., Williams, E.A., Bourlange, S., Jousselin, D., Backert, N. and Malartre, F. 2012. Tectono-sedimentary evolution of the western Corinth rift (Central Greece), *Basin Research* [online] 25(1) February, pp. 3–25 Available from: <http://onlinelibrary.wiley.com/> [Accessed April 30 2016].

Kapetanidis, V. and Papadimitriou, P. (2011), Estimation of arrival-times in intense seismic sequences using a Master-Events methodology based on waveform similarity. *Geophysical Journal International*, 187 August, pp. 889-917. Available from: < http://dggsl.geol.uoa.gr/en_index.html> [Accessed March 24 2018].

Kapetanidis, V., Deschamps, A., Papadimitriou, P., Matrullo, E., Karakostantis, A., Bozionelos, G., Kaviris, G., Serpetsidaki, A., Lyon-Caen, H., Voulgaris, N., Bernard, P., Sokos, E. and Makropoulos, K., 2015. The 2013 earthquake swarm in Helike, Greece: seismic activity at the root of old normal faults. *Geophysical Journal International*, 202, January, pp. 2044-2073.

Kaviris, G., Papadimitriou, P. and Makropoulos, K., 2010. Anisotropy stusy of the February 4^{th} 2008 swarm in NW Peloponnesus (Greece). *Bulletin of the Geological Society of Greece, Proceedings of the* 12^{th} *Internationsl Congress, Patras,* May, pp. 2084-2092.

Kaviris, G., Spingos, I., Kapetanidis, V., Papadimitriou, P., Voulgaris, N. and Makropoulos, K. 2017. Upper crust seismic anisotropy study and temporal variations of shear-wave splitting parameters in the western Gulf of Corinth (Greece) during 2013. *Physics of Earth and Planetary Interiors*, 269, June, pp. 148-164.

Kreemer, C. and Chamot – Rooke, N., 2004. Contemporary kinematics of the southern Aegean and the Mediterranean Ridge. *Geophysical Journal International*, 157 February, pp. 1377-1392.

Lomax, A., J. Virieux, Volant, P. and Berge, C., 2000. *Probabilistic earthquake location in 3D and layered models: Introduction of a Metropolis-Gibbs method and comparison with linear locations, Advances in Seismic Event Location*. Thurber, C.H., and N. Rabinowitz (eds.), Kluwer, Amsterdam, 101-134.

Lyon-Caen, H., Papadimitriou, P., Deschamps, A., Bernard P., Makropoulos, K., Pacchiani, F. and Patau, G. 2004. First results of the CRLN seismic network in the western Corinth Rift: evidence for old-fault reactivation. *C. R. Geoscience* [online] 336 January pp. 343-351. Available from: <http://www.sciencedirect.com/> [Accessed March 24 2018].

McNeill, L.C., Collier, R.E., De Martini, P.M., Pantosti, D. and D' Addezio, G. 2005. Recent history of the Eastern Eliki Fault, Gulf of Corinth: geomorphology, palaeoseismology and impact on palaeoenvironments. *Geophysical Journal International* [online] 161(1) March pp. 154-166. Available from: <http://onlinelibrary.wiley.com/> [Accessed April 3 2015].

McNeill, L.C., Coterill, C.J., Bull J.M., Henstock, T.J., Bell, R. and Stefatos, A. 2007. Geometry and slip rate of the Aigion fault, a young normal fault system in the western Gulf. *Geology* [online] 35(4) April, pp. 355-358. Available from: <http://ardoise.ens.fr/> [Accessed April 3 2015].

Milne, J. 1886. The 'method of hyperbolas'of Milne. *Earthquakes and other Earth movements*. pp.202.

Moretti, I., Sakellariou, D., Lykousis, V. and Micarelli, L., 2003. The Gulf of Corinth: an active half graben?.*Journal of Geodynamics,* 36 (1) August, pp. 323-340 (18).

Morris, A., 2000. Magnetic fabric and palaeomagnetic analysis of the Plio-Quaternary calc-alkaline series of Aegina Island, South Aegean volcanic arc, Greece. *Earth and Planetary Science Letters*, 176 January, pp. 91-105.

Palyvos, N., Pantosti, D., De Martini, P.M., Lemeille, F., Sorel, D. and Pavlopoulos, K. 2005. The Aigion-Neos Erineos coastal normal fault system (western Corinth Gulf Rift, Greece): Geomorphological signature, recent earthquake history, and evolution. *Journal of Geophysical Reasearch* [online] 110, September, pp. B09302.

Papadimitriou P., Makropoulos K. and Drakopoulos, J., 1993. Seismic doublet analysis and application in the rupture process: preliminary results of the Rio-Antirio region (Greece), in *Proceedings of the 2nd congress of the Hellenic Geophysical Union*, Greece, pp. 502–508.

Papanikolaou, D. J., Royden, L. H., 2007. Disruption of the Hellenic arc: late Miocene extensional detachment faults and steep Pliocene-Quaternary normal faults – Or what happened at Corinth. *Tectonics,* 26 (5) October, TC5003 pp.1-16.

Pe-Piper, G. and Piper, D.J., 2005. The South Aegean active volcanic arc: relationships between magmatism and tectonics. *Developments in Volcanology,* 7, pp. 113-133.

Pearce, F.D., Rondenay, S., Sachpazi, M., Charalampakis, M. and Royden, L.H., 2012. Seismic investigationof the transition from continental to oceanic subduction along the western Hellenic Subduction Zone, *Journal of Geophysical Research*, 117 July, pp. 1-18 B07306.

Pirli, M., Voulgaris, N., Alexopoulos, J. and Makropoulos, K. 2004. Installation and preliminary results from a small aperture seismic array in Tripoli, Greece. *Bulletin of the Geological Society of Greece* [online] 36, April, pp. 1499-1508. Available from: < http://www.geo.auth.gr> [Accessed August 10 2017].

Pirli M., 2005. *Contribution to the determination of focal parameters of earthquakes in Greece with the technique of array stations*. Doctoral Thesis, National and Kapodistrian University of Athens, Athens.

Podvin P. and Lecomte I. 1991. Finite difference computation of traveltimes in very contrasted velocity models: a massively parallel approach and its associated tools. *Geophysical Journal International* [online] 105(1) April, pp 271–284. Available from: <https://academic.oup.com> [Accessed August 7 2017].

Press,W.H., Teukolsky, S.A., Vetterling,W.T. & Flannery, B.P. (1992). *Numerical recipes in FORTRAN, the art of scientific computing - second edition*. Cambridge University Press.

Rigo, A., Lyon-Caen, H., Deschamps, A., Hatzfeld, D., Makropoulos, K., Papadimitriou, P. and Kassaras I. 1996. A microseismic study in the western part of the Gulf of Corinth (Greece): implications for large-scale normal faulting mechanisms. *Geophysical Journal International* [online] 126 March, pp 663–688. Available from: <ftp://ftp.gps.caltech.edu/.pdf> [Accessed March 24 2018].

Ring, U. and Reischmann, T., 2002. The weak and superfast Cretan detachment, Greece: exhumation at subduction rates in extruding wedges. *Journal of the Geological Society*, 159 May, pp. 225-228.

Ring, U., Glodny, J., Will, T. and Thomson S., 2010. The Hellenic Subduction System: High – Pressure Metamorphism, Exhumation, Normal Faulting, and Large – Scale Extension. *Annual Review of Earth and Planetary Sciences*, 38 January, pp. 45-76.

Rost, S. and Thomas, Chr. 2002. Array Seismology: Methods and applications. *Reviews of Geophysics* [online] 40 (3) September. Available from: <http://stephanerondenay.com> [Accessed August 4 2015].

Rost, S. and Garnero E. 2004. Array Seismology Advances-Research into earth's interior. *Eos Earth & Space Science News* [online] 85(32) August, pp. 305-306.

Sakellariou, D., Lykousis, V., Alexandri, S., Kaberi, H., Rousakis, G., Nomikou, P. Georgiou, P. & Ballas, D., 2007. Faulting, seismicstratigraphic architecture and Late Quaternary evolution of the Gulf of Alkyonides Basin-East Gulf of Corinth, Central Greece, *Basin Research* [online] 19 , pp. 273–295 Available from: <http://refhub.elsevier.com/> [Accessed April 29 2016].

Schweitzer, J. 1997. HYPOSAT – a new routine to locate seismic events. *NORSAR Scientific Report* 1-97/98, pp. 94-102, NORSAR, Kjeller, Norway, November 1997.

Schweitzer, J., Fyen, J.,Mykkeltveit, S. &Kværna, T., 2002. *Seismic arrays, in Peter Bormann, ed., 'IASPEI New Manual of Seismological Observatory Practice (NMSOP)'*, GeoForschungsZentrum, Potsdam, Germany .

Sokos, E., Zahradnik, J., Kiratzi, A., Jansky, J., Gallovic, F., Novotny, O., Kostelecky, J., Serpetsidaki, A. and Tselentis, G.-A. 2012. The January 2010 Efpalio earthquake sequence in the western Corinth Gulf Greece. *Tectonophysics* [online] January pp. 299-309. Available from: <http://geo.mff.cuni.cz> [Accessed April 3 2015].

Sweeney J. J. and Walter W. R., 1998. Preliminary definition of geophysical regions for the Middle East and North Africa. *Lawrence Livermore National Laboratory*, UCRLID-132899, 40.

Tarantola, A. and Valette B. 1982. Generalized nonlinear inverse problems solved using the least squares criterion. *Reviews of Geophysics* [online] 20(2) May, pp.219-232. Available from: <http://onlinelibrary.wiley.com> [Accessed August 7 2017].

Taylor, B., Weiss, J.R., Goodliffe, A.M., Sachpazi, M., Laigle, M., Hirn, A., 2011.The structures, stratigraphy and evolution of the Gulf of Corinth Rift, Greece. *Geophysical Journal International* [online] 185 (3) March, pp. 1189–1219.

Tselentis, A. 1997. *Modern Seismology* (Volume I), Papasotiriou Publications, Athens.

Tsodoulos, I. M., Koukouvelas, I.K. and Pavlides, S., 2008. Tectonic geomorphology of the easternmost extension of the Gulf of Corinth (Beotia, Central Greece). *Tectonophysics*, 453 February, pp.211-232.

Vassilakis, E., Royden, L. and Papanikolaou D., 2011. Kinematic links between subduction along the Hellenic trench and extension in the Gulf of Corinth, Greece: A multidisciplinary analysis. *Earth and Planetary Science Letters*, 303 January, pp. 108-120.

Waldhauser, F., 2009. Near-real-time double-difference event location using long-term seismic archives, with application to Northern California, *Bulletin of Seismological Society of America*, [online] **99**(5) October, pp. 2736–2748. Available from: <http://www.ldeo.columbia.edu/> [Accessed March 24 2018].

Weiss, J., R. 2004. *A geophysical investigation of the gulf of Corinth, Greece.* Master Thesis, University of Hawaii.

Westaway, R. 2002. The Quaternary evolution of the Gulf of Corinth, central Greece: coupling between surface processes and flow in the lower continental crust. *Tectonophysics* [online] 348 December, pp.269-318.

Zhou, H. 1994. Rapid three-dimensional hypocentral determination using a master station method. *Journal of Geophysical Research* [online] 99(B8), pp.15.439-15.455. Available from: <https://documents.tips> [Accessed August 7 2017].